

THEORY OF ELECTRON TRANSPORT THROUGH SINGLE MOLECULES

Abdalghani Daaoub

B.Sc., M.Sc.

PhD Thesis in Nanoelectronics

Department of Physics, Lancaster University, UK

This Thesis is submitted in partial fulfilment of the
requirements for degree of Doctor of Philosophy

June 2020



Declaration

I hereby declare that the thesis is my own work and effort and has not been submitted in substantially the same form for the award of a higher degree elsewhere. Other sources of information have been used, they have been acknowledged. This thesis documents work carried out between January 2017 and June 2020 at Lancaster University, UK, under the supervision of Dr. Hatef Sadeghi and Prof. Colin J. Lambert and funded by Ministry of Higher Education and Scientific Research of Libya.

Abdalghani Daaoub

2020

Dedication

I would like to dedicate this work to my mother, the memory of my late beloved father, my wife, my brothers and my sisters.

Abstract

Understanding the electronic transport properties of junctions consisting of a scattering region such as a nanoscale region or molecule connected two electrodes is of fundamental interest. The theoretical work carried out in this thesis presents the electrical properties of two different types of two terminal nanojunctions: one dealing with gold electrodes which form gold | molecule | gold structures and the other with graphene sheet electrodes forming graphene | molecule | graphene junctions. Chapter 2 presents an introduction to the theoretical concept of density functional theory (DFT) and its implemented in this thesis, via the SIESTA code. The second tool is the quantum transport code Gollum which is based on Green's function-based scattering theory. To introduce this technique in Chapter 3, I present solutions of Green's functions for infinite and semi-infinite chains and the transmission coefficient equation which forms the theoretical basis of this code.

The first original topic I investigate in chapter 4 addresses anti-resonance features of destructive quantum interference in single-molecule thiophene junctions. This study is a collaborative work with experimentalists in Xiamen University, China. Controlling the electrical conductance and in particular the occurrence of quantum interference in single-molecule junctions through gating effects, has potential for the realization of high-performance functional molecular devices. In this work, I demonstrate the underlying science behind the tunable electronic structure of thiophene-based molecular junctions using electrochemically-gated. This is explained by destructive quantum interference (DQI) features in these molecules. Using electrochemical gating the Fermi energy is moved towards the DQI feature leading to two orders of magnitude changes in electrical conductance. This is a promising strategy for

obtaining improved in-situ control over the electrical performance of interference-based molecular devices.

In the second original work in chapter 5, I investigate quantum transport across graphene nanogaps bridged by carbon atomic chains. To realise the technological potential of electroburnt graphene junctions, there is a need to understand how their electronic and spintronic properties are controlled by edge terminations and by the carbon chains bridging their gaps. Here I study a wide variety of such structures and find that junctions with zigzag edges tend to have lower conductances than those with armchair edges, while junctions with ferromagnetically aligned edges have a higher transmission than anti-ferromagnetically aligned edges, because ferromagnetic alignment tends to increase the transmission of one of the spins. I also find that nanogaps formed from graphene with saturated edges tend to have a lower conductance than unsaturated edges, five-membered saturated terminal rings with saturated edges are poor conductors, while five-membered terminal rings (saturated or unsaturated) with unsaturated edges are highly conducting. In addition I find that junctions bridged by even-numbered chains of carbon atoms tend to have a lower conductance than those bridged by odd-numbered atomic chains, while chains attached to six-membered terminal rings and unsaturated edges tend to have a lower conductance than those attached to five-membered terminal rings and unsaturated edges.

Acknowledgements

A great thanks to Allah for his mercy and blessing. Thanks God for keeping my head up and my heart strong.

I would like firstly to take this opportunity to thank Dr. Hatef Sadeghi and Professor Lambert because this thesis would not have been possible or completed without the excellent supervision, guidance and trust I received from them.

My greetings, respect and thanks to all the group members who created a scientific atmosphere and have been good friends especially Dr. Sara, Dr. Alaa, Dr. Ali, Dr. Abdalkareem and Many thanks for providing all the necessary help.

Of course, most important I thank my family, relatives, friends, colleagues and teachers who through their constant support and their love taught me to be a good man.

List of publication during my PhD study

1. Bai, J., **Daaoub, A.**, Sangtarash, S., Li, X., Tang, Y., Zou, Q., ... & Liu, J. (2019). Anti-resonance features of destructive quantum interference in single-molecule thiophene junctions achieved by electrochemical gating. *Nature materials*, 18(4), 364.
2. Quantum Transport Across Graphene Nanogaps Bridged By Carbon Atomic Chains (to be submitted).
3. Single molecule conductance of Au-molecule-ITO heterojunctions (to be submitted)

Contents

Chapter 1.....	10
1.1 Introduction.....	10
1.1.1 Molecular electronics	10
1.1.2 Electrochemical gating	12
1.1.3 Structure–function relationship	12
1.1.4 Thermoelectric properties of single-molecule junctions.....	12
1.1.5 Spintronics	13
1.1.6 Quantum interference	14
1.2 Thesis Outline	16
References.....	17
Chapter 2.....	24
2. Density Functional Theory	24
2.1 Introduction	24
2.2 The Schrödinger Equation and Variational Principle	25
2.3 The Thomas-Fermi Theory	29
2.4 The Kohn-Sham Theorems	31
2.5 The Exchange Correlation Functionals	35
2.5.1 Local Density Approximation (LDA).....	35
2.5.1 Generalized Gradient Approximation (GGA).....	36
2.6 SIESTA.....	37
2.7 Pseudopotentials	38
2.7 Localized Atomic Orbital Basis Sets (LAOBs)	40
2.8 Basis Set Superposition Error Correction (BSSE) and Counterpoise Correction (CP)	43
References.....	45
Chapter 3.....	50
3. Single Particle Transport	50

3.1 Introduction	50
3.2 The Landauer Formula	50
3.3. Tight-Binding Model.....	53
3.4 One-Dimension.....	55
3.4.1 A Perfect One-Dimensional Lattice	55
3.4.2 One-Dimensional Scattering	58
3.5 Transport through an arbitrary scattering region.....	62
3.6 Calculation in Practice.....	66
3.7 Features of the Transport Curve	66
3.7.1 Breit-Wigner Resonance	67
3.7.2 Fano Resonance.....	68
3.7.3 Anti-Resonance	69
3.8 Scissors corrections	70
References.....	70
Chapter 4.....	75
Anti-resonance features of destructive quantum interference in single- molecule thiophene junctions achieved by electrochemical gating	75
4.1 Introduction.....	75
4.2 Results and Discussion	77
References.....	87
Chapter 5.....	90
Quantum transport across graphene nanogaps bridged by carbon atomic chains	90
5.1 Introduction.....	90
5.2 Results and Discussion	92
References.....	134
Chapter 6.....	144

6.1 Conclusion	144
6.2 Future Work.....	146
References.....	147

Chapter 1

1.1 Introduction

1.1.1 Molecular electronics

The idea of using single molecules as building blocks to design and fabricate molecular electronic components has been around for more than 40 years [1], but only recently it has attracted huge scientific interest to explore their unique properties and opportunities. Molecular electronics including self-assembled monolayers [2] and single-molecule junctions [3] are of interest not only for their potential to deliver logic gates [4-5], sensors[6-7], and memories [8] with ultralow power requirements and sub-10-nm device footprints, but also for their ability to probe room-temperature quantum properties at a molecular scale such as quantum interference [9] and thermoelectricity [10,11]. Single molecule electronics has gained intensive attention since the first molecular rectifier was proposed by Aviram and Ratner in 1974 [12]. By manipulating their chemical structure, a diverse range of molecules have been investigated, which function as basic electronic elementary devices, such as rectifiers,[13–16] conducting wires,[17–21] and negative differential resistance devices,[22–24]. The ability to use specific intermolecular interactions to assemble molecular devices appropriately is another critical challenge for molecular electronics. [25] Therefore, a quantitative understanding of the electron transport between adjacent molecules is an essential prerequisite.

There are five main categories of research in molecular scale electronics [3] namely: Molecular optoelectronics, molecular mechanics, molecular electronics, molecular

thermoelectrics, and molecular spintronics as shown in figure 1.1.1 in which studying the electronic transport properties of the junction is the central basis toward junction characterization for a wide range of applications.

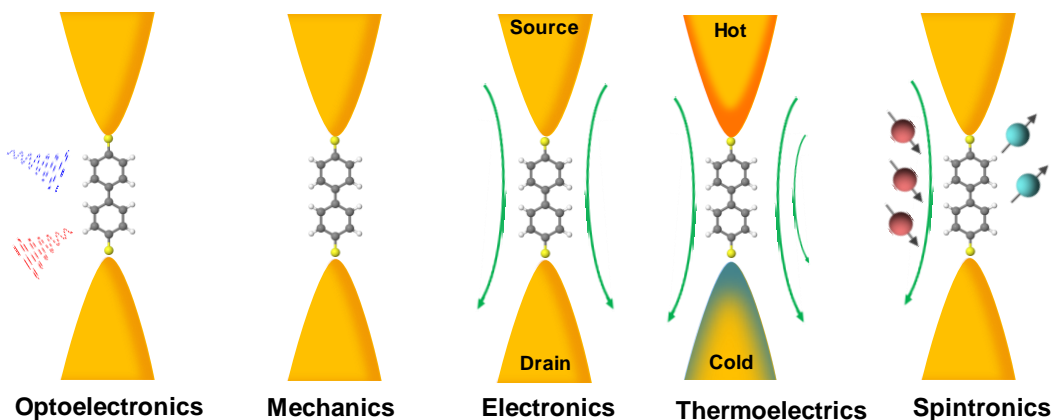


Figure 1.1.1: Molecular electronic active area of research [3]

In this thesis, I focus only on the molecular electronics system. Electron transport through single molecules is strongly affected by single-electron charging and energy level quantization. Molecular conformation, energies of frontier orbitals and charge distribution controls the quantum interference.

Most studies - both theoretical and experimental - focus on electrode molecule-electrode systems, which will be discussed in this thesis. Experimentally, these can be studied using Scanning Tunneling Microscopy Break Junctions (STM-BJ) [26-28] or Mechanically Controllable Break Junctions MCBJ [29,30]. Recently, more scalable techniques for contacting single molecules have been developed, including graphene-based junctions [31-34], silicene-based junctions [35], and CMOS-compatible electrodes, such as Pt and Pd [36]. However, structural defects in 2d hexagonal materials [37][38] mean that their use as electrodes is still in its infancy and for the moment gold break junctions remain the contacting method of choice. Within such

constraints, several methods of controlling electron transport have been developed including mechanical gating [39, 40] and electrochemical gating [41,42].

1.1.2 Electrochemical gating

In an electrochemical electrolyte solution, charge transport can be controlled by external potential (electrochemical gating). By tuning the potential of a third electrode (potential or gate electrode) added to a two terminal device with source and drain (e.g. STM tip and substrate electrodes), the energies of molecular orbitals, i.e. HOMO and LUMO can be tuned. This modifies the alignment of frontier molecular orbitals of the molecule relative to the Fermi level of electrodes and thus allows modulating the current through the junction [43-45].

1.1.3 Structure–function relationship

Mechanical modelling and simultaneous force and conductance measurements offer an alternative method for answering questions related to the structure of atomic junctions [46]. In particular, force measurements through single lead-molecule-lead junction provide independent mechanical facts that can be utilized to link the structure of junctions to electrical conductance. Simultaneous measurements of force and conductance in the nanometer scale junctions of Au point contacts showed that the force data are clearly correlated with the quantified changes of conductance [47-49].

1.1.4 Thermoelectric properties of single-molecule junctions

Studying the principle of heat transport and the electronic response to heating of the two sides of molecular junctions is not only of fundamental scientific attentiveness but also this can be used to convert waste heat to electricity economically, provided molecules with a high thermoelectric efficiency could be identified. Generation of

electricity from heat via the Seebeck effect is silent, environmentally friendly and requires no moving parts. Conversely, efficient Peltier cooling using such materials would have applications to on-chip cooling of CMOS-based devices [57]. The efficiency of a thermoelectric device is proportional to a dimensionless figure of merit $ZT = S^2GT/\kappa$, where S is the Seebeck coefficient, G is the electrical conductance, T is the temperature and $\kappa = \kappa_{el} + \kappa_{ph}$ is the thermal conductance due to electrons κ_{el} and phonons κ_{ph} . Therefore low- κ , high- G and high- S materials are needed. In the past couple of years, electrical conductance and Seebeck coefficient of various molecular junctions have been measured. The Seebeck coefficient in the range of $-33\mu\text{V/K}$ in Fullerene C60 dimer to $+21\mu\text{V/K}$ in 1,4-4-Benzenethiol (4-BT) has been measured [50,51]. These Seebeck values are not sufficient enough to deliver high performance molecular scale thermoelectric materials. Recently, new strategies based on quantum interference have been proposed to improve the efficiency of molecular scale thermoelectricity [52,53].

In addition, the sign of S can be used to derive the type of charge carriers at junctions. A positive S results from the transport of holes through the highest occupied molecular orbital (HOMO) and a negative S indicates the transport of electrons through the lowest occupied molecular orbital (LUMO).

1.1.5 Spintronics

Spin electronics (or spintronics) is one of the growing areas of current nanotechnology that has a big impact on daily life, for example, by improving information storage on the hard drive and magnetic recording. This branch of molecular electronics attempt to study both electronic and nuclear spin to control spin transport and magnetization in single-molecule devices. These devices can be formed in three ways including non-

magnetic electrodes contacting magnetic molecules, magnetic electrodes contacting a non-magnetic molecule and magnetic electrodes contacting a magnetic molecule [54]. Tuning molecular properties by chemical design provide unique opportunity to increase performances of molecular spintronic devices to the level required to compete with alternative electronic qubits, such as impurity spins in extended solids.

1.1.6 Quantum interference

Quantum interference is another purely quantum mechanical aspect of charge transport via a single molecule junction. This occurs due to the wave nature of electrons when the scale length of the device becomes comparable to the coherence length of the electronic phase. Quantum interference effects can significantly reduce the conductance of meta connected benzene molecule compared to para connected benzene to electrodes [63-71]. By studying quantum transport through junctions, we can investigate the symbiotic relationship between quantum interference and physical, chemical and electronic structure, which is sensitive to environmental factors by conformational control, polarisation or redox processes (electrical vs. electrochemical gating) leads to new opportunities for controlling the electrical and thermoelectrical properties of single molecules connected to nano-electrodes [9].

The realization of single-molecule electronic devices is challenging in several ways. First, the typical length of molecules used in the research field is in the order of 1–2 nm. In addition, electrodes typically made of noble metals, separated by 1–2 nm is beyond the limits of classical top-down lithographic techniques. Second, due to the tiny dimensions of the molecule, it is typically impractical to place the molecule in the nanogap by direct manipulation. Instead, chemical interaction between the molecule

and the electrode is needed for positioning of a molecule in the gap between the electrodes. Third, since the electrodes are typically much larger than the molecules, it is an additional challenge to make sure that only a single molecule is placed in each functional device. In addition to these three basic challenges, other challenges such as device stability, uniformity, yield, and scalability are equally important. [55].

1.2 Thesis Outline

My aim in this thesis is to review the theoretical techniques to treat electron transport in molecular scale junctions. The theoretical approach includes two main techniques, Density Functional Theory (Ch. 2), which is implemented in the SIESTA code [55] and the non-equilibrium Green's function formalism of transport theory [56] (Ch. 3). Both of these methods are used extensively to study a family of molecules. This helps not only to understand the experimental observations but also provides a vital design tool to develop strategies for molecular electronic building blocks. The previous chapters have been used to understand quantum interference (QI) when trying to study charge transport through thiophene between gold-gold electrodes in the presence of electrochemical gating in chapter 4. In chapter 5, I studied spin dependent quantum transport across graphene nanogaps bridged by carbon atomic chains which in this chapter I tried to classify my study to four main classes that will affect in electron transport properties. The first class includes zigzag and armchair graphene edges, the second class describes the role of number of carbon atoms in a chain (Odd and Even carbon atomic chains) on the transmission properties, the third class presents the effect of the saturated or unsaturated edges and the last class shows the role of six and five membered terminal rings effect on transmission properties and conductance through these graphene junctions.

References

- [1] “Visions for a molecular future,” *Nature Nanotechnology*, vol. 8, no. 6, pp. 385– 389, 2013.
- [2] J. L. Christopher, L. A. Estroff, J. K. Kriebel, R. G. Nuzzo, and G. M. Whitesides, “Self-assembled monolayers of thiolates on metals as a form of nanotechnology,” *Chemical Reviews*, vol. 105, no. 4, pp. 1103–1170, 2005. PMID: 15826011.
- [3] S. V. Aradhya and L. Venkataraman, “Single-molecule junctions beyond electronic transport,” *Nature Nanotechnology*, vol. 8, no. 6, pp. 399–410, 2013.
- [4] S. Sangtarash, C. Huang, H. Sadeghi, G. Sorohhov, J. Hauser, T. Wandlowski, W. Hong, S. Decurtins, S.-X. Liu, and C. J. Lambert, “Searching the Hearts of Graphene-like Molecules for Simplicity, Sensitivity, and Logic,” *Journal of the American Chemical Society*, vol. 137, no. 35, pp. 11425–11431, 2015.
- [5] Yan Geng, Sara Sangtarash, Cancan Huang, Hatef Sadeghi, Yongchun Fu, Wenjing Hong, Thomas Wandlowski, Silvio Decurtins, Colin J Lambert, Shi-Xia Liu, “Magic ratios for connectivity-driven electrical conductance of graphene-like molecules,” *Journal of the American Chemical Society* 137 (13), 4469-4476 (2015)
- [6] H. Sadeghi, L. Algaragholy, T. Pope, S. Bailey, D. Visontai, D. Manrique, J. Ferrer, V. Garcia-Suarez, S. Sangtarash, and C. J. Lambert, “Graphene sculpture nanpores for DNA nucleobase sensing,” *Journal of Physical Chemistry B*, vol. 118, no. 24, pp. 6908–6914, 2014.

- [7] H. Sadeghi, S. Bailey, C. J. Lambert, "Silicene-based DNA nucleobase sensing," *Applied Physics Letters* 104 (10), 103104, 2014.
- [8] T. Prodromakis, C. Toumazou, and L. Chua, "Two centuries of memristors," *Nature Materials*, vol. 11, no. 6, pp. 478–481, 2012.
- [9] C. J. Lambert, "Basic concepts of quantum interference and electron transport in single-molecule electronics," *Chem. Soc. Rev.*, vol. 44, pp. 875–888, 2015.
- [10] H. Sadeghi, S. Sangtarash, and C. J. Lambert, "Oligoynes molecular junctions for efficient room temperature thermoelectric power generation," *Nano letters*, vol. 15, no. 11, pp. 7467–7472, 2015.
- [11] Sadeghi, H.; Sangtarash, S.; Lambert, C. J., "Enhanced Thermoelectric Efficiency of Porous Silicene Nanoribbons," *Scientific Reports* 5, 9514 (2015)
- [12] A. Aviram, M. A. Ratner, *Chem. Phys. Lett.* 1974, 29, 277 – 283.
- [13] A. Batra, P. Darancet, Q. Chen, J. S. Meisner, J. R. Widawsky, J. B. Neaton, C. Nuckolls, L. Venkataraman, *Nano Lett.* 2013, 13, 6233 –6237.
- [14] Zhao, Jin, et al. "Single C₅₉N molecule as a molecular rectifier." *Physical review letters* 95.4 (2005): 045502.
- [15] Lei, Shulai, et al. "Orbital-selective single molecule rectifier on graphene-covered Ru (0001) Surface." *Applied Physics Letters* 102.16 (2013): 163506..
- [16] Wang, Bing, et al. "Conduction Mechanism of Aviram– Ratner Rectifiers with Single Pyridine– σ – C₆₀ Oligomers." *The Journal of Physical Chemistry B* 110.48 (2006): 24505-24512..
- [17] Lafferentz, Leif, et al. "Conductance of a single conjugated polymer as a continuous function of its length." *Science* 323.5918 (2009): 1193-1197.

- [18] Choi, Seong Ho, BongSoo Kim, and C. Daniel Frisbie. "Electrical resistance of long conjugated molecular wires." *Science* 320.5882 (2008): 1482-1486.
- [19] Zhao, Xiaotao, et al. "Oligo (aryleneethynylene) s with terminal pyridyl groups: synthesis and length dependence of the tunnelling to hopping transition in single-molecule conductances." *Chemistry of materials*. 25.21 (2013): 4340-4347.
- [20] Davis, William B., et al. "Molecular-wire behaviour in p-phenylenevinylene oligomers." *Nature* 396.6706 (1998): 60-63.
- [21] Kaliginedi, Veerabhadrrao, et al. "Correlations between molecular structure and single-junction conductance: a case study with oligo (phenyleneethynylene)-type wires." *Journal of the American Chemical Society* 134.11 (2012): 5262-5275.
- [22] Chen, J., et al. "Room-temperature negative differential resistance in nanoscale molecular junctions." *Applied physics letters* 77.8 (2000): 1224-1226.
- [23] Guisinger, Nathan P., et al. "Room temperature negative differential resistance through individual organic molecules on silicon surfaces." *Nano Letters* 4.1 (2004): 55-59.
- [24] Chen, J., et al. "Large on-off ratios and negative differential resistance in a molecular electronic device." *science* 286.5444 (1999): 1550-1552..
- [25] Pijper, Thomas C., et al. "Reversible light induced conductance switching of asymmetric diarylethenes on gold: surface and electronic studies." *Nanoscale* 5.19 (2013): 9277-9282.
- [26] Li, Chen, et al. "Charge transport in single Au vertical bar alkanedithiol vertical bar Au junctions: Coordination geometries and conformational

- degrees of freedom." *Journal of the American Chemical Society* 130.1 (2008): 318-326..
- [27] Xu, Bingqian, and Nongjian J. Tao. "Measurement of single-molecule resistance by repeated formation of molecular junctions." *Science* 301.5637 (2003): 1221-1223.
- [28] GJ Ashwell, B Urasinska, C Wang, MR Bryce, I Grace, CJ Lambert, "Single-molecule electrical studies on a 7 nm long molecular wire" *Chemical Communications*, 4706-4708 2006
- [29] Huber, R.; Gonzalez, M. T.; Wu, S.; Langer, M.; Grunder, S.; Horhoiu, V.; Mayor, M.; Bryce, M. R.; Wang, C. S.; Jitchati, R.; Schonenberger, C.; Calame, M. J. *Am. Chem. Soc.* 2008, 130, 1080-1084.
- [30] Hong, W.; Manrique, D. Z.; Moreno-Garca, P.; Gulcur, M.; Mishchenko, A.; Lambert, C. J.; Bryce, M. R.; Wandlowski, T. J. *Am. Chem. Soc.* 2011, 134, 2292-2304.
- [31] H Sadeghi, JA Mol, CS Lau, GAD Briggs, J Warner, CJ Lambert, "Conductance enlargement in picoscale electroburnt graphene nanojunctions," *Proceedings of the National Academy of Sciences* 112 (9), 2658-2663, 2015
- [32] JA Mol, CS Lau, WJM Lewis, H Sadeghi, C Roche, A Cnossen, JH Warner, C.J. Lambert, H.L. Anderson and G.A.D. Briggs, "Graphene-porphyrin single-molecule transistors," *Nanoscale* 7 (31), 13181-13185, 2015
- [33] XH Zheng, GR Zhang, Z Zeng, VM García-Suárez, CJ Lambert, "Effects of antidots on the transport properties of graphene nanoribbons," *Physical Review B* 80 (7), 075413, 2009

- [34] H Sadeghi, S Sangtarash, CJ Lambert, “Enhancing the thermoelectric figure of merit in engineered graphene nanoribbons” *Beilstein journal of nanotechnology* 6, 1176 2015
- [35] H Sadeghi, S Bailey, CJ Lambert, “Silicene-based DNA nucleobase sensing,” *Applied Physics Letters* 104 (10), 103104 2014
- [36] VM García-Suárez, AR Rocha, SW Bailey, CJ Lambert, S Sanvito, J Ferrer, “Single-channel conductance of H₂ molecules attached to platinum or palladium electrodes,” *Physical Review B* 72 (4), 045437, 2005
- [37] CJ Lambert, DL Weaire, “Theory of the arrangement of cells in a network” *Metallography* 14 (4), 307-318 1981
- [38] Detailed Atomic Structure of Defects in 2D Materials: From Graphene to Transition Metal Dichalcogenides, JH Warner, *Microscopy and Microanalysis* 21, 573 2015
- [39] CM Finch, S Sirichantaropass, SW Bailey, IM Grace, VM Garcia-Suarez, C J Lambert, “Conformation dependence of molecular conductance: chemistry versus geometry,” *Journal of Physics: Condensed Matter* 20 (2), 022203 2007
- [40] Laura Rincón-García, Ali K Ismael, Charalambos Evangelis, Iain Grace, Gabino Rubio-Bollinger, Kyriakos Porfyrakis, Nicolás Agrait, Colin J Lambert “Molecular design and control of fullerene-based bi-thermoelectric materials” *Nature materials* 15 (3), 289-293 (2016)
- [41] Yonghai Li, Masoud Baghernejad, Al-Galiby Qusiy, David Zsolt Manrique, Guanxin Zhang, Joseph Hamill, Yongchun Fu, Peter Broekmann, Wenjing Hong, Thomas Wandlowski, Deqing Zhang, Colin Lambert, “Three-State Single-Molecule Naphthalenediimide Switch: Integration of a Pendant Redox

- Unit for Conductance Tuning” *Angewandte Chemie International Edition* 54 (46), 13586-13589 2015
- [42] VM García-Suárez, CJ Lambert, DZ Manrique, T Wandlowski, “Redox control of thermopower and figure of merit in phase-coherent molecular wires,” *Nanotechnology* 25 (20), 205402 2014
- [43] Brooke, R. J., Jin, C., Szumski, D. S., Nichols, R. J., Mao, B. W., Thygesen, K. S., & Schwarzacher, W. (2015). Single-molecule electrochemical transistor utilizing a nickel-pyridyl spinterface. *Nano letters*, 15(1), 275-280.
- [44] SVEzzoli, A., Grace, I., Brooke, C., Wang, K., Lambert, C. J., Xu, B., ... & Higgins, S. J. (2015). Gating of single molecule junction conductance by charge transfer complex formation. *Nanoscale*, 7(45), 18949-18955.
- [45] Huang, C., Rudnev, A. V., Hong, W., & Wandlowski, T. (2015). Break junction under electrochemical gating: testbed for single-molecule electronics. *Chemical Society Reviews*, 44(4), 889-901..
- [46] Agrait, N., Yeyati, A. L., & Van Ruitenbeek, J. M. (2003). Quantum properties of atomic-sized conductors. *Physics Reports*, 377(2-3), 81-279..
- [47] Xu, B., Xiao, X., & Tao, N. J. (2003). Measurements of single-molecule electromechanical properties. *Journal of the American Chemical Society*, 125(52), 16164-16165.
- [48] Xu, B., & Tao, N. J. (2003). Measurement of single-molecule resistance by repeated formation of molecular junctions. *science*, 301(5637), 1221-1223.
- [49] Giessibl, F. J. (2000). Atomic resolution on Si (111)-(7× 7) by noncontact atomic force microscopy with a force sensor based on a quartz tuning fork. *Applied Physics Letters*, 76(11), 1470-1472.

- [50] Rincón-García, L., Evangeli, C., Rubio-Bollinger, G., & Agraït, N. (2016). Thermopower measurements in molecular junctions. *Chemical Society Reviews*, 45(15), 4285-4306.
- [51] Wang, K., Meyhofer, E., & Reddy, P. (2020). Thermal and thermoelectric properties of molecular junctions. *Advanced Functional Materials*, 30(8), 1904534..
- [52] Sangtarash, S., & Sadeghi, H. (2020). Radical enhancement of molecular thermoelectric efficiency. *Nanoscale Advances*, 2(3), 1031-1035..
- [53] Sadeghi, H. (2019). Quantum and Phonon Interference-Enhanced Molecular-Scale Thermoelectricity. *The Journal of Physical Chemistry C*, 123(20), 12556-12562.
- [54] Camarero, J., & Coronado, E. (2009). Molecular vs. inorganic spintronics: the role of molecular materials and single molecules. *Journal of Materials Chemistry*, 19(12), 1678-1684.
- [55] Sun, L., Diaz-Fernandez, Y. A., Gschneidner, T. A., Westerlund, F., Lara-Avila, S., & Moth-Poulsen, K. (2014). Single-molecule electronics: from chemical design to functional devices. *Chemical Society Reviews*, 43(21), 7378-7411..
- [56] Sadeghi, H. (2018). Theory of electron, phonon and spin transport in nanoscale quantum devices. *Nanotechnology*, 29(37), 373001.
- [57] Sadeghi, H., Sangtarash, S., & Lambert, C. J. (2015). Oligoynes molecular junctions for efficient room temperature thermoelectric power generation. *Nano letters*, 15(11), 7467-7472.

Chapter 2

2. Density Functional Theory

2.1 Introduction

Both chemists and physicists widely employ DFT to explore the ground-state properties of various interacting many-particles, including crystal, atoms and molecules. DFT plays a crucial role of transforming many-particles system into a unified non-interacting fermions within an effective area. This simply implies that the electrical features of the many-interacting particles system can be defined as a density functional of the system's ground state density [1, 2]. The benefits of DFT were confirmed in 1998, as Walter Kohn, the Nobel Prize winner in Chemistry was awarded for his great contribution in developing the density functional theory. Various chemists and physicists consider DFT as one of the most reliable methodologies that has been used in various molecular systems with most of the articles and book in literature detailing DFT's principles as well as its use [1-6]. Initially, DFT was founded upon Thomas-Fermi's theory 1920s. This model presented some of the crucial steps required to get the density functional for the cumulative energy and it was based on wave-functions [1, 6-8]. For nearly a period of four decades, further improvements were made, starting with Hartree, then Dirac, Fock and later Slater. Finally, Thomas-Fermi's works was a great breakthrough. Both Kohn-Sham technique and Hohenberg-Kohn theorems gave DFT a great foundation [1, 3, 4, 7-11].

This chapter is aimed at presenting a brief introduction about DFT, demonstrating the key formalism as the technique to address problems concerning non-relativistic many-body time independent Schrödinger equation (TISE), because functional of an electron

density can be used to determine the properties of the many-particles system. Moreover, I will present a brief summary of SIESTA (DFT code) that I have applied extensively throughout this PhD research as one of the theoretical techniques to improve the structures.

2.2 The Schrödinger Equation and Variational Principle

The time-independent, non-relativistic Schrödinger equation can be employed to describe all non-relativistic many-particles system as follows:

$$H\Psi_i(\vec{r}_1, \vec{r}_2, \dots, \vec{r}_N, \vec{R}_1, \vec{R}_2, \dots, \vec{R}_M) = E_i\Psi_i(\vec{r}_1, \vec{r}_2, \dots, \vec{r}_N, \vec{R}_1, \vec{R}_2, \dots, \vec{R}_M) \quad (2.1)$$

In this case H stands for the system's Hamiltonian operator comprising of M -nuclei as well as N -electrons, which describes how particles interact with one another, whereas Ψ_i denotes the wave-function of the system's i^{th} eigenstate and E_i represents the numerical value assigned to energy of the i^{th} state as defined by Ψ_i . For such a system, the Hamilton operator can be presented as the total sum of all the five terms that are given by (2.2)

$$H = \overbrace{-\frac{\hbar^2}{2m_e} \sum_{i=1}^N \nabla_i^2}^{T_e} - \overbrace{\frac{\hbar^2}{2m_n} \sum_{n=1}^M \nabla_n^2}^{T_n} - \overbrace{\frac{1}{4\pi\epsilon_0} \sum_{i=1}^N \sum_{n=1}^M \frac{Ze^2}{|\vec{r}_i - \vec{R}_n|}}^{U_{en}} + \overbrace{\frac{1}{8\pi\epsilon_0} \sum_{i=1}^N \sum_{j \neq i}^N \frac{e^2}{|\vec{r}_i - \vec{r}_j|}}^{U_{ee}} + \overbrace{\frac{1}{8\pi\epsilon_0} \sum_{n=1}^M \sum_{n' \neq n}^M \frac{Z_n Z_{n'} e^2}{|\vec{R}_n - \vec{R}_{n'}|}}^{U_{nn}} \quad (2.2)$$

In which case, i as well as j represents the N -electrons as n and n' run-over the system's M -nuclei, m_n and m_e represent the mass of nucleus and electron respectively, Z_n and e denote the nuclear and electron charge respectively. The nuclei

and electrons position are denoted as \vec{R}_n and \vec{r}_i respectively, and the Laplacian operator, ∇_i^2 in the Cartesian co-ordinates ∇_i^2 is defined as follows:

$$\nabla_i^2 = \frac{\partial^2}{\partial x_i^2} + \frac{\partial^2}{\partial y_i^2} + \frac{\partial^2}{\partial z_i^2}$$

The two terms, T_n as well as T_e in equation (2.2) denoted the kinetic energy of nuclei and electrons respectively. The crucial part of Hamiltonian is represented by the last three terms; whereby T_{en} described the attractive electrostatic interactions that exist between the nuclei and the electrons. Both the nuclear-nuclear, U_{nn} as well as the electron-electron, U_{ee} describes the repulsive component of potential [1, 3, 6, 9, and 13]. The Born-Oppenheimer approximation, which is also referred to as clamped nuclei approximation is used, because approximately 99.9 percent mass of the atom is concentrated within the nucleus (for instance, hydrogen nucleus weigh about 1800 times as compared to an electron) as well as the nucleus is considered to be fixed than the electrons. In such as case, provided that the treated atoms' nuclei are fixed, then there is no kinetic energy and they have not any significant contribution to the full wave-function. The results of this assumption is that an electron systems Hamiltonian decreased the Hamiltonian to form a new one, an electronic Hamiltonian denoted as H_{ele} that is represented as shown below in a fixed nuclear picture [1, 3, 36, 13-15]:

$$H_{ele} = -\overbrace{\frac{\hbar^2}{2m_e} \sum_{i=1}^N \nabla_i^2}^{T_e} - \overbrace{\frac{1}{4\pi\epsilon_0} \sum_{i=1}^N \sum_{n=1}^M \frac{1}{|\vec{r}_i - \vec{R}_n|} Z_n e^2}^{U_{en}} + \overbrace{\frac{1}{4\pi\epsilon_0} \frac{1}{2} \sum_{i=1}^N \sum_{i \neq j}^N \frac{e^2}{|\vec{r}_i - \vec{r}_j|}}^{U_{ee}}$$

$$+ \overbrace{\frac{1}{4\pi\epsilon_0} \frac{1}{2} \sum_{i=1}^M \sum_{n \neq n'}^M \frac{Z_n Z_{n'} e^2}{|\vec{R}_n - \vec{R}_{n'}|}}^{U_{nn}}$$

$$H = \underbrace{\sum_i V_{ext}(r_i)}_{\text{nuclei-electron interaction}} - \underbrace{\frac{\hbar^2}{2m_e} \sum_i \nabla_i^2}_{\text{kinetic term}} + \underbrace{\frac{1}{8\pi\epsilon_0} \sum_{i \neq j} \frac{e^2}{|\vec{r}_i - \vec{r}_j|}}_{\text{electron-electron interaction}} \quad (2.3)$$

In this case U_{nn} represents the determined constant. The Schrödinger equation for the ‘clamped-nuclei for this system is:

$$H_{ele}\Psi_{ele} = E_{ele}\Psi_{ele} \quad (2.4)$$

In this case, Ψ_{ele} is dependent on the electron coordinates. Moreover, the nuclear part does not appear explicitly in Ψ_{ele} , but only enter parametrically. The total energy, E_{total} can be given by having the sum of the E_{ele} as well as the constant nuclear-repulsion term that is given by the following equation:

$$E_{total} = E_{ele} + U_{nn} \quad (2.5)$$

In itself, the wave-function is not regarded as an observable quantity, however its modulus squared may be represented as:

$$|\Psi(\vec{r}_1, \vec{r}_2, \dots, \vec{r}_N)|^2 d\vec{r}_1 d\vec{r}_2 \dots d\vec{r}_N \quad (2.6)$$

The above equation denotes the likelihood that electrons 1, 2... n exist within the volume elements $d\vec{r}_1 d\vec{r}_2 \dots d\vec{r}_N$. Because most electrons are indistinguishable, the probability is unchangeable provided that any two electrons’ coordinates (in this case, i and j) are changed.

$$|\Psi(\vec{r}_1, \vec{r}_2, \dots, \vec{r}_i, \vec{r}_j, \dots, \vec{r}_N)|^2 = |\Psi(\vec{r}_1, \vec{r}_2, \dots, \vec{r}_j, \vec{r}_i, \dots, \vec{r}_N)|^2 \quad (2.7)$$

Since is apparent that all electrons as fermions with a half spin, then it is crucial for Ψ to be anti-symmetric in respect to the spatial’s interchange as well as the spin of any of the two electrons. This is given as:

$$\Psi(\vec{r}_1, \vec{r}_2, \dots, \vec{r}_i, \vec{r}_j, \dots, \vec{r}_N) = -\Psi(\vec{r}_1, \vec{r}_2, \dots, \vec{r}_j, \vec{r}_i, \dots, \vec{r}_N) \quad (2.8)$$

The logical consequence of the wave-functions' probability interpretation is that an integral of the equation (2.6) in a variety of variables is equal to one. This means that the probability of determining an N -electron within the space should be precisely unity,

$$\int \dots \int |\Psi(\vec{r}_1, \vec{r}_2, \dots, \vec{r}_N)|^2 d\vec{r}_1 d\vec{r}_2 \dots d\vec{r}_N = 1 \quad (2.9)$$

The wave-function that satisfies the equation (2.9) is referred to as a normalized wave-function.

The Schrödinger equation does not have an exact solution. For this reason, various theories have been developed in order to achieve this goal. The first theory was developed by Hartree, followed by Hartree-Fock amongst others. A good number of these theories are based one of the crucial theoretical principles referred to as the wavefunction's variational principle [1, 2, 5, 6, and 12]. The principle simply presents how to find solutions by applying an appropriate trial wave-functions Ψ_{Tri} . Although this principle is very crucial in the study of ground-state, it is never beneficial as far as the study of excited-states is concerned. In a system whose state is Ψ_{Tri} , then the expectation value of energy can be given as [1, 3, and 9]:

$$\langle E_{Tri} \rangle = \frac{\int \Psi_{Tri} H \Psi_{Tri}^* d\vec{r}}{\int \Psi_{Tri} \Psi_{Tri}^* d\vec{r}} \quad (2.10)$$

Equation (2.10) has the variational principle. This implies that the energy calculated as the Hamiltonian operator's expectation value from any Ψ_{Tri} (predicted wave-function), which represents the upper-bound to Ψ_{GS} (true ground-state energy) is normalized in relation to equation (2.9), as well as both Ψ_{Tri} and the ground state, ($\Psi_{Tri} = \Psi_{GS}$) are equal. Also, it implies that E_{Tri} is equal to the precise ground state energy E_{GS} , and the equation (2.10) that represents the ground-state can be rewritten as:

$$\langle E_{GS} \rangle = \int \Psi_{GS} H \Psi_{GS}^* d\vec{r} \quad (2.11)$$

A normalized Ψ_{Tri} exhibits that E_{Tri} is greater than E_{GS} or E_{Tri} equal E_{GS} . Thus, the best alternative of E_{Tri} will always be the one where E_{Tri} is totally minimized [3, 4]

2.3 The Thomas-Fermi Theory

Most of the earliest approaches that uses electron density instead of wave-form in order to collect information regarding systems' electronic structures as themselves old as quantum mechanics. These approaches dates back to early works that was performed in 1926 with Llewellyn Thomas, as well as that of Enrico Fermi conducted in 1928. The two developed independently a similar concept of attempting to construct an approach to approximate the potential and kinetic energy as the functional of an electronic density. This means that the T-F concept is a quantum mechanical can be defined based on the functional energy for the system's ground state level, with a certain number of orbitals around the atom as well as a certain charge. Thus, this was one of the initial attempts of using the electron density rather than wave-function in order to address a ground-state Schrödinger equation for many-particles systems [7, 8, 12, 16]

Irrespective of the fact that there is non-uniform distribution of electronic in an atom, the approximation was determined assuming that there is uniform distribution of atoms (as per the uniform electron gas) in all the small elements of volume ΔV close by, while electron density $n(\vec{r})$ may be changed from ΔV to another state. The approximation for kinetic energy applied is given as:

$$T_{T-F}[n(\vec{r})] = C_F \int [n(\vec{r})]^{5/3} d\vec{r} \quad (2.12)$$

Where, $C_F = \frac{3}{10} (3\pi^2)^{2/3} = 2.8712$ as well as $n(\vec{r})$ denotes the electron density.

Similarly, an approximation can be proposed in order to define the internal potential energy U_{en} as a result of the attractive interactions between N -electrons as well as M -nuclei:

$$U_{en} = \int n(\vec{r}) V_n(\vec{r}) d\vec{r} \quad (2.13)$$

In which, $V_n(\vec{r})$ represents the electron's potential energy because of the nucleus electric-field (i.e. the external potential), and it is written as:

$$V_n(\vec{r}) = -\frac{1}{4\pi\epsilon_0} \sum_{i=1}^N \sum_{n=1}^M \frac{1}{|\vec{r}_i - \vec{R}_n|} Z_n e^2 \quad (2.14)$$

Where Z denotes the atomic number as well as e represents the electron charge. In this case, approximate electron-electron repulsive energy can be presented as:

$$U_{ee} = \frac{1}{4\pi\epsilon_0} \frac{1}{2} e^2 \int \frac{n(\vec{r})n(\vec{r}')}{|\vec{r} - \vec{r}'|} d\vec{r} d\vec{r}' \quad (2.15)$$

All these equations (2.12), (2.13) as well as (2.15) having the U_{nn} term present T-F model as follows:

$$F_{T-F}[n(\vec{r})] = T_{T-F} + U_{en} + U_{ee} + U_{nn} \quad (2.16)$$

In equation (2.16), the fourth term U_{nn} represents the nuclear-nuclear repulsion. This term is crucial in determining the constant in the two cases, when either the nuclei are bound or not. For M -nuclei within the system, U_{nn} is given as [1, 3, 7, 8 and 12]:

$$U_{nn} = \frac{1}{4\pi\epsilon_0} \frac{1}{2} \sum_{n=1}^M \sum_{n' \neq n}^M \frac{1}{|\vec{R}_n - \vec{R}_{n'}|} Z_n Z_{n'} e^2 \quad (2.17)$$

2.4 The Kohn-Sham Theorems

It is Kohn and Sham who realized that Hohenberg-Kohn theory could be applied on both non-interacting and interacting systems. Since DFT avoids the challenge of an interacting many-particles system. One of the advantages of non-interacting systems over the interacting systems is that it is easier to determine its ground-state energy. Kohn and Sham developed this concept in 1965, claiming the possibility to replace the initial Hamiltonian of a system with the non-interacting system's effective Hamiltonian (H_{eff}) in the effective external potential, $V_{eff}(\vec{r})$ that generates a similar ground-state density as that generated by the original system. Because a clear recipe for computing this was not yet determined, Kohn-Sham approach was considered as a significant ansatz, however is so easier to solve as compare to the non-interacting challenge. Kohn-Sham approach is founded on Hohenberg-Kohn universal density, and is given by [6, 9, 10 and 20]:

$$F_{H-K}[n(\vec{r})] = T_{int}[n(\vec{r})] + U_{ee}[n(\vec{r})] \quad (2.18)$$

For the case of non-interacting electrons, the Hohenberg-Kohn functional is minimized to only kinetic energy. Kohn-Sham energy functional $F_{K-S}[n(\vec{r})]$, contrary to equation (2.13,14,15,16), is presented as:

$$F_{K-S}[n(\vec{r})] = T_{non}[n(\vec{r})] + E_{Hart}[n(\vec{r})] + \int V_{ext}(\vec{r}) n(\vec{r}) d\vec{r} + E_{xc}[n(\vec{r})] \quad (2.19)$$

In this case, T_{non} represents the non-interacting system's kinetic energy which is distinct from that of T_{int} (kinetic energy for interaction system) presented in equation (2.21). Moreover E_{Hart} represents the classical self-interaction energy or classical electrostatic energy of the electron gas that is related with the density $n(\vec{r})$. In the

equation, the 4th term E_{xc} denotes an exchange-correlation energy functional, which is presented as:

$$E_{xc}[n(\vec{r})] = F_{H-K}[n(\vec{r})] - \overbrace{\frac{1}{2} \int \frac{n(\vec{r}_1)n(\vec{r}_2)}{|\vec{r}_1 - \vec{r}_2|} d\vec{r}_1 d\vec{r}_2}^{E_{Hart}[n(\vec{r})]} - T_{non}[n(\vec{r})] \quad (2.20)$$

In equation (2.19), the 1st, 2nd and 3rd terms can be cast trivially to a functional form. Contrarily, E_{xc} does not have an exact functional form. For the last few decades, there has been a lot of efforts to develop a better approximation than E_{xc} . At the present, functionals are able to investigate as well as predict various physical properties of a number of solid state systems as well as the molecules. In equation (2.25), functional derivatives are taken from the last three terms in order to come up with an effective single-particle potential $V_{eff}(\vec{r})$, and is given by:

$$V_{eff}(\vec{r}) = V_{ext}(\vec{r}) + \frac{\partial E_{Hart}[n(\vec{r})]}{\partial n(\vec{r})} + \frac{\partial E_{xc}[n(\vec{r})]}{\partial n(\vec{r})} \quad (2.21)$$

The potential can be applied to come up with a single particle's Hamiltonian, and is given as:

$$H_{K-S} = T_{non} + V_{eff} \quad (2.22)$$

Using the Hamiltonian, Schrödinger equation is presented as:

$$[T_{non} + V_{eff}]\Psi_{K-S} = E\Psi_{K-S} \quad (2.23)$$

The equation (2.23) is what is referred to as Kohn-Sham equation. In this case, the ground-state density $n_{GS}^{K-S}(\vec{r})$ is similar to the ground state wave-function Ψ_{GS}^{K-S} that by definition reduces Kohn-Sham functional subject ortho-normalization constraints $\langle \Psi_i | \Psi_j \rangle = \delta_{ij}$; and it is defined using self-consistent computation [1, 4,21].

The density functional theory utilizes the self-consistent field approach. For instance, assume that E_{xc} and E_{Hart} can be determined accurately. The challenge is that there is

no way V_{eff} can be calculated unless the exact ground-state density is well known. Also, it is challenging to get the correct density from Kohn-Sham wave-functions, unless there is a correct V_{eff} in order to solve the equation (2.23). Thus, this circular problem is solved by conducting a self-consistent cycles [3, 12 and 22] as demonstrated in Fig. 2.1.

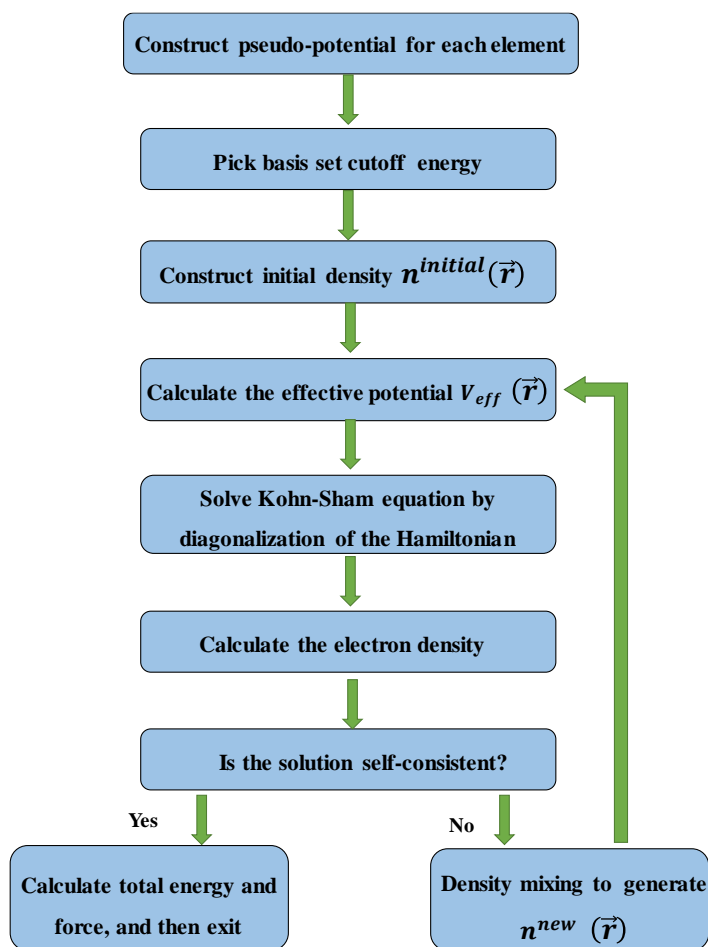


Figure 2.1. A Schematic demonstration of self-consistent DFT cycle.

Based on Fig 2.1, the initial step entails generating a pseudo potential that is able to represent the electrostatic interactions between valence electrons, the nuclei as well as core electrons. The subsequent step entails building the necessary basis set using a

particular kinetic energy cut-off in order to be fixed on the basis set; the aim of this step is to extend the density functional quantity.

Apparently, provided that the density is known, then it is easier to fully determine the energy functional. The trial electronic density $n^{initial}(\vec{r})$ has to be made as the initial guess. The first guess is then employed in order to determine the quantity that follows:

$$G = E_{Hart}[n^{initial}(\vec{r})] + E_{xc}[n^{initial}(\vec{r})] \quad (2.24)$$

Then $\frac{\partial G}{\partial n^{initial}(\vec{r})}$ and the effective potential V_{eff} are calculated. In this case, effective potential V_{eff} is applied to solving the Kohn-Sham equation (2.23) that facilitates the determination of the electron Hamiltonian. Once the electron Hamiltonian is determined, it is then diagonalised so as to identify the eigen functions as well as the new electron density $n^{new}(\vec{r})$. Expectantly, the $n^{new}(\vec{r})$ may be closer to correspond to the exact ground state and it is also checked.

For self-consistency, provided that the new-updated electron density $n^{new}(\vec{r})$ numerically corresponds with density $n^{initial}(\vec{r})$ that is used to come up with Hamiltonian as the start of a SCF cycle, then the end of the loop has been reached. We then exist, as well as calculate the required converged quantities including the electron band-structure, the total energy, states' density among others, otherwise if the new density, $n^{new}(\vec{r})$ fails to correspond to starting density $n^{initial}(\vec{r})$, then one produces another new in-put density and then begins a different SCF cycle: develop a new density-independent Hamiltonian, compute and solve the density. Also, check for self-consistency [3, 17, and 23]. Kohn-Sham technique clearly demonstrated that a complicated many-particles system may be mapped to form a set of the simple non-interacting equations provided that they know the exchange- correlation functional.

Nevertheless, approximations are inevitable, since the exchange correlational function cannot be known precisely.

2.5 The Exchange Correlation Functionals

It is apparent that DFT is one the reliable as well as proven techniques, however it still applies approximation for exchange-correlation functional as well as kinetic energy functional in terms of density E_{xc} . Researchers have done a lot to develop appropriate expressions for these functional. The Local Density Approximation (LDA) [24] is one of the popular exchange-correlation approximations that is employed currently. LDA depends on the density. The other approach is the Generalised Gradient Approximation (GGA) [24], and is a complicated technique that involves the derivatives of density. Moreover it contains information regarding the environment and thus, it is considered semi-local.

2.5.1 Local Density Approximation (LDA)

According to the Kohn-Sham[21] approach, the functional E_{xc} can be computed in homogenous electron- gas in order to estimate the many-particles problem as a very simpler system [11]. Clearly, Kohn-Sham exhibited that if the system's density is varied slowly, then the E_{xc} functional precisely at point \vec{r} can be regarded as the acting in the uniform-density. Thus, E_{xc} functional may be denoted in a uniform electron gas $E_{xc}^{homo}[n(\vec{r})]$ using the density $n(\vec{r})$.

Generally, it is not possible for LDA to work for any system that is dominated with electron-electron interactions. Nevertheless, LDA assumes that in a local-area around any of the considered positions, the density is always a constant and it is presented as [6, 12]:

$$E_{xc}^{LDA}[n(\vec{r})] = \int E_{xc}^{homo}[n(\vec{r})]n(\vec{r})d\vec{r} \quad (2.25)$$

It is possible to split the exchange-correlation energy $E_{xc}^{homo}[n(\vec{r})]$ to form two terms, which includes the sum of the correlation energies $E_c^{homo}[n(\vec{r})]$ as well as the exchange $E_x^{homo}[n(\vec{r})]$. The two are presented separately as shown in the equation that follows:

$$E_{xc}^{homo}[n(\vec{r})] = E_x^{homo}[n(\vec{r})] + E_c^{homo}[n(\vec{r})] \quad (2.26)$$

It is easier to analytically find the exchange term; since it is popular and can be found in a variety of textbooks [6, 16]. It is given as:

$$E_x^{homo}[n(\vec{r})] = -\frac{3}{4} \left(\frac{3n(\vec{r})}{\pi} \right)^{1/3} \quad (2.27)$$

2.5.1 Generalized Gradient Approximation (GGA)

Although real systems are inhomogeneous, LDA treats all the systems as homogenous systems. Taking this into account, a step would be taken beyond LDA as well as extent is to incorporate derivative information of density into exchange-correlation functional. This is done by involving the gradient as well as total charge density's higher spatial derivatives ($|\nabla n(\vec{r})|$, $|\nabla^2 n(\vec{r})|$, ...) into approximation. This functional is also referred to as Generalized Gradient Approximation (GGA). In this case, the exchange part of a functional does not have a closed expression and for this reason, it must be calculate together with correlation contributions by the use of numerical approaches. Similar to the LDA case, there are various parameterizations form exchange correlation energy in a GGA [29-30].

This section entails a discussion about the proposed functional form that was initiated by Perdew, Burke as well as Ernzerhof (PBE) [29]. There are two separate expressions

in this parameterization. The initial expression is known as the exchange $E_x^{GGA}[n(\vec{r})]$.

This expression is presented as:

$$E_x^{GGA}[n(\vec{r})] = \int n(\vec{r}) E_x^{homo}[n(\vec{r})] F_x(s) d\vec{r}, \quad (2.28)$$

$$F_x(s) = 1 + \kappa - \frac{\kappa}{(1 + \mu s^2)/\kappa}$$

Where $F_x(s)$ is referred to as enhancement factor, $\mu = 0.21951$, $\kappa = 0.804$ as well as $s = |\nabla n(\vec{r})|/2k_s n(\vec{r})$ represents a non-dimensional density gradient, in which

$k_s = \sqrt{\frac{4k_{T-F}}{\pi a_0}}$ as well as $k_{T-F} = \frac{(12/\pi)^{1/3}}{\sqrt{r_s}}$ denote the Thomas-Fermi screening wave-

number while r_s represents the local Seitz radius.

2.6 SIESTA

Each of the calculation presented in this thesis were conducted using the SIESTA and DFT code. SIESTA is applied in order to determine the relaxed geometry of the various structure discussed in this thesis. Moreover, it is used to perform calculations in order to explore their electronic properties. The term SIESTA is an acronym that stands for **S**panish Initiative for **E**lectronic **S**imulations with **T**housands of **A**toms. SIESTA is one of the self-consistent density function approach that utilises norm-conserving pseudo-potentials as well as LCAOB (Linear Combination of Atomic Orbital Basis) set in order to conduct efficient calculations [33]. In order to get additional information concerning SIESTA code as well as what it offers (see 34, 35]. When using SIESTA, there are two distinct modes to conduct DFT simulations. First one is the conventional self-consistent field diagonalization approach that solved the Kohn-Sham equations. The second one is by direct reduction of the modified energy functional [36]. In this section, we will describe some components of SIESTA a well as how they are involved in the code.

2.7 Pseudopotentials

In this section, a brief introduction to pseudo-potentials will be presented. Any systems' physical properties are dependent upon an excellent description of its valence electrons distribution. The atom has electrons, which are either define as valence or core electrons. Nevertheless, any typical system with more number of atoms having complex potentials, it is expensive to explore the electronic properties in terms of computer memory as well as time. Through the introduction of an approximation approach known as effective potential or pseudo potential, one is able to decrease the total number of electrons that are engaged in simulation. This is one of the attempts that is aimed at replacing the complicated impact of motion of core electrons (non-valence electrons) of the nucleus as well as the atom through pseudo-potential. This justified by the fact that no core electrons are involved in chemical bonding. Also, core electrons are localized spatially about the atom's nucleus. Moreover, the overlap between their wave-functions and the core electron wave-functions from the surrounding atoms is weak. Because in most of the systems only valence electron states overlap, then it is only such electrons that contribute significantly to the development of molecular orbitals. Thus, it is reasonable to assume that core-electrons can be eliminated and replaced using pseudo-potential. This makes it easier for the coulombic potential terms that is used for core electrons in the Schrödinger equation to be replaced by the modified effective potential term. In 1934, Fermi introduced the initial pseudo-potential approximation and later followed by Hellmann in 1935 [35-38]. Pseudo-potentials have a variety of advantages when they as applied in computational calculations. These advantages include:

1. It eliminates core electron from calculations, thus reducing the number of electrons that are involved in the calculations. This decreases both memory and time that is needed to run ab-initio simulation.
2. It reduced the total energy scale when core-electrons are eliminated from the calculations. Certainly, it stabilises the numerical calculations of the energy differences that is exhibited between atomic configurations.
3. The introduction of pseudo-potentials as well the replacement of true valence wave-functions with pseudo wave-functions, in order to correspond to the exact valence wave-functions outside the cut-off or core radius r_c , however, inside they are nodeless. Such pseudo-wavefunctions may be expanded through the use of lesser number of plane-wave basis states.
4. Another advantage of employing pseudo-potentials involved the ease with which relativistic effects can be incorporated into pseudo-potential while additionally treating non-relativistically the valence electrons.

While solving the Kohn-Sham equation, it is important to start by matching the pseudo-potential's energy eigenvalues with those found in the real potential so as to get a reasonable pseudo-potential. The second step is to ensure the long range pseudo-potential's effect should correspond to that of a real potential. The problem is resolved by ensuring both potential coincide outside the core-radius (r_c).

The pseudo-potential does not match with than of the real potential within a core radius (r_c), and after solving the Kohn-Sham equation using pseudo-potential, the pseudo-wavefunction that is generated does not correspond to the real wave-function within radius r_c . A pseudo-potential is developed in a way that it lack radial nodes within the pseudo-wavefunction in the core. Also, it is clear in that pseudo-potential and

pseudo-wavefunctions coincide with their real potential outside the core region as demonstrated in Fig. 2.2.

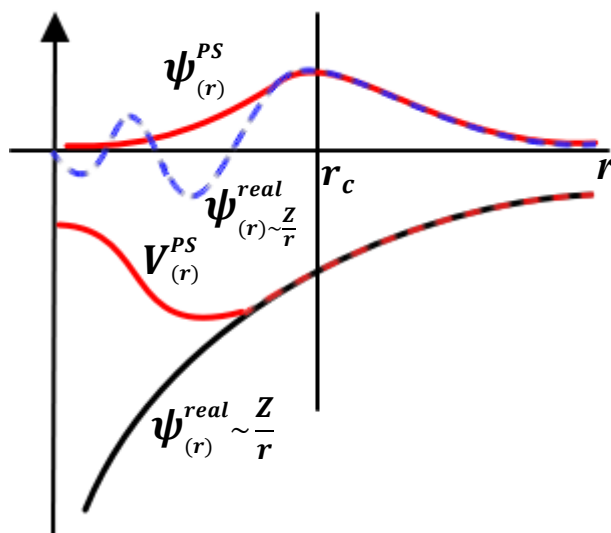


Figure. 2.2. Schematic demonstration of a comparison between the wave-function within the nucleus' Coulomb potential (dashed blue) as well as the ones in pseudo-potential (marked red). Beyond a particular cut-off radius r_c (core radius), both the pseudo-wave function and the wave function correspond to one another.

2.7 Localized Atomic Orbital Basis Sets (LAOBs)

One of the most important aspects of the SIESTA code is the type of the basis function employed in the calculations. It uses a basis set composed of localised atomic orbitals which compare well with other DFT schemes which may use a plane wave function basis set [35]. The benefits from using LAOBs are that they provide a closer representation of the chemical bond; they can allow order-N calculations to be performed and also it gives a good base from which generate a tight-binding Hamiltonian. SIESTA uses confined orbitals, i.e. orbitals are constrained to be zero outside of a certain radius (cutoff radius r_c). This produces the desired sparse form of

the Hamiltonian as the overlap between basis functions is reduced. The atomic orbitals inside this radius are products of a numerical radial function and a spherical harmonic.

The simplest form of the atomic basis set for an atom (labelled as I) is called single- ζ (also called minimal) which represents a single basis function per electron orbital. It is given by the following equation:

$$\Psi_{nlm}^I(\vec{r}) = R_{nl}^I(\vec{r}) Y_{lm}^I(\vec{r}) \quad (2.29)$$

Where $\Psi_{nlm}^I(\vec{r})$ is the single basis function which consists of two parts, the first part is the radial wavefunction R_{nl}^I and the second part is the spherical harmonic Y_{lm}^I . Minimal or single zeta basis set are constructed by using one basis function of each type occupied in the separate atoms that comprise a molecule. If at least one *p*-type orbital is occupied in the atom, then the complete set (*3p*-type) of the functions must be included in the basis set. For example, in the carbon atom, the electron configuration is $1s^2 2s^2 2p^2$, therefore, a minimal basis set for carbon atom consists of $1s, 2s, 2p_x, 2p_y$ and $2p_z$ orbitals which means the total basis functions are five as shown in table 2.1.

Higher accuracy basis sets called multiple- ζ are formed by adding another radial wave function for each included electron orbital. Double basis sets are constructed by using two basis functions of each type for each atom. For carbon atom, a double zeta basis contains ten basis functions corresponding to ten orbitals which are $1s, 1s', 2s, 2s', 2p_x, 2p_x', 2p_y, 2p_y', 2p_z$ and $2p_z'$. For further accuracy, polarisation effects are included in double- ζ polarised basis sets obtained by including wave functions with different angular momenta corresponding to orbitals which are unoccupied in the atom. A polarization function is any higher angular momentum orbital used in a basis set which is unoccupied in the separated atom. As an example,

the hydrogen atom has only one occupied orbital type that is s -type. Therefore, if p -type or d -type basis functions were added to the hydrogen atom they would be known as polarization functions. Carbon atoms with polarization functions include d -type and f -type basis functions.

Table 2.1 Examples of the radial basis sets functions per atom used in SIESTA code for different precisions of the split valence basis sets.

Basis Set	H	C	Au
SZ	1 = (1 × 1s)	4 = (1 × 2s + 3 × 2p)	6 = (1 × 6s + 5 × 5d)
SZP	4 = (1 × 1s + 3 × 2p̃)	9 = (1 × 2s + 3 × 2p + 5 × 3d̃)	9 = (1 × 6s + 5 × 5d + 3 × 6p̃)
DZ	2 = (2 × 1s)	8 = (2 × 2s + 6 × 2p)	12 = (2 × 6s + 10 × 5d)
DZP	5 = (2 × 1s + 3 × 2p̃)	13 = (2 × 2s + 6 × 2p + 5 × 3d̃)	15 = (2 × 6s + 10 × 5d + 3 × 6p̃)

Assuming the core electrons (non-valence electrons) of an atom are less affected by the chemical environment than the valence electrons. This is so-called as split valence basis set. For example, the carbon atom, a split valence double zeta basis set would consist of a single $1s$ orbital, along with $2s, 2s'$ and $2p_x, 2p'_x, 2p_y, 2p'_y, 2p_z, 2p'_z$ orbitals, for a total of 9 basis functions. The basis functions in a split valence double zeta basis set are denoted $1s, 2s, 2s', 2p_x, 2p'_x, 2p_y, 2p'_y, 2p_z, 2p'_z$.

In case of molecules, molecular orbitals can be represented as Linear Combinations of Atomic Orbitals (LCAO-MO) given by:

$$\varphi_i(\vec{r}) = \sum_{v=1}^L a_{vi} \Psi_v(\vec{r}) \quad (2.29)$$

Where φ_i represents the molecular orbitals (basis functions), Ψ_v are atomic orbitals, a_{vi} are numerical coefficients and L is the total number of the atomic orbitals.

2.8 Basis Set Superposition Error Correction (BSSE) and Counterpoise Correction (CP)

BSSE is one of the major factors affecting the accuracy of interaction energy calculations when using incomplete basis sets. It is most often discussed in the context of intermolecular interactions and frequently for weakly interacting systems. The SIESTA implementation of DFT used in this thesis means that the BSSE occurs when using the linear combination of the atomic orbitals formalism which consists of a finite basis set centred on the nuclei, when atoms are close enough to each other so that their basis functions will overlap. This might cause artificial strengthening of the atomic interaction and artificial shortening of the atomic distances and therefore this can affect the total energy of the system.

In 1970, Boys and Bernardi proposed a technique to eliminate the BSSE in molecular complexes composed of two geometric configurations so-called the counterpoise correction (CP) scheme [41-43]. Let us consider two molecular systems which are labelled as A and B . They are separated by a distance R . The energy of the interaction may be expressed as [44]:

$$\Delta E_{inter}^{AB}(\vec{R}) = E^{AB}(\vec{R}) - E^A - E^B \quad (2.30)$$

Where ΔE_{inter}^{AB} is the overall energy of the super system, E^A and E^B are the energies of the isolated subsystems. The form of equation 2.50 shows the counterpoise correction [41]. Figure 2.3 highlights the counterpoise correction for a dimer which are A and B .

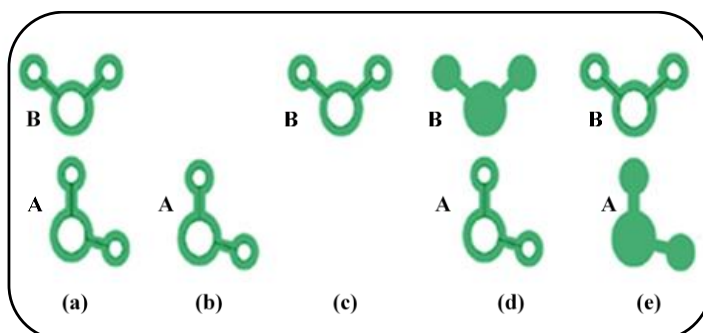


Figure 2.3 Illustrating the Counterpoise method to calculate the binding energy. (a) Represents the basis functions for total system where atoms are white color and the basis functions of the atoms are green. (b) and (c) show the basis function for the individual monomers whereas (d) and (e) represent the counterpoise correction, every single molecule is evaluated with the same basis function as the total system in (a) [42].

In figure 2.3 a, b and c represent the two isolated molecules with their individual and corresponding basis functions while the shaded green atoms in 2.3 d and e represent the ghost states (basis set functions which have no electrons or protons). The BSSE is obtained by recalculating using the mixed basis sets realised by introducing the ghost orbitals, and then subtracting the error from the uncorrected energy to calculate the binding energy E_{Bin} given by:

$$E_{Bin} = E_a - (E_d + E_e) \quad (2.31)$$

Where E_a , E_d and E_e are the total energy of (a), (d) and (e) systems in figure 2.3, respectively. This is an important concept that has been successfully implemented in many systems to give reliable and realistic results and will be utilised in chapter 4 [42, 45,46].

References

- [1] Argaman, N. and G. Makov, Density Functional Theory--an introduction. arXiv preprint physics/9806013, 1998.
- [2] Dronskowski, R., Computational chemistry of solid state materials2005: Wiley Online Library.
- [3] Eschrig, H., The Fundamentals of Density Functional Theory (revised and extended version). Edition am Gutenbergplatz, Leipzig, Germany, 2003. 9.
- [4] Kohn, W., A.D. Becke, and R.G. Parr, Density functional theory of electronic structure. The Journal of Physical Chemistry, 1996. 100(31): p. 12974-12980.
- [5] Martin, R.M., Electronic structure: basic theory and practical methods2004: Cambridge university press.
- [6] Parr, R.G. and Y. Weitao, Density-functional theory of atoms and molecules. Vol. 16. 1994: Oxford University Press, USA.
- [7] Kumar, A., A Brief Introduction to Thomas-Fermi Model in Partial Differential Equations. 2012.
- [8] Lieb, E.H., Thomas-Fermi and related theories of atoms and molecules. Reviews of Modern Physics, 1981. 53(4): p. 603.
- [9] Gross, E.K. and R.M. Dreizler, Density functional theory. Vol. 337. 1995: Springer.
- [10] Hohenberg, P.a.W.K., Inhomogeneous Electron Gas. Physical Review, 1964. 136(3B): p. B864-B871.
- [11] Kohn, W. and L.J. Sham, Self-Consistent Equations Including Exchange and Correlation Effects. Physical Review, 1965. 140(4A): p. A1133-A1138.

- [12] Koch, W. and M.C. Holthausen, A chemist's guide to density functional theory. Vol. 2. 2001: Wiley-Vch Weinheim.
- [13] Geerlings, P., F. De Proft, and W. Langenaeker, Conceptual density functional theory. Chemical Reviews-Columbus, 2003. 103(5): p. 1793-1874.
- [14] Eschrig, H., K. Koepnik, and I. Chaplygin, Density functional application to strongly correlated electron systems. Journal of Solid State Chemistry, 2003. 176(2): p. 482-495.
- [15] Ziesche, P. and F. Tasnádi, Methods for electronic-structure calculations: Overview from a reduced-density-matrix point of view. International journal of quantum chemistry, 2004. 100(4): p. 495-508.
- [16] Thomas, L.H. The calculation of atomic fields. in Mathematical Proceedings of the Cambridge Philosophical Society. 1927. Cambridge Univ Press.
- [17] Burke, K., the ABC of DFT. Department of Chemistry, University of California, 2007.
- [18] Walker, B., C. Molteni, and N. Marzari, Ab initio molecular dynamics of metal surfaces. Journal of Physics: Condensed Matter, 2004. 16(26): p. S2575.
- [19] Kohn, W., Nobel Lecture: Electronic structure of matter—wave functions and density functionals*. Reviews of Modern Physics, 1999. Vol. 71, No. 5: p. 1253-1266.
- [20] Levy, M., Electron densities in search of Hamiltonians. Physical Review A, 1982. 26(3): p. 1200.
- [21] Lima, N., L. Oliveira, and K. Capelle, Density-functional study of the Mott gap in the Hubbard model. EPL (Europhysics Letters), 2007. 60(4): p. 601.
- [22] March, N.H., Self-consistent fields in atoms. 1975.

- [23] Kohn, W. and L.J. Sham, Self-consistent equations including exchange and correlation effects 1965: APS.
- [24] Ceperley, D.M. and B. Alder, Ground state of the electron gas by a stochastic method. *Physical Review Letters*, 1980. 45(7): p. 566-569.
- [25] Perdew, J.P. and A. Zunger, Self-interaction correction to density-functional approximations for many-electron systems. *Physical Review B*, 1981. 23(10): p. 5048-5079.
- [26] Naghavi, S.S., Theoretical Study of correlated systems using hybrid functionals 2011.
- [27] Hedin, L. and S. Lundqvist, Effects of electron-electron and electron-phonon interactions on the one-electron states of solids. *Solid State Physics*, 1970. 23: p. 1-181.
- [28] Vosko, S.H., L. Wilk, and M. Nusair, Accurate spin-dependent electron liquid correlation energies for local spin density calculations: a critical analysis. *Canadian Journal of Physics*, 1980. 58(8): p. 1200-1211.
- [29] Perdew, J.P., K. Burke, and M. Ernzerhof, Generalized gradient approximation made simple. *Physical Review Letters*, 1996. 77(18): p. 3865-3868.
- [30] Becke, A.D., Density-functional exchange-energy approximation with correct asymptotic behavior. *Physical Review A*, 1988. 38(6): p. 3098.
- [31] Hammer, B., L.B. Hansen, and J.K. Nørskov, Improved adsorption energetics within density-functional theory using revised Perdew-Burke-Ernzerhof functionals. *Physical Review B*, 1999. 59(11): p. 7413.

- [32] Perdew, J.P. and Y. Wang, Accurate and simple analytic representation of the electron-gas correlation energy. *Physical Review B*, 1992. 45(23): p. 13244-13249.
- [33] Soler, J.M., et al., The SIESTA method for ab initio order-N materials simulation. *Journal of Physics: Condensed Matter*, 2002. 14(11): p. 2745.
- [34] Sánchez-Portal, D., et al., Density-functional method for very large systems with LCAO basis sets. *International journal of quantum chemistry*, 1998. 65(5): p. 453-461.
- [35] E. Artacho, J.D.G., A. Junquera, R. M. Martin, P. Ordejon, D. Sanchez-Portal, and J. M. Soler. *SIESTA 3.1 User's Guide*. 2011.
- [36] Ordejón, P., et al., Unconstrained minimization approach for electronic computations that scales linearly with system size. *Physical Review B*, 1993. 48(19): p. 14646.
- [37] Kleinman, L. and D. Bylander, Efficacious form for model pseudopotentials. *Physical Review Letters*, 1982. 48(20): p. 1425-1428.
- [38] Hamann, D., M. Schlüter, and C. Chiang, Norm-conserving pseudopotentials. *Physical Review Letters*, 1979. 43(20): p. 1494-1497.
- [39] Troullier, N. and J.L. Martins, Efficient pseudopotentials for plane-wave calculations. *Physical Review B*, 1991. 43(3): p. 1993.
- [40] Troullier, N. and J. Martins, A straightforward method for generating soft transferable pseudopotentials. *Solid State Communications*, 1990. 74(7): p. 613-616.

- [41] Boys, S. and F.d. Bernardi, The calculation of small molecular interactions by the differences of separate total energies. Some procedures with reduced errors. *Molecular Physics*, 1970. 19(4): p. 553-566.
- [42] Haynes, P., et al., Elimination of basis set superposition error in linear-scaling density-functional calculations with local orbitals optimised in situ. *Chemical physics letters*, 2006. 422(4): p. 345-349.
- [43] Mierzwicki, K., & Latajka, Z. (2003). Basis set superposition error in N-body clusters. *Chemical physics letters*, 380(5-6), 654-664..
- [44] Senent, M. and S. Wilson, Intramolecular basis set superposition errors. *International journal of quantum chemistry*, 2001. 82(6): p. 282-292.
- [45] Daza, M.C., et al., Basis set superposition error-counterpoise corrected potential energy surfaces. Application to hydrogen peroxide... X (X= F⁻, Cl⁻, Br⁻, Li⁺, Na⁺) complexes. *The Journal of Chemical Physics*, 1999. 110(24): p. 11806-11813.
- [46] Boese, A.D., et al., Effects of counterpoise correction and basis set extrapolation on the MP2 geometries of hydrogen bonded dimers of ammonia, water, and hydrogen fluoride. *Phys. Chem. Chem. Phys.*, 2010. 13(3): p. 1230-1238.

Chapter 3

3. Single Particle Transport

3.1 Introduction

The aim of studying molecular electronics is to comprehend electrical properties of molecular junctions. In this case, a specifically small structure (or molecule) is attached to the main part of electrodes to allow elastic transport to occur among its energy levels. The strength of the bond between the molecule and the leads is typically smaller than the intra-molecule or intra-electrode bond strengths. This presents a scattering activity from the molecule to the electrode and from the electrode to the molecule.

This chapter starts with a brief summary of the Landauer formula. After this, the most straight forward formula of Green's function for a simplistic tight binding strand will be introduced. These simple systems use methods that are useful in the derivation of the transmission coefficient of randomly complex geometry's mesoscopic conductors.

3.2 The Landauer Formula

An established method to describe transport process in mesoscopic systems is the Landauer formula [1, 2]. It relates the mesoscopic sample conductance to the transmission characteristics of electrons travelling through it. Towards the end of this chapter, the techniques used to estimate the transmission properties will be elaborated.

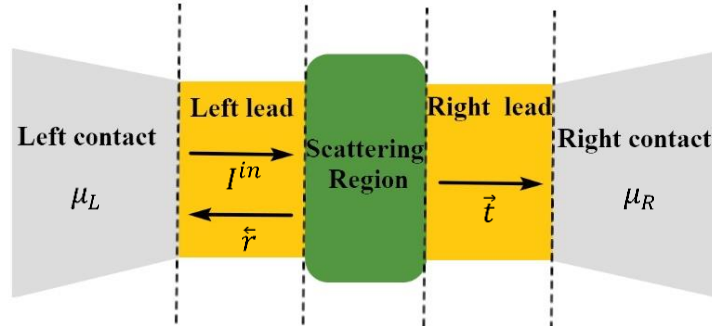


Figure 3.1: A mesoscopic scatterer connected to contacts by ballistic leads. The chemical potentials in the left and right contacts are μ_L and μ_R respectively. If an incident wave packet hits the scatterer from the left, it will be transmitted to the right with probability $T = |\vec{t}|^2 = \vec{t}\vec{t}^*$ and reflected with probability $R = |\vec{r}|^2 = \vec{r}\vec{r}^*$. Since incident electrons must be either reflected or transmitted, probability conservation implies $R + T = 1$.

The above figure represents a mesoscopic scatterer linked to two contacts, which act like electron reservoirs, using two perfect ballistic leads (Figure 3.1). Every inelastic relaxation process is restricted to the reservoirs [3]. These reservoirs contain somewhat different chemical potentials ($\mu_L > \mu_R \Rightarrow \mu_L - \mu_R = \delta E = e\delta V > 0$) which is expected to pump electrons from the left to the right reservoir. To begin with, the solution for one open channel (wherein only a single electron is permitted to travel in a particular direction) will be discuss.

Before finding the current in this system, the δI^{in} (incident electric current) generated by the chemical potential difference will be analysed first:

$$\delta I^{in} = ev_g \frac{\partial n}{\partial E} \delta E = ev_g \frac{\partial n}{\partial E} (\mu_L - \mu_R) \quad (3.1)$$

Where e represent the electronic charge, v_g represents the group velocity, and $\partial n/\partial E$ represents the *DOS* (density of states) per unit length in the lead found in the energy gap described by the contacts' chemical potentials:

$$DOS = \frac{\partial n}{\partial E} = 2 \left(\frac{\partial n}{\partial k} \frac{\partial k}{\partial E} \right) \quad (3.2)$$

Wherein the factor of 2 stands for the spin. In one dimension, $\partial k / \partial E = 1 / \hbar v_g$ and $\partial n / \partial k = 1 / 2\pi$. This modifies equation (3.1) to:

$$\delta I^{in} = \frac{2e}{h} (\mu_L - \mu_R) = \frac{2e^2}{h} \delta V \quad (3.3)$$

Where, δV stands for the voltage related to the chemical potential difference. Equation (3.3) prove that without a scattering site, the conductance of a quantum wire with a single free channel is $2e^2/h$ which is roughly $77.5 \mu S$ (to be more specific, a $12.9 k\Omega$ resistance). The quantity is reasonable and it characteristically appears on the nameplates of ordinary electrical appliances.

Taking into account a scattering site, the collected current in the right contacts (δI^{out}) can be found by:

$$\delta I^{out} = \delta I^{in} T = \frac{2e^2}{h} T \delta V \Rightarrow \frac{\delta I^{out}}{\delta V} = \frac{2e^2}{h} T = G \quad (3.4)$$

The above equation is the renowned Landauer formula, connecting G (the conductance), of a mesoscopic scatterer to T (the transmission probability) of the electrons flowing through it. This defines the linear response conductance, and it therefore only applies for small bias voltages $\delta V \approx 0$.

Büttiker has generalized the Landauer formula for the case of more than one open channel [2]. In such a case, the transmission coefficient is substituted by the total transmission amplitudes which explain incoming electrons from the left contact and approaching the right contact. The open channels Landauer formula (equation (3.3)) hence turns into:

$$\frac{\delta I^{out}}{\delta V} = G = \frac{2e^2}{h} \sum_{ij} |\vec{t}_{ij}|^2 = \frac{2e^2}{h} \text{Trace} (\vec{t}\vec{t}^\dagger) \quad (3.5)$$

Where \vec{t}_{ij} is the transmission amplitude describing scattering from the j^{th} channel of the left lead to the i^{th} channel of the right lead. From the description of the transmission amplitudes, it is possible to derive the reflection amplitudes \vec{r}_{ij} which defines the scattering activities in which a particle is scattered from the left lead's j^{th} channel to the i^{th} channel of the left lead. The S matrix is an object that can be defined by combining transmission and reflection amplitudes. It links states from the right lead to the left lead and the opposite is also true:

$$S = \begin{pmatrix} \vec{r} & \vec{t} \\ \vec{t} & \vec{r} \end{pmatrix} \quad (3.6)$$

Where, \vec{r} and \vec{t} describe electrons coming from the left, while \vec{r} and \vec{t} describe electrons coming from the right. Equation (3.5) demonstrates that $\vec{r}, \vec{t}, \vec{t}$ and \vec{r} are complex matrices for at least one channel (for instance in the presence of a magnetic field). However, charge conservation requires that the S matrix be unitary $SS^\dagger = I$. This S matrix is a building block of the scattering theory. The S matrix is not only useful in defining transport in the linear response system, but also in other issues, including adiabatic pumping [4].

3.3. Tight-Binding Model

A tight binding model is a simple way to describe the electronic structure of molecules and solids [36]. In this work, I will also use the tight binding model (TBM) which assume sthat the electrons in a solid are tightly bound that only interact with nearest neighbours. This is a good approximation in many physical problems when the wave

function at the individual atomic sites decay to zero before they reach the second nearest neighbour.

A simple TB description of system could be constructed by assigning a *Hückel* parameter to the on-site energy ε of each atom in the molecule connected to the nearest neighbors with a single Hückel parameter (hopping matrix element) γ as shown in figure (3.3.1).

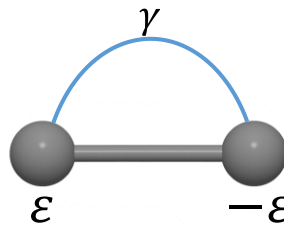


Figure 3.2: A simple Tight Binding Hamiltonian for a close system of two single-orbital sites with on-site energies ε and $-\varepsilon$ coupled to each other by the hopping integral γ .

The most general Schrödinger equation¹ describes the evolution of physical properties of a system in time and was proposed by the Austrian physicist Erwin Schrödinger in 1926 as:

$$i\hbar \frac{d}{dt} \psi(r, t) = \hat{H} \psi(r, t) \quad (3.7)$$

Where ψ is the wave function of the quantum system, and \hat{H} is the Hamiltonian operator which characterizes the total energy of any given wave function and \hbar is the reduced Planck constant ($\frac{h}{2\pi}$), r and t are the position vector and time respectively.

For Time-independent Schrödinger equation it could be written such as next equation:

$$H\psi(x) = E\psi(x) \quad (3.8)$$

$$\det(EI - H) = 0 \quad (3.9)$$

The Hamiltonian expression can therefore be written in matrix form as shown below:

$$H = \begin{pmatrix} \varepsilon & \gamma \\ \gamma^* & -\varepsilon \end{pmatrix} \quad (3.10)$$

Then by analyzing the last equation:

$$\det \left(\begin{pmatrix} E & 0 \\ 0 & E \end{pmatrix} - \begin{pmatrix} \varepsilon & \gamma \\ \gamma^* & -\varepsilon \end{pmatrix} \right) = 0 \quad (3.11)$$

$$\det \begin{pmatrix} E - \varepsilon & -\gamma \\ -\gamma^* & E + \varepsilon \end{pmatrix} = 0 \quad (3.12)$$

The eigenvalues from the Hamiltonian are:

$$E_{\pm} = \pm \sqrt{\varepsilon^2 + |\gamma|^2} \quad (3.13)$$

Next equations shows eigenvectors

$$|\psi_1\rangle = \begin{pmatrix} u_1 \\ v_1 \end{pmatrix} \quad (3.14)$$

$$|\psi_2\rangle = \begin{pmatrix} u_2 \\ v_2 \end{pmatrix} \quad (3.15)$$

Where is

$$|u_1|^2 = \frac{1}{2} \left(1 + \frac{\varepsilon}{E} \right) \quad (3.16)$$

$$|v_1|^2 = \frac{1}{2} \left(1 - \frac{\varepsilon}{E} \right) \quad (3.17)$$

$$|u_2|^2 = \frac{1}{2} \left(1 + \frac{\varepsilon}{E} \right) \quad (3.18)$$

$$|v_2|^2 = \frac{1}{2} \left(1 - \frac{\varepsilon}{E} \right) \quad (3.19)$$

3.4 One-Dimension

As an example, I shall work out the scattering matrix for a simple one-dimensional system prior to presenting the generalized methodology. In so doing, the outline of the methodology used will be made clear. Green's functions will be useful in the derivation and therefore, there is need to first describe the type of the Green's function for a one dimensional separated lattice before evaluating the scattering medium of a one-dimensional scatterer.

3.4.1 A Perfect One-Dimensional Lattice

Here, we shall discuss the type of the Green's function for a simple endless one-dimensional sequence with hopping parameters ($-\gamma$) and on-site energies (ε_o) as illustrated in Figure 3.4.1.

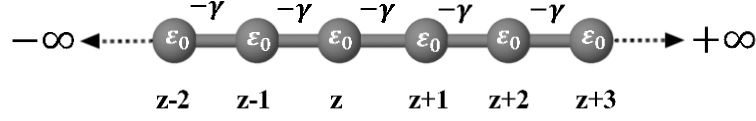


Figure 3.4.1: Tight-binding approximation of a one-dimensional periodic lattice with on-site energies ε_o and couplings $-\gamma$.

Infinitely, the Hamiltonian is built with the hopping elements ($-\gamma$) along the first off-diagonal and the on-site energies (ε_o) along the diagonal. The Hamiltonian expression can therefore be written in matrix form as shown below:

$$H = \begin{pmatrix} \bullet & \bullet & 0 & 0 & 0 & 0 & 0 & 0 \\ \bullet & \bullet & \bullet & 0 & 0 & 0 & 0 & 0 \\ 0 & \bullet & \varepsilon_o & -\gamma & 0 & 0 & 0 & 0 \\ 0 & 0 & -\gamma^* & \varepsilon_o & -\gamma & 0 & 0 & 0 \\ 0 & 0 & 0 & -\gamma^* & \varepsilon_o & -\gamma & 0 & 0 \\ 0 & 0 & 0 & 0 & -\gamma^* & \varepsilon_o & \bullet & 0 \\ 0 & 0 & 0 & 0 & 0 & 0 & \bullet & \bullet \\ 0 & 0 & 0 & 0 & 0 & 0 & 0 & \bullet \end{pmatrix} \quad (3.20)$$

Substituting equation (3.20) and the wave function into the Schrödinger equation $H|\psi\rangle = E|\psi\rangle$, and using an accurate approximation, we get:

$$\begin{pmatrix} \bullet & \bullet & \bullet & \bullet & \bullet & \bullet & \bullet & \bullet \\ \bullet & \bullet & \bullet & \bullet & \bullet & \bullet & \bullet & \bullet \\ \bullet & -\gamma^* & (E - \varepsilon_o) & -\gamma & 0 & 0 & 0 & \bullet \\ \bullet & 0 & -\gamma^* & (E - \varepsilon_o) & -\gamma & 0 & 0 & \bullet \\ \bullet & 0 & 0 & -\gamma^* & (E - \varepsilon_o) & -\gamma & 0 & \bullet \\ \bullet & 0 & 0 & 0 & -\gamma^* & (E - \varepsilon_o) & -\gamma & \bullet \\ \bullet & \bullet & \bullet & \bullet & \bullet & \bullet & \bullet & \bullet \\ \bullet & \bullet & \bullet & \bullet & \bullet & \bullet & \bullet & \bullet \end{pmatrix} \begin{pmatrix} \bullet \\ \bullet \\ \Psi_{(z-1)} \\ \Psi_{(z)} \\ \Psi_{(z+1)} \\ \Psi_{(z+2)} \\ \bullet \\ \bullet \end{pmatrix} = \begin{pmatrix} \bullet \\ \bullet \\ 0 \\ 0 \\ 0 \\ 0 \\ \bullet \\ \bullet \end{pmatrix} \quad (3.21)$$

We may now come up with the Schrödinger equation for H (Hamiltonian) row z as:

$$-\gamma^* \Psi_{(z-1)} + (E - \varepsilon_o) \Psi_{(z)} - \gamma \Psi_{(z+1)} = 0 \quad (3.22)$$

Hence the fact that equation (3.22) satisfies the Schrödinger equation qualifies any function $\Psi_{(z)}$ to be a wave function. The wave function for this ideal lattice assumes the formula of a propagation Bloch state (equation (3.23)), normalised by its group v_g (velocity) to enable it to transport a unit current flux. Substituting this into

equation (3.22), assuming $\gamma = \gamma^*$, i.e. if γ is real, it results in the famous expression and supposed one-dimensional energy distribution equation (equation (3.24)):

$$\Psi_{(z)} = \frac{1}{\sqrt{v_g}} e^{ikz} \tag{3.23}$$

$$E = \varepsilon_o - 2\gamma \cos k \tag{3.24}$$

Wherein, we presented the k (quantum number) usually known as the wave number. The $\mathcal{G}(z, z')$ (retarded Green's function) is associated with the wavefunction and is really the product of an equation identical to the Schrödinger equation:

$$\left. \begin{aligned} (E - H) \mathcal{G}(z, z') &= \delta_{(z, z')} \Rightarrow \\ -\gamma^* \mathcal{G}(z - 1, z') + (E - \varepsilon_o) \mathcal{G}(z, z') - \gamma \mathcal{G}(z + 1, z') &= \delta_{(z, z')} \end{aligned} \right\} \tag{3.25}$$

Here,

$$\delta_{(z, z')} = 1, \quad \text{if } z = z'$$

$$\delta_{(z, z')} = 0, \quad \text{if } z \neq z'$$

Physically, the retarded Greens function, $\mathcal{G}(z, \acute{z})$, describes the response of a system at a point z due to a source at a point \acute{z} . Intuitively, we expect such an excitation to give rise to two waves, traveling outwards from the point of excitation, with amplitudes A^+ and A^- as shown in figure 3.4

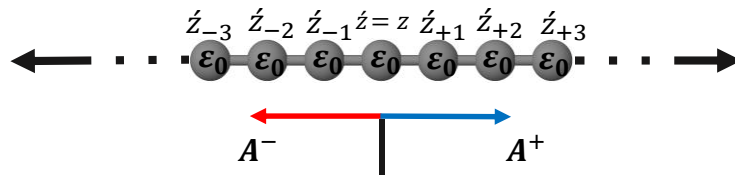


Figure 3.4 Retarded Green's Function of an infinite one-dimensional lattice. The Excitation at $l = j$ causes wave to propagate left and right with amplitudes A^- and A^+ Respectively.

These waves can be expressed simply as:

$$\begin{aligned} g(\acute{z}, z) &= A^+ e^{ikz} & z > \acute{z} \\ g(\acute{z}, z) &= A^- e^{-ikz} & z < \acute{z} \end{aligned} \quad (3.26)$$

Except at $z = z'$, this outcome complies with equation (3.25) at all points. The Green's function must be constant to overcome this, so we relate the two at $z = z'$:

$$A^+ e^{ik\acute{z}} = A^- e^{-ik\acute{z}} \quad (3.27)$$

$$A^- = A^+ e^{2ik\acute{z}} \quad (3.28)$$

Substituting Eq. 3.28 into the Green's functions (Eq.(3.26)) yields:

$$\begin{aligned} g(\acute{z}, z) &= A^+ e^{ik\acute{z}} e^{ik(z-\acute{z})} & \acute{z} > z \\ g(\acute{z}, z) &= A^+ e^{ik\acute{z}} e^{ik(\acute{z}-z)} & \acute{z} < z \end{aligned} \quad (3.29)$$

With a little thought, it is clear that this can be written simply as:

$$g(z, \acute{z}) = A^+ e^{ik\acute{z}} e^{ik|z-\acute{z}|} \quad (3.30)$$

Where

$$A^+ = \frac{e^{-ik\acute{z}}}{i\hbar v} \quad (3.31)$$

$$\text{Hence } g(z, \acute{z}) = \frac{e^{ik|z-\acute{z}|}}{i\hbar v} \quad (3.32)$$

Where the group velocity, found from the dispersion relation, is:

$$v = \frac{dE(k)}{\hbar dk} = \frac{2\gamma \sin(k)}{\hbar} \quad (3.32)$$

A more thorough derivation can be found in the literature [37, 38 and 39].

3.4.2 One-Dimensional Scattering

This section presents two elements of one-dimensional close-fitting semi-infinite leads bound by $-\alpha$ (connector element). The two leads possess the same ε_0 (on-site potentials) and $-\gamma$ (hopping elements) as illustrated in figure 3.4.2. Though it is apparently simple, such a system is misleading as every one-dimensional setup can be

condensed back to this topology. The methodical solutions for the reflection and transmission coefficients would therefore be very important.

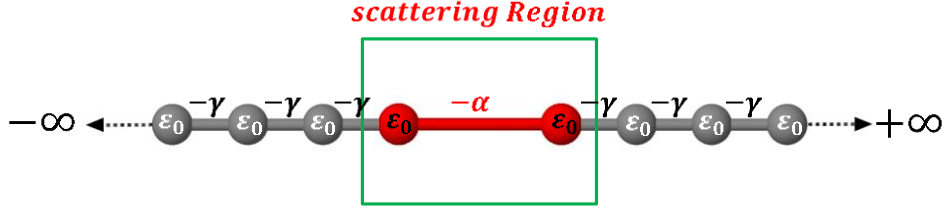


Figure 3.4.2: Simple tight-binding model of a one dimensional scatterer attached to one dimensional leads.

To begin with, there is need to express a H , which appears to an infinite matrix.

$$H = \begin{pmatrix} \bullet & \bullet & 0 & 0 & 0 & 0 & 0 & 0 \\ \bullet & \bullet & -\gamma & 0 & 0 & 0 & 0 & 0 \\ 0 & -\gamma^* & \epsilon_o & -\gamma & 0 & 0 & 0 & 0 \\ 0 & 0 & -\gamma^* & \epsilon_o & -\alpha & 0 & 0 & 0 \\ 0 & 0 & 0 & -\alpha^* & \epsilon_o & -\gamma & 0 & 0 \\ 0 & 0 & 0 & 0 & -\gamma^* & \epsilon_o & -\gamma & 0 \\ 0 & 0 & 0 & 0 & 0 & -\gamma^* & \bullet & \bullet \\ 0 & 0 & 0 & 0 & 0 & 0 & \bullet & \bullet \end{pmatrix} = \begin{pmatrix} H_L & V_c \\ V_c^\dagger & H_R \end{pmatrix} \quad (3.33)$$

Where, H_L and H_R symbolise Hamiltonians for semi-infinite leads equivalent to the Hamiltonian, while V_c signifies the coupling factor. Equation (3.24) gave the dispersion relationship equivalent to the leads given above and equation (3.32) gave the group velocity for real γ :

$$E(k) = \epsilon_o - 2\gamma \cos k \quad (3.34)$$

And

$$v_g = \frac{1}{\hbar} \frac{\partial E}{\partial k} \quad (3.35)$$

For us to get the scattering amplitudes, we must work out the Green's function of the scheme and it can be given as:

$$(E - H)G = I \Rightarrow G = (E - H)^{-1} \quad (3.36)$$

If the energy E is equivalent to the Hamiltonian H 's eigenvalues, Equation (3.36) would be singular. It is important to take into account the limit below to avoid such a problem:

$$G_{\mp} = \lim_{\eta \rightarrow 0} (E - H \mp i\eta)^{-1} \quad (3.37)$$

Here, η denotes a positive number, while G_- (G_+) denotes the advanced (retarded) Green's function. Only Retarded Green's functions will be applied in this paper and hence the negative sign will be chosen. Equation (3.32) described the retarded Green's function for an infinite one dimensional chain having similar parameters:

$$g_{ml} = \frac{1}{i\hbar v_g} e^{ik|m-l|} \quad (3.38)$$

Where, m and l represents the tags of the sites along the chain. There is need to familiarise ourselves with the suitable boundary conditions for us to derive the Green's function of a partially infinite lead. For this reason, and due to semi-infinite nature of the lattice, the chain should end at a particular point (i_o) making every point for which $i \leq i_o$ to vanish. This is possible when a wave function is added to the Green's function to accurately embody this situation. In this case, the wave function becomes:

$$\Psi_{ml}^{i_o} = -\frac{e^{ik(2i_o-m-l)}}{i\hbar v_g} \quad (3.39)$$

The summation of equations (3.38) and (3.39) ($g_{ml} = g_{ml}^{\infty} + \Psi_{ml}^{i_o}$) yields Green's function and will have the simple form at the boundary ($m = l = i_o - 1$) shown below:

$$g_{i_o-1, i_o-1} = -\frac{e^{ik}}{\gamma} \quad (3.40)$$

Consider the instance of detached leads ($\alpha = 0$), the sum of Green's function of the system can be given by the detached Green's function:

$$\mathcal{G} = \begin{pmatrix} -\frac{e^{ik}}{\gamma} & 0 \\ 0 & -\frac{e^{ik}}{\gamma} \end{pmatrix} = \begin{pmatrix} \mathcal{G}_L & 0 \\ 0 & \mathcal{G}_R \end{pmatrix} \quad (3.41)$$

On switching on the contact, the Green's function of the coupled system (G) will be obtained. At this point, Dyson's equation will be used:

$$G = (\mathcal{G}^{-1} - V)^{-1} \quad (3.42)$$

Wherein the operator V defining the link between the two leads will look like:

$$V = \begin{pmatrix} 0 & V_c \\ V_c^\dagger & 0 \end{pmatrix} = \begin{pmatrix} 0 & \alpha \\ \alpha^* & 0 \end{pmatrix} \quad (3.43)$$

The outcome of equation (3.41) (Dyson's equation) reads:

$$G = \frac{1}{\gamma^2 e^{-2ik} - \alpha^2} \begin{pmatrix} -\gamma e^{-ik} & \alpha \\ \alpha^* & -\gamma e^{-ik} \end{pmatrix} \quad (3.44)$$

At this point, the Green's function equation (3.44) will be employed in the calculation of the reflection (\tilde{r}) and transmission (\tilde{t}) amplitudes. This is achieved through the use of the Fisher-Lee equation [3, 8] which compares the Green's function of the problem to the scattering amplitudes of a scattering problem. The Fisher-Lee expressions in this context are written as:

$$\tilde{r} = G_{1,1} v_g - 1 \quad (3.45)$$

And

$$\tilde{t} = G_{1,2} v_g e^{ik} \quad (3.46)$$

Such amplitudes match with the charges coming from the left. Similar relations may be used for the reflection (\tilde{r}) and transmission (\tilde{t}) amplitudes when charges coming from the right are considered.

With the full scattering matrix at hand, we may apply the Landauer formula (equation (3.4)) in the calculation of the zero bias conductance. The process of finding this systematic solution for a one-dimensional scatterer's conductance can be simplified for more complex problems. The steps can be summarized as follows:

- a. First, calculate the Green's function defining the surface regions of the leads.
- b. Use Dyson's equation to obtain the whole Green's function in the existence of a scatterer.
- c. Make use of the Fisher-Lee relation to get the scattering matrix from the Green's function.
- d. Finally, use Landauer formula to find the zero-bias conductance.

Despite the fact that the setup addressed in this section looks simple, we shall make sure that it is quite general since every type of scattering site can be diminished to be equal to the two one dimensional leads by the use of a method called decimation.

3.5 Transport through an arbitrary scattering region

In this section I will derive the most general formula for the transmission probability for an arbitrarily scattering structure. Here I will use a different approach starting with the wave functions leading to the surface Green's function and ending up with a general formula for the transmission probability.

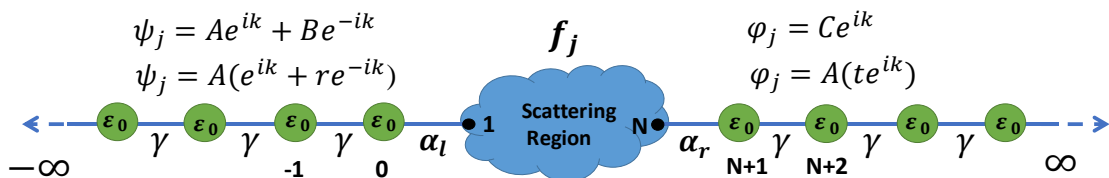


Figure 3.5 Tight-binding representation of a one dimensional arbitrarily scattering region attached to one dimensional lead.

$$\varepsilon_r \varphi_j - \gamma_r \varphi_{j+1} - \gamma_r \varphi_{j-1} = E \varphi_j \quad \text{for } j > N + 1 \quad (3.50)$$

$$\varepsilon_r \varphi_{N+1} - \gamma_r \varphi_{N+2} - \alpha_r f_N = E \varphi_{N+2} \quad \text{for } j = N + 1 \quad (3.51)$$

Where g is the Green's function:

$$\begin{pmatrix} f_1 \\ \vdots \\ f_N \end{pmatrix} = \begin{pmatrix} g_{11} & \cdots & g_{1N} \\ \vdots & \ddots & \vdots \\ g_{1N} & \cdots & g_{NN} \end{pmatrix} \begin{pmatrix} -\alpha_l \psi_0 \\ 0 \\ -\alpha_r \varphi_{N+1} \end{pmatrix} \quad (3.52)$$

$$f_1 = -g_{11} \alpha_l \psi_0 - g_{1N} \alpha_r \varphi_{N+1} \quad (3.53)$$

$$f_N = -g_{N1} \alpha_l \psi_0 - g_{NN} \alpha_r \varphi_{N+1} \quad (3.54)$$

By substituting (3.48) in (3.54) and (3.53)

$$-g_{11} \alpha_l \psi_0 - g_{1N} \alpha_r \varphi_{N+1} = \frac{\gamma_l}{\alpha_l} \psi_1 \quad (3.55)$$

$$-g_{N1} \alpha_l \psi_0 - g_{NN} \alpha_r \varphi_{N+1} = \frac{\gamma_r}{\alpha_r} \varphi_N \quad (3.56)$$

As we know that the wave function in the left site is $\psi_j = e^{ik_l j} + r e^{-ik_l j}$ and for the right side is $\varphi_j = t e^{-ik_r j}$ now substitute $j=1$ in left side

$$\psi_1 = e^{ik_l} + r e^{-ik_l} \quad (3.57)$$

Now add and subtract e^{-ik_l} in last equation

$$\psi_1 = e^{ik_l} + r e^{-ik_l} + e^{-ik_l} - e^{-ik_l} \quad (3.58)$$

$$\psi_1 = 2i \sin k_l + e^{-ik_l} (r + 1)$$

$$\psi_1 = 2i \sin k_l + e^{-ik_l} \psi_0$$

$$\varphi_j = t e^{-ik_r j} \quad (3.59)$$

By substituting $j=N$

$$\varphi_N = t e^{-ik_r N} \quad (3.60)$$

$$\varphi_{N+1} = t e^{-ik_r (N+1)} \quad (3.61)$$

$$\varphi_N = \varphi_{N+1} e^{-ik_r} \quad (3.62)$$

Now take a value of φ_N and ψ_1 and substitute in to equation (3.55), (3.56)

$$-g_{11}\alpha_l\psi_0 - g_{1N}\alpha_r\varphi_{N+1} = \frac{\gamma_l}{\alpha_l}\psi_1 = \frac{\gamma_l}{\alpha_l}(2isink_l + e^{-ik_l}\psi_0) \quad (3.63)$$

$$-g_{N1}\alpha_l\psi_0 - g_{NN}\alpha_r\varphi_{N+1} = \frac{\gamma_r}{\alpha_r}\varphi_N = \frac{\gamma_r}{\alpha_r}\varphi_{N+1}e^{-ik_r} \quad (3.64)$$

Rewrite 7 and 8

$$\left(-g_{11}\alpha_l - \frac{\gamma_l}{\alpha_l}e^{-ik_l}\right)\psi_0 + (g_{1N}\alpha_r)\frac{\gamma_l}{\alpha_l}\varphi_{N+1} = \frac{\gamma_l}{\alpha_l}2isink_l \quad (3.65)$$

$$\left(-g_{NN}\alpha_r - \frac{\gamma_r}{\alpha_r}e^{-ik_r}\right)\varphi_{N+1} + (g_{N1}\alpha_r)\psi_0 = 0 \quad (3.66)$$

$$\begin{pmatrix} -g_{11}\alpha_l - \frac{\gamma_l}{\alpha_l}e^{-ik_l} & -g_{1N}\alpha_r \\ -g_{N1}\alpha_l & -g_{NN}\alpha_r - \frac{\gamma_r}{\alpha_r}e^{-ik_r} \end{pmatrix} \begin{pmatrix} \psi_0 \\ \varphi_{N+1} \end{pmatrix} = \frac{\gamma_l}{\alpha_l}2isink_l \begin{pmatrix} 1 \\ 0 \end{pmatrix} \quad (3.67)$$

$$\begin{pmatrix} -g_{11}\alpha_l - \frac{\gamma_l}{\alpha_l}e^{-ik_l} & -g_{1N}\alpha_r \\ -g_{N1}\alpha_l & -g_{NN}\alpha_r - \frac{\gamma_r}{\alpha_r}e^{-ik_r} \end{pmatrix} = A$$

$$\begin{pmatrix} \psi_0 \\ \varphi_{N+1} \end{pmatrix} = \frac{\gamma_l}{\alpha_l}2isink_l A^{-1} \begin{pmatrix} 1 \\ 0 \end{pmatrix}$$

$$\begin{pmatrix} \psi_0 \\ \varphi_{N+1} \end{pmatrix} = \frac{\gamma_l}{\alpha_l}2isink_l \frac{1}{\det} \begin{pmatrix} -g_{NN}\alpha_r - \frac{\gamma_r}{\alpha_r}e^{-ik_r} \\ g_{N1}\alpha_r \end{pmatrix} \quad (3.68)$$

$$\begin{aligned} \det A &= \left(-g_{11}\alpha_l - \frac{\gamma_l}{\alpha_l}e^{-ik_l}\right)\left(-g_{NN}\alpha_r - \frac{\gamma_r}{\alpha_r}e^{-ik_r}\right) - (-g_{1N}\alpha_r)(-g_{N1}\alpha_r) \\ &= e^{-ik_l} \cdot e^{-ik_r} \frac{\gamma_r\gamma_l}{\alpha_r\alpha_l} \left[e^{-ik_l} \cdot e^{-ik_r} \frac{\alpha_l^2\alpha_r^2}{\gamma_r\gamma_l} (-g_{11}g_{NN} - g_{1N}g_{N1}) + \frac{\alpha_l^2}{\gamma_l}g_{11} \cdot e^{ik_r} + \right. \\ &\quad \left. \frac{\alpha_r^2}{\gamma_r}g_{NN} \cdot e^{ik_r} + 1 \right] \quad (3.69) \end{aligned}$$

$$\Delta = \left[e^{-ik_l} \cdot e^{-ik_r} \frac{\alpha_l^2\alpha_r^2}{\gamma_r\gamma_l} (-g_{11}g_{NN} - g_{1N}g_{N1}) + \frac{\alpha_l^2}{\gamma_l}g_{11} \cdot e^{ik_r} + \frac{\alpha_r^2}{\gamma_r}g_{NN} \cdot e^{ik_r} \right] \quad (3.70)$$

$$\det A = e^{-ik_l} \cdot e^{-ik_r} \frac{\gamma_r\gamma_l}{\alpha_r\alpha_l} [\Delta + 1] \quad (3.71)$$

$$T = |\varphi_{N+1}|^2 = t e^{-ik_r j} \cdot t^* e^{-ik_r j} \quad (3.72)$$

$$= tt^* = |t|^2 \quad (3.73)$$

$$T = \left(\frac{\alpha_l}{\gamma_l}\right)^2 \left(\frac{\alpha_r}{\gamma_r}\right)^2 r_l^2 \frac{|g_{N1}|^2}{|\Delta+1|^2} \quad (3.74)$$

Equation (3.74) is the most general formula to calculate the transmission probability for any scattering region connected to identical leads.

The completely general technique for calculating Green's function and a scattering S matrix and transport coefficient of a finite super-lattice connected to crystalline semi-infinite leads can be found in [10].

3.6 Calculation in Practice

Over the last decade, the proposed method has been applied in several fields of mesoscopic transport owing to its effectiveness. It has been used effectively in molecular electronics [11, 18, 19], spintronics [10, 20] and molecular electronics. Furthermore [21-23], this method has also been applied for finite bias by means of the asymmetrical Green's function method [24]. Our system is described by a Hamiltonian which can be manually created using a tight-binding technique or is a product of a mathematical operation, including DFT.

3.7 Features of the Transport Curve

Before proceeding, it would be important to apply some simple toy models to briefly study a number of significant features that we are likely to encounter in the more complex transport curves of real structures. For this reason, it will be a matter of applying equation (3.44) (the Green's function) to determine the transmission coefficient by use of equation (3.46) and subsequently the transmission probability. The three aspeexamples will be studied to illustrate the appearance of anti-resonances due to

quantum interference[28, 29], Fano Resonances[26, 27] and Breit-Wigner Resonances [25].

3.7.1 Breit-Wigner Resonance

Of all the aspects, the Breit-Wigner resonance is the simplest to understand. It refers to the peak of Lorentzian in the transmission amplitude which takes place when an energy level in the scatterer resonates with the energy of the incoming wave. Figure 3.7.1 demonstrates an effective instance of this process. Connected to a scattering surface with one ε_1 (site energy) using $-\alpha$ (hopping components) are two one-dimensional semi-infinite crystal-like chains having ε_0 (site energies) and $-\gamma$ (hopping components) as shown:

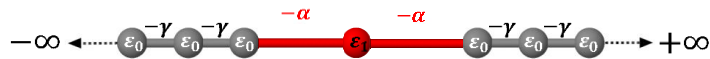


Figure 3.7.1: Simple model to study Fano resonance. Two one-dimensional semi-infinite crystalline chains coupled to a scattering region of site energy ε_1 by hopping elements $-\alpha$.

The transmission probability for this structure when $\alpha = 0.01$, $\gamma = 0.1$ and $\varepsilon_0 = \varepsilon_1 = 0$ is represented by the red line in figure 3.9. The coupling element α defines the breadth of the resonance, while its site is defined by the site energy ε_1 . Usually, the scatterer possess numerous energy levels, but they can easily be identified in an adequately weakly connected system. Resonances related to the LUMO and HOMO levels of the scheme are very evident since the Fermi Energy, and hence the scatterer conductance, is typically between both peaks. On the whole, the conductance is larger and the resonances are wider when the coupling component ($-\alpha$) is big.

3.7.2 Fano Resonance

This is a form of resonant scattering that takes place between two scattering amplitudes, one as a result of the resonant process (an excitation of a distinct state) interference and the other as a result of the background process (scattering in a range of states) [30]. For instance, a particle having a side group gives out a Fano resonance if the energy (E) of the incoming electron is nearby the side group energy level. Figure 3.7 illustrates a toy-model estimation. Two one-dimensional semi-infinite crystal-like systems having hopping components ($-\gamma$) and site energies (ε_0) are connected to a scattering surface with two site energies (ε_1 and ε_2). Site one (ε_1) connects to the leads with hopping components ($-\alpha$), while the side-group, site two (ε_2) is connected to site one by hopping component ($-\beta$).

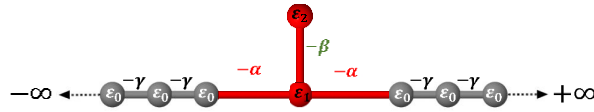


Figure 3.4.7: Simple model to study Fano resonances. Two one-dimensional semi-infinite crystalline chains coupled to a scattering region of site energy (ε_1) by hopping elements ($-\alpha$). An extra energy level (ε_2) is coupled to the scattering level by hopping element ($-\beta$).

This system's transmission probability during $\alpha = \beta = 0.01$, $\gamma = 0.1$ and $\varepsilon_1 = 0$, $\varepsilon_2 = 0.5$ is given in the blue curve in figure (3.7.4). With the exception of the fact that a Fano resonance happens at $E \approx \varepsilon_2$, the nature of the curve is very similar to the Breit-Wigner curve (see Figure 3.9, red). Fano resonances is obviously flexible through the gate voltages [31] or molecular side groups [27] and have been demonstrated to present the molecules fascinating thermoelectric characteristics [11, 32].

3.7.3 Anti-Resonance

An anti-resonance also appears in the transmission probability when the system is multibranch and destructive interference occurs between propagating waves at the nodal point. A simple example is shown in figure (3.7.3). Two one-dimensional semi-infinite crystalline chains with site energies (ε_0) and hopping elements ($-\gamma$) are coupled to two non-interacting scattering regions with site energies ε_1 (site one) and ε_2 (site two) by the hopping parameter ($-\alpha$).

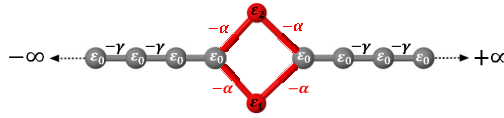


Figure 3.7.3: Simple model to study antiresonances. Two one-dimensional semi-infinite crystalline chains coupled to two independent scattering regions of site energies ε_1 and ε_2 , by hopping elements ($-\alpha$).

The green curve in figure (3.7.4) shows the analytical transmission probability for this system when $\varepsilon_0 = 0$, $\varepsilon_1 = -0.5$, $\varepsilon_2 = -0.5$, $\gamma = 0.1$ and $\alpha = 0.1$. The curve shows two Breit-Wigner peaks at $E = 0$ and $E = 0.5$, which correspond to the site energies of each scatterer as expected. The antiresonance occurs between these points, $E = 0.25$, where the transmission probability drops to $T(E) \approx 0$. This drastic change in electron transmission is utilised in quantum interference effect transistors (QuIET) [33], data storage [34] and molecular switches [35].

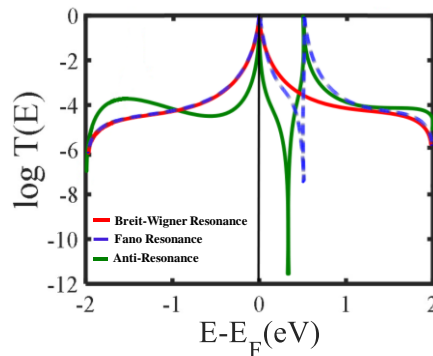


Figure 3.7.4: Transmission coefficients for the systems describe in sections 3.7.1 (Red 3.7.2 (Blue) and 3.7.3 (Green).

3.8 Scissors corrections

Although DFT has been successful in predicting the trends, generally, it is not accurate in predicting the Fermi energy E_F position and the position of the HOMO and LUMO. For that reason, we need to do some corrections to DFT results. The starting point is to calculate ionization potential (IP) and electron affinity (EA) of gas phase molecule. This leads to the more accurate calculation of HOMO (the negative of the IP also called Koopmans theorem) and LUMO (the negative of the EA). The IP and EA are evaluated using the following formulas [40]:

$$\text{IP} = E(N-1) - E(N) \quad (3.74)$$

$$\text{EA} = E(N) - E(N+1) \quad (3.74)$$

Where $E(N)$ is the ground state energy of the neutral molecule, N is the total number of electrons in the molecule. $E(N-1)$ is the energy with one electron removed and $E(N+1)$ is the energy with one electron added. The HOMO-LUMO gap (IP-EA) usually is larger than H-L gap calculated from Kohn-Sham eigenenergies. This can be used to correct position of HOMO and LUMO.

References

- [1] Landauer, R., Spatial variation of currents and fields due to localized scatterers in metallic conduction. IBM Journal of Research and Development, 1957. 1(3): p. 223-231.
- [2] Büttiker, M., et al., Generalized many-channel conductance formula with application to small rings. Physical Review B, 1985. 31(10): p. 6207.
- [3] Datta, S., Electronic transport in mesoscopic systems1997: Cambridge university press.
- [4] Brouwer, P., Scattering approach to parametric pumping. Physical Review B, 1998. 58(16): p. R10135-R10138.
- [5] Finch, C.M., AN UNDERSTANDING OF THE ELECTRICAL CHARACTERISTICS OF ORGANIC MOLECULAR DEVICES, in Physics Department2008, Lancaster University.
- [6] Economou, E.N., Green's functions in quantum physics1984: Springer.
- [7] Mello, P.A. and N.K. Kumar, Quantum transport in mesoscopic systems: complexity and statistical fluctuations: a maximum-entropy viewpoint. Vol. 4. 2004: Oxford University Press on Demand.
- [8] Fisher, D.S. and P.A. Lee, Relation between conductivity and transmission matrix. Physical Review B, 1981. 23(12): p. 6851-6854.
- [9] Visontai, D., Quantum and Classical Dynamics of Molecule Size Systems, in Physics Department2013, Lancaster University.
- [10] Sanvito, S., Giant Magnetoresistance and Quantum Transport in Magnetic Hybrid Nanostructures, in Physics Department2008, Lancaster University.
- [11] Finch, C.M., An understanding of electrical characteristics of organic molecular devices, in Physics Department2008, Lancaster University.

- [12] Aoki, H., Real-space renormalisation-group theory for Anderson localisation: Decimation method for electron systems. *Journal of Physics C: Solid State Physics*, 1980. 13(18): p. 3369.
- [13] Lema, F. and C. Wiecko, Multifractality of the Anderson and binary alloy localized eigenstates by the improved decimation method. *Physica Scripta*, 1993. 47(2): p. 129.
- [14] Leadbeater, M. and C.J. Lambert, A decimation method for studying transport properties of disordered systems. *Annalen der physik*, 1998. 7(5-6): p. 498-502.
- [15] MacKinnon, J.G. and H. White, Some heteroskedasticity-consistent covariance matrix estimators with improved finite sample properties. *Journal of Econometrics*, 1985. 29(3): p. 305-325.
- [16] Ryndyk, D., et al., Green function techniques in the treatment of quantum transport at the molecular scale, in *Energy Transfer Dynamics in Biomaterial Systems2009*, Springer. p. 213-335.
- [17] Lambert, C., V. Hui, and S. Robinson, Multi-probe conductance formulae for mesoscopic superconductors. *Journal of Physics: Condensed Matter*, 1993. 5(25): p. 4187.
- [18] Finch, C.M., et al., Conformation dependence of molecular conductance: chemistry versus geometry. *Journal of Physics: Condensed Matter*, 2008. 20(2): p. 022203.
- [19] I.M. Grace, S.W.B., C. J. Lambert, and J. H. Jefferson, *Molecular Nanowires and Other Quantum Objects*. NATO ASI Series, 2004: p. pages 13-21.

- [20] Athanopoulos, S., Electronic Properties of Hybrid Carbon Nanotubes, in Physics Department 2005, Lancaster University.
- [21] Leadbeater, M. and C. Lambert, Superconductivity-induced phase-periodic transport in nanoscale structures. *Physical Review B*, 1997. 56(2): p. 826-831.
- [22] Koltai, J., J. Cserti, and C. Lambert, Andreev bound states for a superconducting-ferromagnetic box. *Physical Review B*, 2004. 69(9): p. 092506.
- [23] Polinák, P., et al., Andreev drag effect via magnetic quasiparticle focusing in normal-superconductor nanojunctions. *Physical Review B*, 2006. 74(13): p. 132508.
- [24] Rocha, A.R., et al., Spin and molecular electronics in atomically generated orbital landscapes. *Physical Review B*, 2006. 73(8): p. 085414.
- [25] Breit, G. and E. Wigner, Capture of slow neutrons. *Physical Review*, 1936. 49(7): p. 519.
- [26] Fano, U., Effects of configuration interaction on intensities and phase shifts. *Physical Review*, 1961. 124(6): p. 1866.
- [27] Papadopoulos, T., I. Grace, and C. Lambert, Control of electron transport through Fano resonances in molecular wires. *Physical Review B*, 2006. 74(19): p. 193306.
- [28] Ke, S.-H., W. Yang, and H.U. Baranger, Quantum-interference-controlled molecular electronics. *Nano letters*, 2008. 8(10): p. 3257-3261.
- [29] Stadler, R., Quantum interference effects in electron transport through nitrobenzene with pyridil anchor groups. *Physical Review B*, 2009. 80(12): p. 125401.

- [30] Fano, U., Effects of Configuration Interaction on Intensities and Phase Shifts. *Physical Review*, 1961. 124(6): p. 1866-1878.
- [31] Kobayashi, K., et al., Tuning of the Fano effect through a quantum dot in an Aharonov-Bohm interferometer. *Physical Review Letters*, 2002. 88(25): p. 256806.
- [32] Finch, C., V. Garcia-Suarez, and C. Lambert, Giant thermopower and figure of merit in single-molecule devices. *Physical Review B*, 2009. 79(3): p. 033405.
- [33] Stafford, C.A., D.M. Cardamone, and S. Mazumdar, The quantum interference effect transistor. *Nanotechnology*, 2007. 18(42): p. 424014.
- [34] Stadler, R., M. Forshaw, and C. Joachim, Modulation of electron transmission for molecular data storage. *Nanotechnology*, 2003. 14(2): p. 138.
- [35] Baer, R. and D. Neuhauser, Phase coherent electronics: a molecular switch based on quantum interference. *Journal of the American Chemical Society*, 2002. 124(16): p. 4200-4201.
- [36] Paxton, A. T.; others. An Introduction to the Tight Binding Approximation--Implementation by Diagonalisation. *NIC Ser.* 2009, 42, 145–176.
- [37] S Datta. *Electronic Transport in Mesoscopic Systems*. Cambridge University Press, Cambridge, (1995).
- [38] E.N. Economou. *Green's Functions in Quantum Physics*. Springer Verlag, (1983).
- [39] Pier A. Mello and Narendra Kumar. *Quantum Transport in Mesoscopic Systems*. Oxford University Press (2004).
- [40] Alcácer, L. (2018). *Electronic Structure of Organic Semiconductors*. Morgan & Claypool Publishers.

Chapter 4

Anti-resonance features of destructive quantum interference in single-molecule thiophene junctions achieved by electrochemical gating

The results presented in this chapter were published in: Bai, Jie, et al., “Anti-resonance features of destructive quantum interference in single-molecule thiophene junctions achieved by electrochemical gating.” *Nature Materials*, 2019, 18.4: 364.

This study is a collaborative work, in which the experiments were carried out in Xiamen University, China.

4.1 Introduction

In the past two decades, the study of the electrochemical gating of molecular devices has triggered a growing interest because of the possibilities to scale electrical components down to the nanoscale level [1]. Controlling charge transport through a single molecule connected to metallic electrodes remains one of the most fundamental challenges of nanoelectronics. Previously, a conductance switching in molecular junctions using various means has been demonstrated, including bias pulses [2], electrostatic gating [3], and electrochemical gating [4].

In electrochemically active molecular system, such as viologens [5], oligoaniline[6], ferrocene [7], transition metal complexes [8], perylenebisimides [9], redox-active proteins [10], quinones [11] and tetrathiafulvalene [12], as well as redox-inactive molecules [13], the concept of “electrochemical gating” can be employed to overcome the technical challenges of incorporating a gate electrode in molecular devices. For example, by applying a range of electrochemical potentials, the conductance of 6pTTF6

was measured over the two redox transitions [1,31]. Also, enhanced off resonance tunneling currents were observed for the totally reduced or totally oxidized redox complex [32].

Electrochemical gating has been proven to be an effective approach to manipulate charge transport in molecular junctions and has been successfully developed in the electrochemically active- and inert molecule systems [24-29]. On the one hand, the applied electrode potentials can be used to tune the molecular conductance by controlling the redox processes in the vicinity of the equilibrium potentials of the molecular junctions. This continuous control of conductance with an changing distance between backbone and ionic liquid is an ideal strategy for realizing a single-molecule transistor, and has been denoted “electrolyte gating” in some papers [27,31]. However, apart from those passing through resonant transport during electrochemical gating, the molecular conductance changes very little with the changing potentials, in agreement with the predicted changes in electron transmission [30,31].

Destructive quantum interference (DQI) in single molecular junctions describes a quantum effect in which the electron waves propagate through separated molecular orbitals and combine destructively, leading to a reduction in the electron transmission probability and a suppression in molecular conductance [14-16] by orders of magnitude compared with very similar molecular junctions without DQI [14,17]. Consequently, control of DQI effects in single-molecule junctions provides a novel strategy for developing high-performance molecular devices, such as molecular switches [18,19], transistors [20-22] and thermoelectric devices [23]. In what follows, my aim is to demonstrate that electrochemical gating can be utilized for the fine-tuning of charge transport properties in single-molecule thiophene junctions with and without DQI.

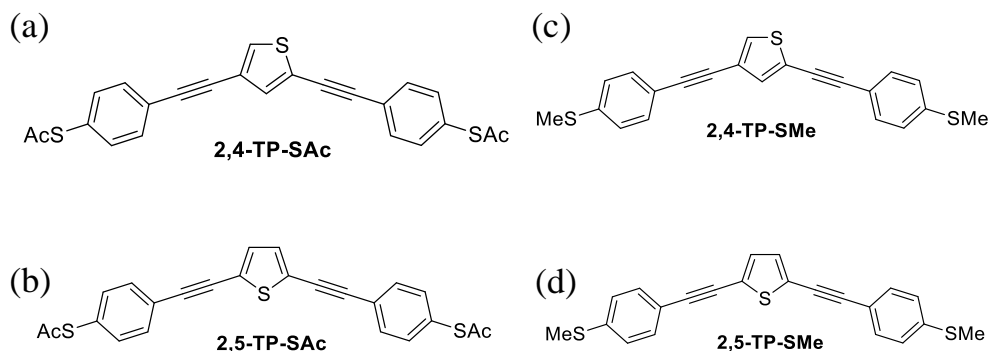


Figure 4.1.1. Molecular structures of thiophene junctions. **a,b)** Molecular structures of thiophene with anchoring groups of thioacetyl ($-SAc$) **c,d)** Molecular structures of thiophene with the anchoring group thiomethyl ($-SMe$).

Figure 4.1.1 Shows molecular structures of thiophene junctions with anchoring groups of thioacetyl (a,b) with different connectivity (2,4-TP-SAc) and (2,5-TP-SAc) and with the thiomethyl anchoring group (c,d) with different connectivity (2, 4-TP-SMe) and (2, 5-TP-SMe) to electrodes.

4.2 Results and Discussion

After finding the relax ground state geometry of (2,4-TP-SAc), (2,5-TP-SAc), (2, 4-TP-SMe) and (2, 5-TP-SMe), next stage is connecting the junctions to two gold electrodes as shown in figure 4.2.1, to calculate the optimum binding distance for a $1-Sp$ molecule between two gold (111) surfaces we used the SIESTA implementation of DFT and the counterpoise method, which removes basis set superposition errors (BSSE). The binding distance z is defined as the distance between the gold surface and the molecule ($1-Sp$) at the closest point. $1-Sp$ is defined as monomer A and the gold electrodes as monomer B.

The ground state energy of the total system is calculated using SIESTA, where is denoted E_{AB}^{AB} , with the parameters defined as those in the “Theory and Simulation”

section of the main text. The gold leads consist of 7 layers each containing 12 atoms. The energy of each monomer is then calculated in a fixed basis, which is achieved by the use of ghost atoms in SIESTA. Hence the energy of the individual molecule **1-Sp** in the presence of the fixed basis is defined as E_A^{AB} and for the gold is E_B^{AB} . The binding energy is then calculated using the following equation:

$$\text{Binding Energy} = E_{AB}^{AB} - E_A^{AB} - E_B^{AB} \tag{4.1}$$

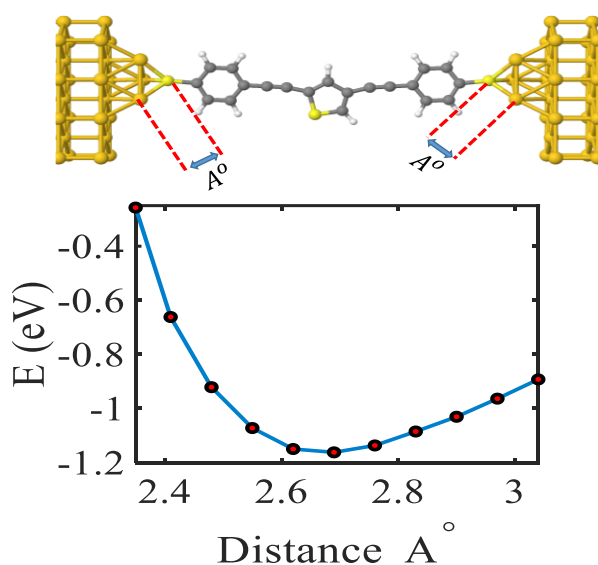


Figure 4.2.1. Binding energies as a function of the distance (Å) of the sulfur from the electrode surface (lower). Examples of binding geometries on a Tip electrode and an electrode containing and atom (above).

The optimized geometry and ground state Hamiltonian and overlap matrix elements of each structure (as shown in Figure 4.2.2.) was self-consistently obtained using the SIESTA [28] implementation of density functional theory (DFT). SIESTA employs norm-conserving pseudo-potentials to account for the core electrons and linear combinations of atomic orbitals to construct the valence states. The generalized gradient approximation (GGA) of the exchange and correlation functional is used with the Perdew-Burke-Ernzerhof parameterization (PBE) a double- ζ polarized (DZP) basis set, a real-space grid

defined with an equivalent energy cut-off of 250 Ry. The geometry optimization for each structure is performed to the forces smaller than 10 meV/Å.

The mean-field Hamiltonian obtained from the converged DFT calculation was combined with Gollum² implementation of the non-equilibrium Green's function method [3] to calculate the phase-coherent, elastic scattering properties of the each system consist of left gold (source) and right gold (drain) leads and the scattering region. The transmission coefficient $T(E)$ for electrons of energy E (passing from the source to the drain) is calculated via the relation: $T(E) = \text{Trace}(\Gamma_R(E)G^R(E)\Gamma_L(E)G^{R\dagger}(E))$. In this expression, $\Gamma_{L,R}(E) = i(\Sigma_{L,R}(E) - \Sigma_{L,R}^\dagger(E))$ describe the level broadening due to the coupling between left (L) and right (R) electrodes and the central scattering region, $\Sigma_{L,R}(E)$ are the retarded self-energies associated with this coupling and $G^R = (ES - H - \Sigma_L - \Sigma_R)^{-1}$ is the retarded Green's function, where H is the Hamiltonian and S is overlap matrix. Using obtained transmission coefficient $T(E)$, the conductance could be calculated by Landauer formula ($G = G_0 \int dE T(E)(-\partial f/\partial E)$) where $G_0 = 2e^2/h$ is conductance quantum.

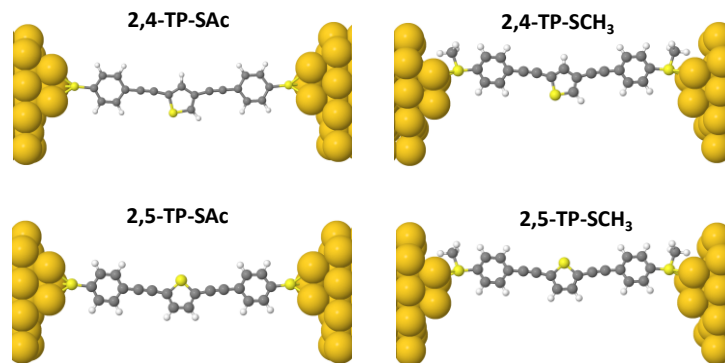


Figure 4.2.2. *Molecular junctions connected to the gold electrodes from 2,4 and 2,5 connectivity's with sulfur acetyl and with sulfur methyl anchor groups.*

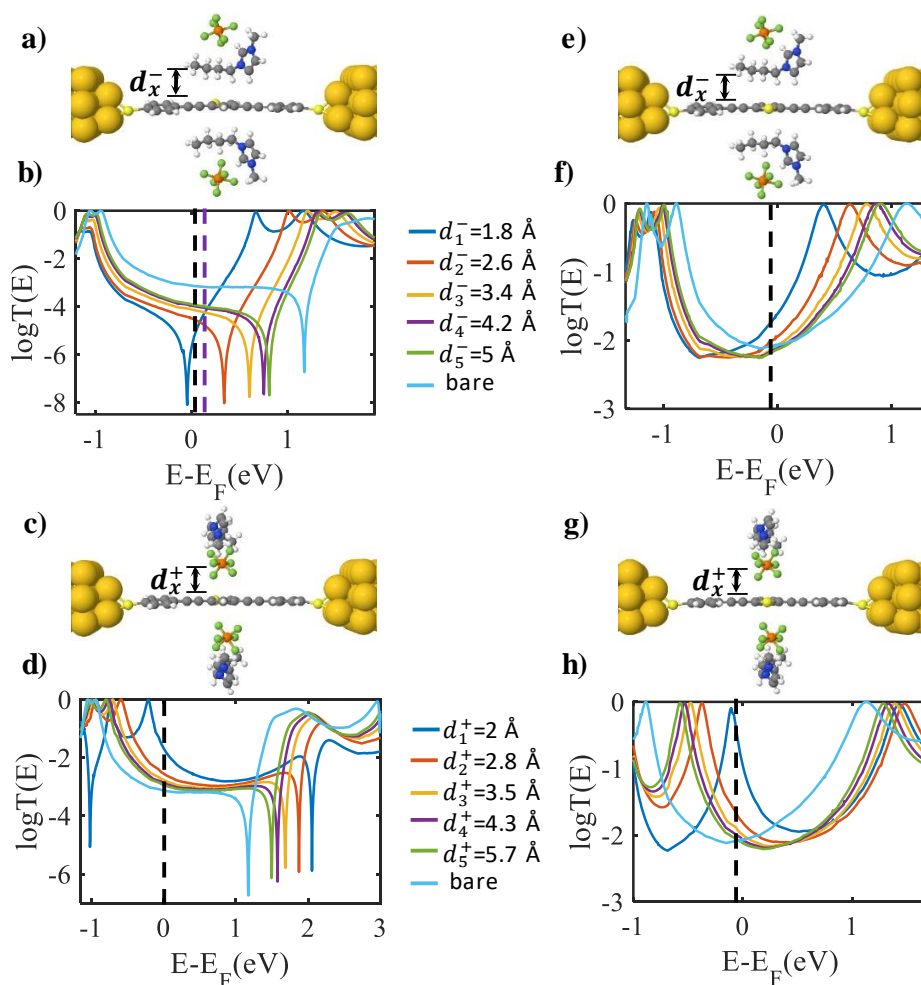


Figure 4.2.3. Transport properties of thiophene core (TP) molecular junctions in the absence and presence of HIMPF6. **a,b)** structure of 2,4-TP-SAc molecular junctions and corresponding transmission coefficient in presence of negative charge potential. **c,d)** structure of 2,4-TP-SAc molecular junctions and corresponding transmission coefficient in presence of positive charge. **e,f)** structure of 2,5-TP-SAc molecular junctions and corresponding transmission coefficient in presence of negative charge potential. **g,h)** structure of 2,5-TP-SAc molecular junctions and corresponding transmission coefficient in presence of positive charge potential.

Due to electrochemical gating, the concentration of charge double layer formed by positively charged 1-hexyl-3-methylimidazolium (HIM) and negatively charged hexafluorophosphate (PF6) varies around the molecular backbone. This changes the applied electric field to the backbone. In order to understand the effect of the electric field on the backbone, I perform quantum transport calculation [14] of the junctions formed by thiophene core (TP) connected to the gold electrodes from 2,4 and 2,5 connectivities with thiol and SMe anchors (Figure 4.2.2.) in the absence and presence of

HIMPF₆. Depending on the electrodes potential, either positive or negative sides of HIMPF₆ placed toward the backbone. I account the variation in the effective electric field by moving HIMPF₆ with certain orientation toward the backbone. Figure 4.5 shows **2,4-TP-SAc** and **2,5-TP-SAc** molecular junctions in the presence of HIMPF₆ with two different orientations where positive (Figure 4.2.3a,e) or negative (Figure 4.2.3c,g) side of HIMPF₆ is closer to the backbone. I calculate material specific mean field Hamiltonian [14] of each structure and combine with transport code Gollum [29] to calculate transmission coefficient T(E) of electron with energy E passing form one electrode to the other. And calculate electrical conductance G from transmission coefficient $G=G_0T(E_F)$ where G_0 is conductance quantum and E_F is the Fermi energy of electrodes, as shown in Figure 4.2.4 where shows conductance carves of (2,4-2-5)TP-SAc in the presence of negative and positive charges at different positions.

The transmission coefficient of bare junction (in the absence of HIMPF₆) shows destructive quantum interference (DQI) for **2,4-TP-SAc** as shown in (Figure 4.2.3 b,d,),whereas QI is constructive in **2,5-TP-SAc** (Figure 4.2.3f,h). When an electric field applied depending on the orientation of HIMPF₆ the transmission coefficient shifts to the left or right. d_x^\pm in Figure 4.2.3 denotes the position (x) of HIMPF₆ from the backbone and its orientation (\pm). When HIM gets closer to back bone (d_x^- in Figure 4.2.3), T(E) shifts to the left whereas it shifts to the right when PF₆ gets closer to back bone (d_x^+ in Figure 4.2.3). Note that HOMO-LUMO gap also shrinks by electric field. In addition, the dip due to destructive QI in 2,4-TP-SAc moves by the position of HIMPF₆. Clearly, if the Fermi energy lies close to the dip of T(E) in **2,4-TP-SAc** a large variation of the conductance is predicted (Figure 4.2.3b,d). Conversely, when HIMPF₆ get closer to the backbone form PF₆ side, the dip of T(E) move to the right away from

the DFT predicted Fermi energy (black dashed line) and therefore the variation is smaller (Figure 4.2.3d). In **2,5-TP-SAc** with a constructive QI (Figure 4.2.3f,h), $T(E)$ does not have a dip and therefore a smaller variation is predicted unless the Fermi energy happens to be in the tail of resonances. Note that if Fermi energy of the electrodes in the absence of electric field lies around the middle of HOMO-LUMO gap of bare junction (e.g. $E=0.1\text{eV}$) shown by black dashed line in Figure 4.2.3b, the conductance initially decreases with negative field (Figure 4.2.3a,b) from d_1^- to d_2^- but then increases from d_2^- to bare. This trend is in agreement with measurement of Figure 4.2.7 and demonstrates the gating of destructive QI in 2,4-TP-SAc.

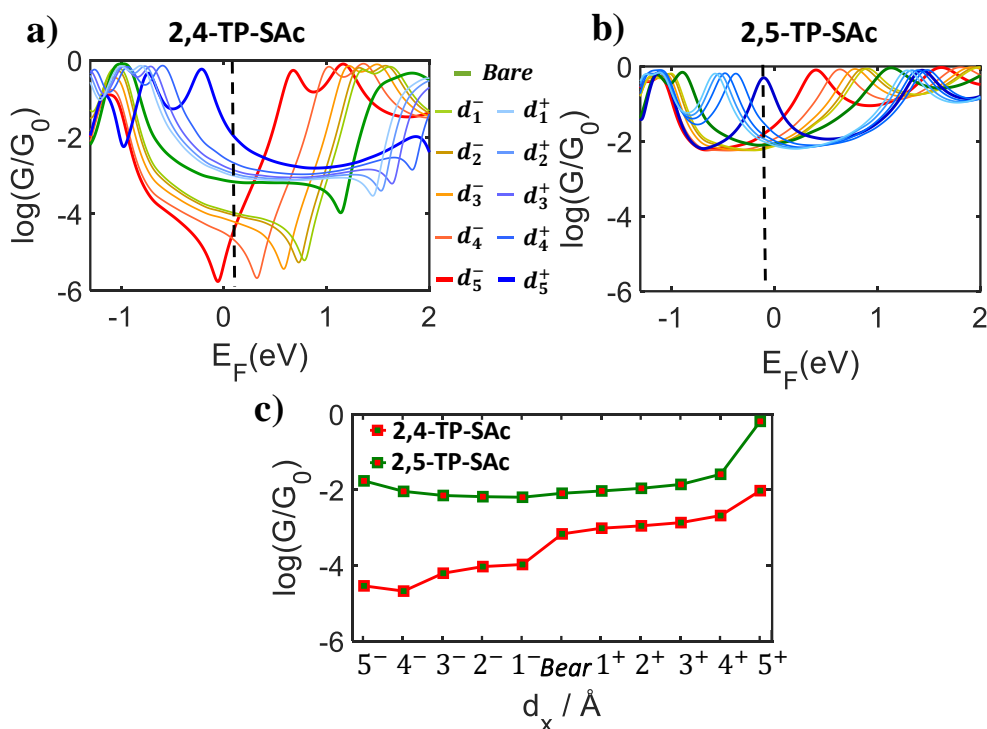


Figure 4.2.4. **a)** Conductance curves of **2,4-TP-SAc** in the presence of negative and positive charges at different positions. **b)** Conductance curves of **2,5-TP-SAc** in the presence of negative and positive charges at different positions. **c)** Comparison of **2,4-TP-SAc** and **2,5-TP-SAc** conductance versus position of HMIPF₆.

Figure 4.2.4. Shows the variation of the conductance versus position of HIMPf₆ from the back bone for both **2,4-TP-Sac** and **2,5-TP-SAc** at the DFT predicted Fermi energy, The Fermi energy (black dashed lines) lies around the middle of the highest occupied

molecular orbital and lowest unoccupied molecular orbital (HOMO–LUMO) gap ($E_F = 0.1$ eV) of the bare junction for 2,4-TP- SAc and at -0.08 eV for 2,5-TP- SAc. This is in a good agreement with measurement at figure 4.2.7.

The following results show molecular junctions corresponding quantum transport calculation of the junctions formed by thiophene core (TP) connected to the gold electrodes from 2,4 and 2,5 connectivities with SME anchors (**Figure 4.2.5**)

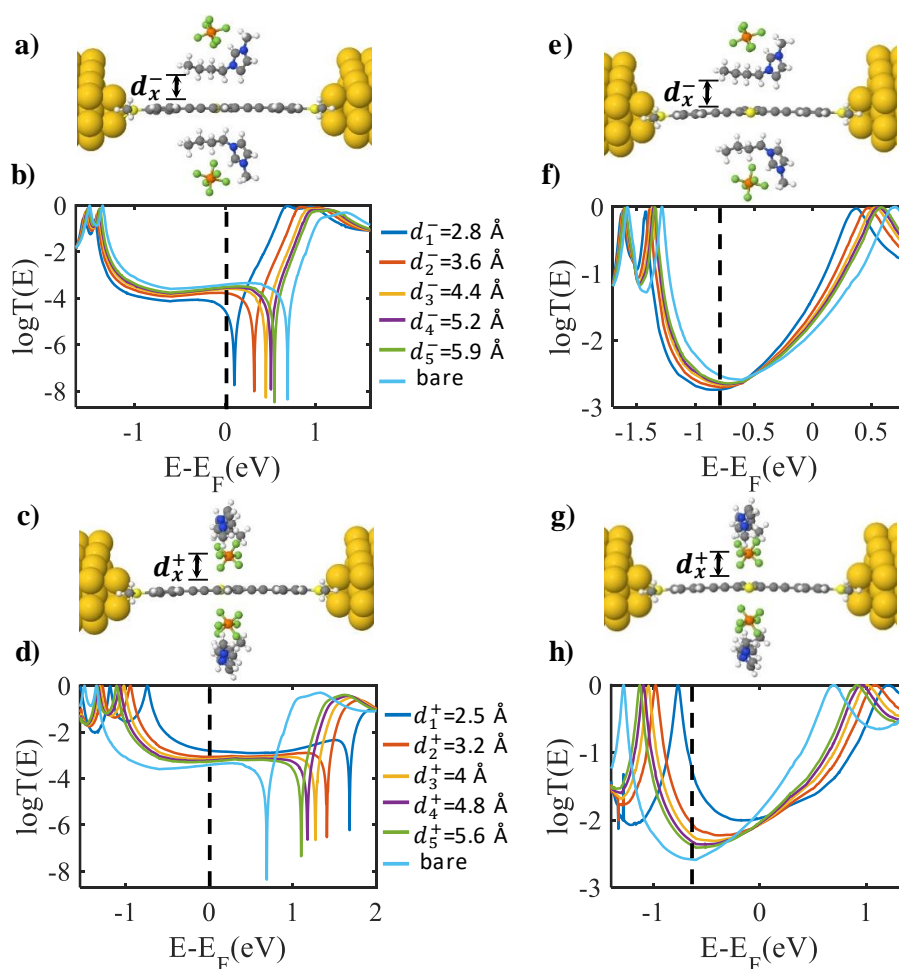


Figure 4.2.5. Transport properties of thiophene core (TP) molecular junctions in the absence and presence of HIMPf6. **a,b**) structure of 2,4-TP-SMe molecular junctions and corresponding transmission coefficient in presence of negative charge potential. **c,d**) structure of 2,4-TP-SMe molecular junctions and corresponding transmission coefficient in presence of positive charge. **e,f**) structure of 2,5-TP-SMe molecular junctions and corresponding transmission coefficient in presence of negative charge potential. **g,h**) structure of 2,5-TP-SMe molecular junctions and corresponding transmission coefficient in presence of positive charge potential.

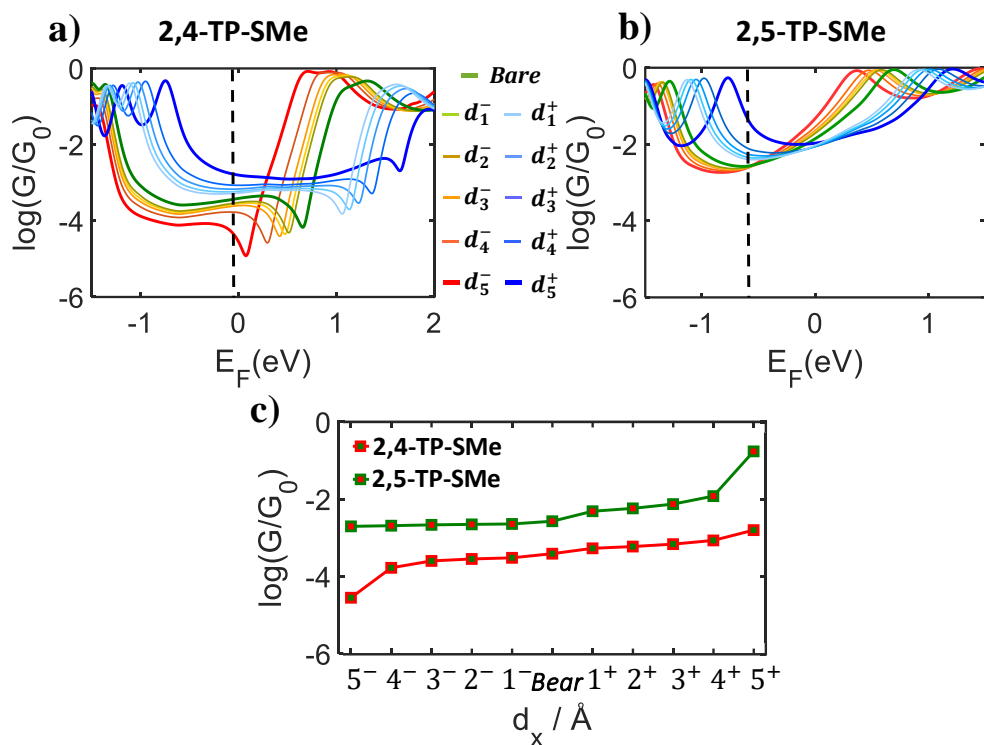


Figure 4.2.6. **a)** Conductance curves of 2,4-TP-SMe in the presence of negative and positive charges at different positions. **b)** Conductance curves of 2,5-TP-SMe in the presence of negative and positive charges at different positions. **c)** Comparison of 2,4-TP-SMe and 2,5-TP-SMe conductance versus position of HMIPF6.

Figure 4.2.5 and figure 4.2.6 show transport and conductance properties of 2,4-TP-SMe and 2,5-TP-SMe molecular junctions in the absence and presence of HMIPF6. The Fermi energy (black dashed lines) lies around the middle of the highest occupied molecular orbital and lowest unoccupied molecular orbital (HOMO–LUMO) gap ($E_F = -0.08$ eV) of the bare junction for 2,4-TP-SMe and at -0.6 eV for 2,5-TP-SMe. the conductance behavior in ASc anchor However, the conductance variation is higher with thiol anchor (Figure 4.2.4) compared to SMe (Figure 4.2.6).

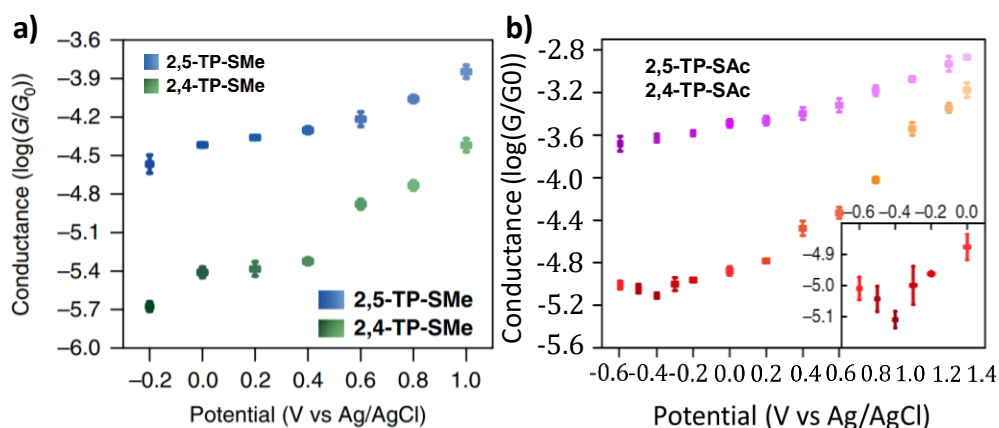


Figure 4.2.7. **a)** Tendency of the molecular conductance of **2,5-TP-SAc** (purple) and **2,4-TP-SAc** (orange) versus electrode potentials from -0.6 V to 1.3 V. Inset, magnification from -0.6 V to 0 V. **b)** Tendency of the molecular conductances of **2,4-TP-SMe** and **2,5-TP-SMe** versus electrode potentials from -0.2 to 1.0 V.

Next I compare my results with the electrochemical gating experiments performed by my collaborators at Xiamen University. Electrochemical gating experiments are performed by a four-electrode bipotentiostat setup, where both the coated Au tip and Au bead serve as the working electrodes. The potential of the working electrodes were controlled separately with respect to the reference electrode upon the bipotentiostat setup. The potential difference between the two working electrodes is the bias voltage applied to the molecular junctions. In electrochemical gating measurements, the electrode potentials of coated Au tip and Au bead were tuned simultaneously relative to the Ag/AgCl quasireference electrode, and the potential of coated Au tip is 0.1 V higher than that of Au bead all along. In all the experiments, the potentials of coated Au tip relative to the Ag/AgCl were adopted as the applied potentials. The break-junction measurement of ECTB chips was made in a modified mechanically controllable break junction (MCBJ) setup modified by my collaborator.

Figure 4.2.7ashows the measured electrical conductance of **2,5-TP-SAc** (purple) and **2,4-TP-SAc** (orange) versus electrode potentials from -0.6 V to 1.3 V. Also Figure

4.2.7b shows measured electrical conductance of 2,4-TP-SMe and 2,5-TP-SMe versus electrode potentials from -0.2 to 1.0 V. These results are in a very good agreement with the calculated electrical conductance in Figures 4.2.4c and 4.2.6c.

In summary, the molecular conductance was increased by reducing the distance between the negative side of an ionic liquid and the molecular backbone, On the other hand the molecular conductance was decreased by reducing the distance between the thiophene molecule and the positive side of the ionic liquid. This work provides evidence of the tuning of charge transport and DQI of thiophene molecule at room temperature.

References

- [1] Kay, N. J., Higgins, S. J., Jeppesen, J. O., Leary, E., Lycoops, J., Ulstrup, J., & Nichols, R. J. (2012). Single-molecule electrochemical gating in ionic liquids. *Journal of the American Chemical Society*, 134(40), 16817-16826.
- [2] Baghernejad, M., Zhao, X., Baruël Ørnsø, K., Füeg, M., Moreno-García, P., Rudnev, A. V., ... & Broekmann, P. (2014). Electrochemical control of single-molecule conductance by Fermi-level tuning and conjugation switching. *Journal of the American Chemical Society*, 136(52), 17922-17925..
- [3] Garner, M. H. et al. Comprehensive suppression of single-molecule conductance using destructive σ -interference. *Nature* 558, 415-419.
- [4] Arroyo, C. R. et al. Signatures of quantum interference effects on charge transport through a single benzene ring. *Angew Chem Int Ed Engl* 52, 3152-3155.
- [5] Baer, R. & Neuhauser, D. Phase Coherent Electronics: A Molecular Switch Based on Quantum Interference. *Journal of the American Chemical Society* 124, 4200-4201.
- [6] Solomon, G. C. et al. Quantum Interference in Acyclic Systems: Conductance of Cross-Conjugated Molecules. *J. Am. Chem. Soc.* 130, 17301-17308.
- [7] Ke, S.-H., Yang, W. & Baranger, H. U. Quantum-Interference-Controlled Molecular Electronics. *Nano Letters* 8, 3257-3261.
- [8] Saha, K. K., Nikolić, B. K., Meunier, V., Lu, W. & Bernholc, J. Quantum-Interference-Controlled Three-Terminal Molecular Transistors Based on a

- Single Ring-Shaped Molecule Connected to Graphene Nanoribbon Electrodes. Physical Review Letters 105, 236803.
- [9] Hsu, L. Y. & Rabitz, H. Single-molecule phenyl-acetylene-macrocycle-based optoelectronic switch functioning as a quantum-interference-effect transistor. Phys Rev Lett 109, 186801.
- [10] Bergfield, J. P., Solomon, G. C., Stafford, C. A. & Ratner, M. A. Novel Quantum Interference Effects in Transport through Molecular Radicals. Nano Lett. 11, 2759-2764.
- [19] Zhang, J. D. et al. Single-molecule electron transfer in electrochemical environments. Chem. Rev. 108, 2737-2791, (2008).
- [20] Huang, C., Rudnev, A. V., Hong, W. & Wandlowski, T. Break junction under electrochemical gating: testbed for single-molecule electronics. Chem Soc Rev 44, 889-901.
- [21] Nichols, R. J. & Higgins, S. J. Single Molecule Nanoelectrochemistry in Electrical Junctions. Acc Chem Res 49, 2640-2648.
- [22] Capozzi, B. et al. Tunable charge transport in single-molecule junctions via electrolytic gating. Nano Lett 14, 1400-1404.
- [23] Xiang, L. et al. Gate-controlled conductance switching in DNA. Nat Commun 8, 14471.
- [24] Brooke, R. J. et al. Dual Control of Molecular Conductance through pH and Potential in Single-Molecule Devices. Nano Lett 18, 1317-1322.
- [25] Baghernejad, M. et al. Highly-effective gating of single-molecule junctions: an electrochemical approach. Chem Commun (Camb) 50, 15975-15978.

- [26] Brooke, R. J. et al. Single-molecule electrochemical transistor utilizing a nickel-pyridyl spinterface. *Nano Lett* 15, 275-280.
- [27] Capozzi, B. et al. Mapping the Transmission Functions of Single-Molecule Junctions. *Nano Lett* 16, 3949-3954.
- [28] Soler, J. M. et al. The SIESTA method for ab initio order- N materials simulation.
- [29] Ferrer, Jaime, et al. "GOLLUM: a next-generation simulation tool for electron, thermal and spin transport." *New Journal of Physics* 16.9 (2014): 093029.
- [30] Song, H., Kim, Y., Jeong, H., Reed, M. A., & Lee, T. (2010). Coherent tunneling transport in molecular junctions. *The Journal of Physical Chemistry C*, 114(48), 20431-20435.
- [31] Vezzoli, A., Grace, I., Brooke, C., Wang, K., Lambert, C. J., Xu, B., ... & Higgins, S. J. (2015). Gating of single molecule junction conductance by charge transfer complex formation. *Nanoscale*, 7(45), 18949-18955.
- [32] Herrera, S., Adam, C., Ricci, A., & Calvo, E. J. (2016). Electrochemical gating of single osmium molecules tethered to Au surfaces. *Journal of Solid State Electrochemistry*, 20(4), 957-967.

Chapter 5

Quantum transport across graphene nanogaps bridged by carbon atomic chains

5.1 Introduction

Since its first discovery in 2004 graphene has been set as one of the most promising materials for generating new technological applications. This exciting material gives exceptional electrical properties [1,2], optical [3,4], mechanical [5,6], and thermal properties [7,8]. The high thermal conductivity of graphene makes this material very attractive to manage heat and dissipate it in high-density devices, which is a serious problem in modern nanoelectronics.

Carbon exhibits an exceptionally rich variety of allotropes, including fullerenes [9], carbon nanotubes [10,11] two-dimensional graphene and three-dimensional diamond and graphite [12,13]. Driven by a desire to develop new wiring strategies for molecular-scale devices, the electrical properties of one-dimensional atomic chains of carbon are of particular interest [14,15], both in their oligoynes form [16-18] (comprising chains of alternating single and triple bonds) and as more highly conducting, cumulenic wires [19-28] (formed from chains of double bonds). Experimental and theoretical studies of atomic and molecular chains have focused mainly on their charge [29-36] and spin [37-42] transport properties, when attached to metallic electrodes by terminal groups such as thiols, amines or pyridines. More recently, it has become possible to create carbon chains and filaments, which are automatically covalently bonded to graphene electrodes, which avoids the need for such terminal groups [43-50]. Such all-carbon molecular-scale junctions are of interest, because they avoid the complexity of metal-molecule interfaces, which can reduce the overall junction conductance and they can be

Chapter 5 *Quantum Transport Across Graphene Nanogaps Bridged By*

electrostatically gated to control the energies of frontier orbitals relative to the Fermi energy of the electrodes. On the other hand, the wide variety of graphene edges that can form in such junctions and the diversity of carbon chains that could bridge the electrodes, means that such junctions possess their own complexities, which must be studied if this nascent technology is to be exploited. Examples of this wide variability are observed in TEM studies of graphene junctions [51, 52], where both even and odd numbered chains of carbon atoms and are observed to be covalently bonded to 5, 6 or 7-membered rings at graphene edges. Here I aim to determine how the electrical conductance of such chains is determined by their length and by the nature of the graphene edges to which they bond. Since such edges can be spin active, I perform calculations of spin dependent transport in the presence of both unsaturated and saturated (hydrogen terminated) graphene edges. Based on our calculations, it is evident that atomic carbon chains coupled to graphene electrodes can exhibit a huge variety of electrical conductance's and can form effective spin-filters with a large spin polarization.

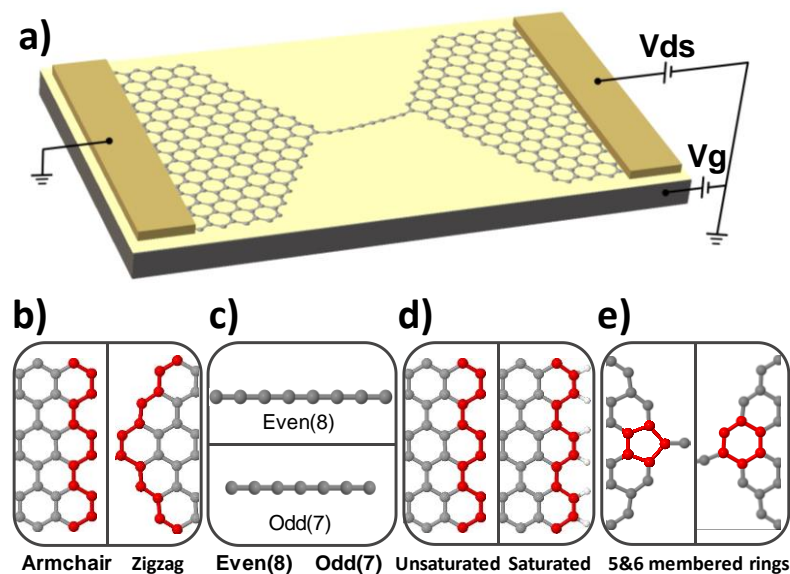


Figure 5.1.1. Structure of graphene junctions. (a) Device structure of graphene junctions bridged by a carbon chain between two electrodes. (b) Armchair and zigzag graphene edges. (c) Examples of atomic chains with even (8) and odd (7) numbers of carbon atoms (d) Unsaturated and saturated graphene edges. (e) 5 and 6 membered rings.

Examples of unsaturated (left) and saturated right edges. In the latter, the rightmost carbon are bonded to hydrogen atoms. (e) 5- (left) and 6- (right) membered terminal rings.

Figure 5.1.1a shows an example of a junction consisting of two graphene electrodes, with zigzag edges in the transport direction connected to a carbon chain through six-membered terminal rings. In practice there are many possible combinations of edges and chains. In what follows, I investigate the series of such junctions shown in Figures 5.1.1b-e, with different edge structures and terminations connected to carbon chains, with odd and even numbers of carbon atoms through different terminal rings. Figure 5.1.1b show examples of armchair (Ar) (left panel) and zigzag (Zi) edges (right panel). Figure 5.1.1c shows examples of atomic chains with even (8) and odd (7) numbers of carbon atoms. As shown in Figure 5.1.1d, the edges of graphene sheet can be unsaturated (U) (left) or saturated (S) by hydrogen atoms (right). Figure 5.1.1e shows examples of a 5-membered terminal ring (left) (5) and a 6-membered terminal ring (right) (6). In what follows I consider junctions in which the two electrodes have the same termination and assign a label ABCD to each junction, where A = Ar or Zi to denote the armchair or zigzag nature of the edges, B = E or O to denote the even or odd number of carbon atoms in the chain, C = U or S to denote unsaturated or saturated edges, and D = 5 or 6 to denote 5- or 6-membered terminal rings

5.2 Results and Discussion

Figures 5.1.2a, b, d, e show examples of such junctions. For example figure 5.1.2a shows an ArEU6 junction, whose two graphene electrodes possess unsaturated armchair edges, connected by six-membered terminal rings to a chain with an even number of carbon atoms.

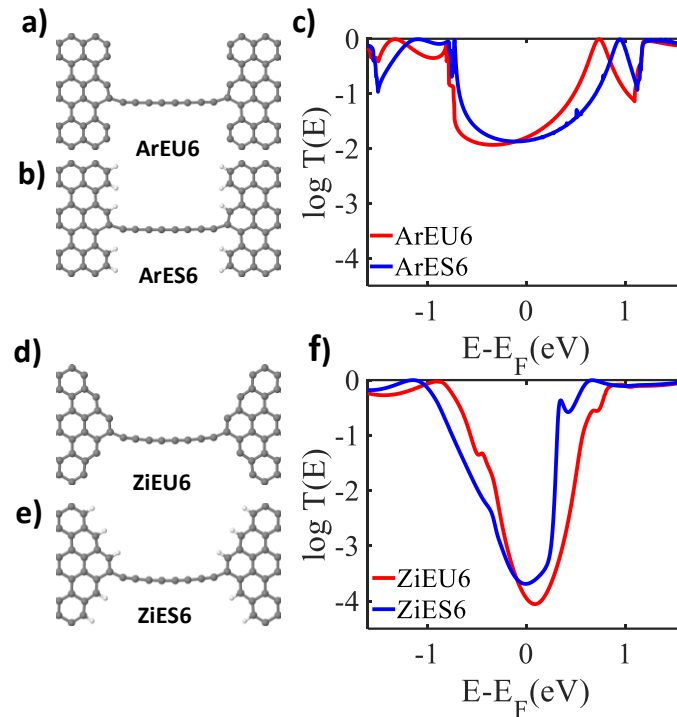


Figure 5.2.1. Electron transport through even-numbered atomic chains connected to graphene electrodes. *a,b*) Relaxed atomic structure of an even (8) numbered carbon chain connected to unsaturated and saturated armchair edges via six membered terminal rings (ArEU6)(ArES6). *d,e*) Relaxed atomic structure of an even (8) numbered carbon chain connected to unsaturated and saturated zigzag edges via six membered terminal rings (ZiEU6) (ZiES6). *(c)* Transmission coefficients versus energy for structures *(a,b)* obtained from DFT. *(f)* Transmission coefficients versus energy for structures *(d,e)*, obtained from DFT.

In order to study the electronic properties of these junctions, I first used density functional theory (DFT) to relax the junctions and obtain their ground state geometries. Next the underlying DFT mean-field Hamiltonian was combined with the quantum transport code Gollum to obtain transmission coefficient $T(E)$ describing electrons with energy E passing from one electrode to the other. Computational Methods. The optimized geometry, ground state Hamiltonian and overlap matrix elements of each structure were obtained self-consistently using the SIESTA[47] implementation of DFT. SIESTA employs norm-conserving pseudopotentials to account for the core electrons and linear combinations of atomic orbitals (LCAO) to construct the valence states. The generalized gradient approximation (GGA) of the exchange and correlation functional is used with the Perdew–Burke–Ernzerhof (PBE) parametrization [48, 49]

Chapter 5 **Quantum Transport Across Graphene Nanogaps Bridged By**

and a double- ζ polarized (DZP) basis set. The real-space grid is defined with an equivalent energy cutoff of 250 Ry. The geometry optimization for each structure is performed to the forces smaller than 10 meV/Å. The mean-field Hamiltonian obtained from the converged SIESTA DFT calculation was combined with the quantum transport code Gollum, [58] to calculate the phase coherent, elastic scattering properties of the each system consisting of left (source) and right (drain) graphene leads. The transmission coefficient $T(E)$ for electrons of energy E (passing from the source to the drain) is calculated via the relation $T(E) = \text{Trace}(\Gamma_R(E)G^R(E)\Gamma_L(E)G^{R\dagger}(E))$. In this expression, $\Gamma_{R,L}(E) = i(\Sigma_{R,L}(E) - \Sigma_{R,L}^\dagger(E))$ describe the level broadening due to the coupling between left (L) and right (R) electrodes and the central scattering region, ($\Sigma_{R,L}(E)$ are the retarded self-energies associated with this coupling and $G^R = (ES - H - \Sigma_L - \Sigma_R)^{-1}$ is the retarded Green's function, where H is the Hamiltonian and S is the overlap matrix. Using obtained transmission coefficient $T(E)$, the conductance could be calculated by Landauer formula $G = G_0 \int dE T(E) (-\partial f(E, T)/\partial E)$ where $G_0 = 2e^2/h$ is the conductance quantum, $f(E) = (1 + \exp((E - E_F)/K_B T))^{-1}$ is the Fermi-Dirac distribution function, T is the temperature, and $K_B = 8.6 \times 10^{-5} eV/K$ is Boltzmann's constant.

To demonstrate the effect of edge saturation, Figure 5.1.2(c) shows the transmission coefficient of ArEU6 (Fig 5.1.2(a)) and ArES6 (Fig 5.1.2(b)) junctions as a function of the energy. It is clear that transmission curves are close to each other and therefore edge saturation has only a modest effect on transport, particularly near the middle of the HOMO and LUMO gap ($E=0$). Figure 5.1.2(f) shows the transmission coefficient of the corresponding zigzag-edge structure ZIEU6 (Fig 5.1.2(d)) and ZIES6 (Fig 5.1.2(e)), and again I find that the transmission curves are rather insensitive to edge saturation.

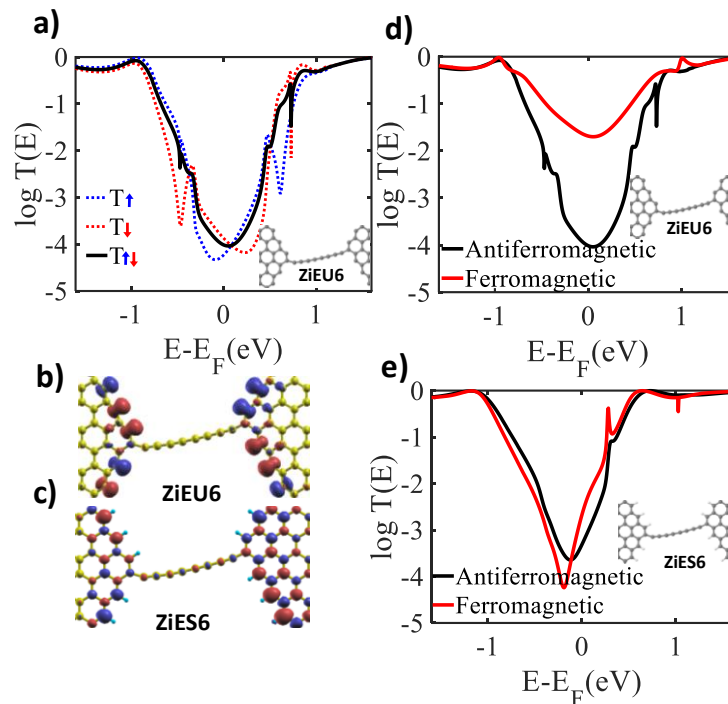


Figure 5.2.2. (a) Transmission coefficients of spin up and spin down electrons for even (8) numbered carbon atoms connected to unsaturated zigzag edges via six membered rings. (b,c) Spin densities ($\rho_{\uparrow} - \rho_{\downarrow}$) of even (8) numbered of carbon chains connected to unsaturated and saturated zigzag edges via six membered terminal rings (ZiEU6)(ZiES6). Blue and red correspond to positive and negative isosurfaces of ($\rho_{\uparrow} - \rho_{\downarrow}$) with antiferromagnetic and ferromagnetic spin order respectively. (d,e) Transmission coefficients with antiferromagnetic and ferromagnetic spin order for even (8) numbered carbon connected to unsaturated and saturated zigzag edges via six membered rings for structures (b,c) respectively.

It is well known that the ground state of the structures with zigzag edges can be antiferromagnetic [53, 54]. To investigate spin transport in these structures, Figure 5.2.2a shows the transmission coefficients of spin up and spin down electrons for ZiEU6. In order to understand the effect of edge saturation, I calculated the spin densities ($\rho_{\uparrow} - \rho_{\downarrow}$) of both ZiEU6 and ZiES6 structures, as shown in figures 5.2.2b and c respectively, where blue and red correspond to positive and negative isosurfaces of ($\rho_{\uparrow} - \rho_{\downarrow}$). Clearly, the spin density is larger near the unsaturated edges of the structure 5.2.2b. Figure 5.2.2d shows Transmission coefficients with antiferromagnetic and ferromagnetic spin order. Clearly the transmission coefficients of these structures are significantly affected by the spin ordering at unsaturated edges. For antiferromagnetic spin calculations, the spin density is initially constructed with the maximum possible

spin polarization for each atom in its atomic configuration. This variable defines the relative orientation of the atomic spins, for example, in ferromagnetic case, spin of electrons on all carbon atoms set to spin up in contrast to antiferromagnetic order where we set the spin-up for the odd atoms and the spin-down for even atoms. The electronic relaxation of molecules then may lead to an antiferromagnetic spin configuration or a ferromagnetic one depend on the molecular structure. My calculations show that spin order has little effect when the edges are saturated, as shown in Figure 5.2.2e.

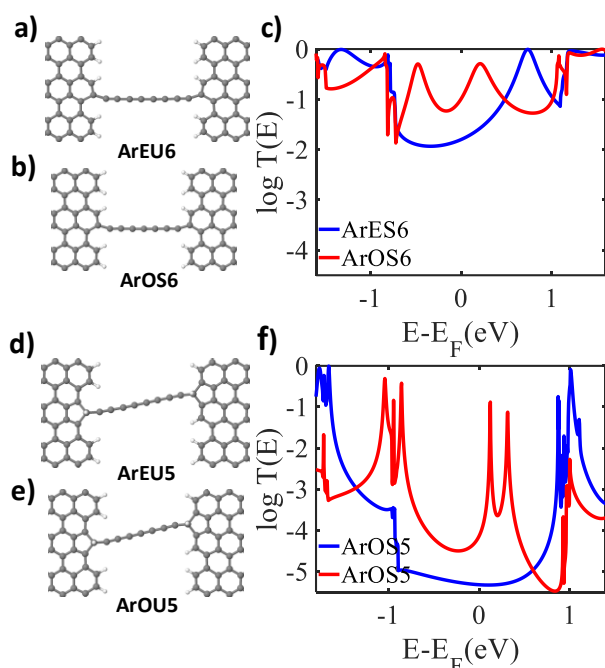


Figure 5.2.3. Results from DFT simulations of armchair structures with odd and even numbered carbon chains. (a) Relaxed atomic structure of an even (8) numbered carbon chain connected to saturated armchair edges via a six membered terminal ring (ArES6). (b) Relaxed atomic structure of an odd (7) numbered carbon chain, connected to saturated armchair edges via six membered terminal rings (ArOS6) (c) Transmission coefficient obtained from DFT for structures (a) and (b). (d) Relaxed atomic structure of an even (8) numbered carbon chain connected to saturated armchair edges via five membered terminal rings (ArES5). (e) Relaxed atomic structure of an odd (7) numbered of carbon chain connected to saturated armchair edges via five membered terminal ring (ArOS5) (c) Transmission coefficients for structures (d) and (e).

Figure 5.2.3c shows the transmission coefficient of structures ArES6 (Figure 5.2.3a) and ArOS6 (Figure 5.2.3b), which only differ by a single carbon atom in their atomic chains. Clearly the structure ArOS6 with an odd-numbered chain possesses extra

transmission resonances within the HOMO-LUMO gap. As shown in fig (5.2.4.), these are due to two singly occupied molecular orbitals (SOMOs) in structures such as ArOS6, bridged by an odd-numbered chain. As shown in Figure 5.2.3f, these extra resonances for odd-numbered chains are also present when the chain is connected to the graphene via five-membered rings.

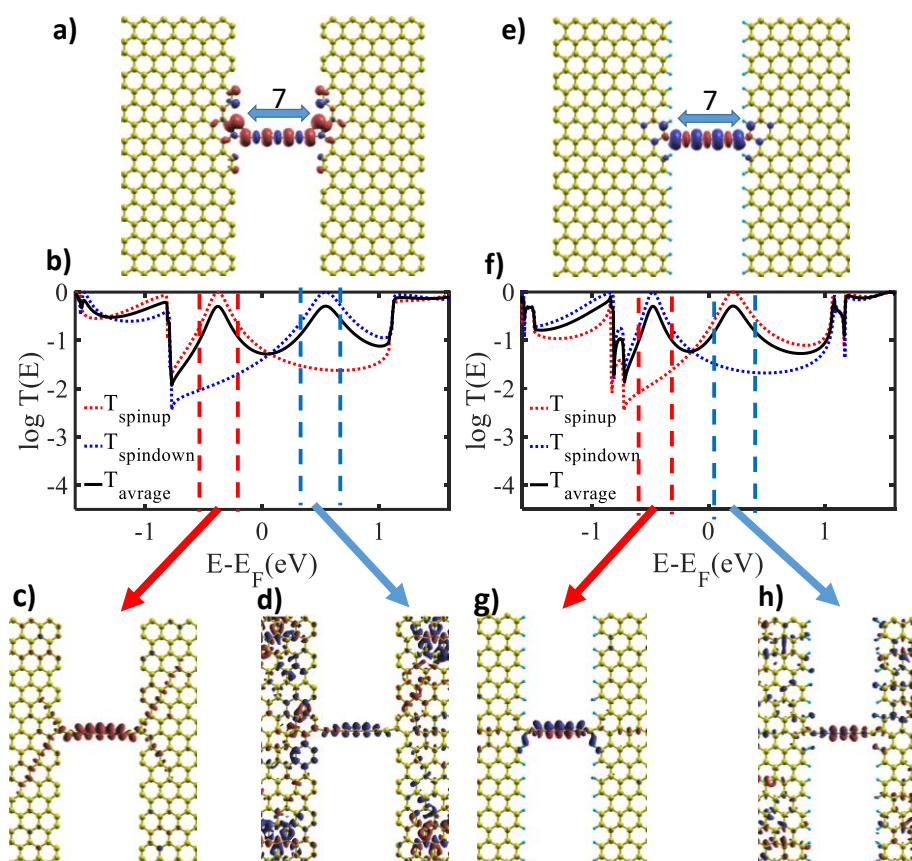


Figure 5.2.4. Schematic representation of the atomic graphene junction. (a) and (e) Spin densities ($\rho_{\uparrow} - \rho_{\downarrow}$) of an odd (7) numbered carbon chain connected to unsaturated and saturated armchair edges via six membered terminal rings (ArOU6) (ArOS6). Results from DFT simulations (b), (f) DFT transmission coefficients with antiferromagnetic spin order for structures (a), (e) respectively. (c),(d),(g),(h),(c) The distributions of the HOMO and LUMO orbital.

Figure 5.2.4a and c shows the spin densities ($\rho_{\uparrow} - \rho_{\downarrow}$) of both (ArES6) and (ArOS6), where blue and red correspond to positive and negative isosurfaces of ($\rho_{\uparrow} - \rho_{\downarrow}$). It is known that an odd carbon chain is radical system, for this reason it is clear to see most of the weight of spin densities on a carbon chain of the structure 5.2.4c. I calculated the

transmission coefficient of structures (ArES6), (ArOS6) as shown in figures 5.2.4b and d respectively. Clearly, transmission coefficients of these structures are significantly affected by the change number of carbon chain from odd to even.

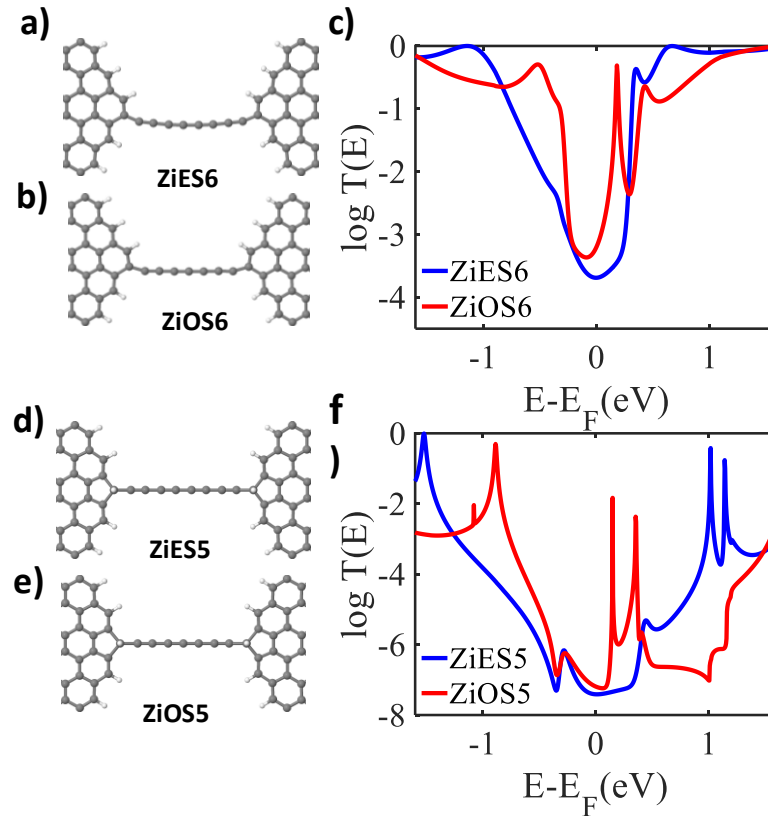


Figure 5.2.5. Results from DFT simulations of zig-zag structures with odd and even numbered carbon chains. (a) Relaxed atomic structure of an even (8) numbered carbon chain connected to saturated armchair edges via a six membered terminal ring (ArES6). (b) Relaxed atomic structure of an odd (7) numbered carbon chain, connected to saturated armchair edges via six membered terminal rings (ArOS6) (c) Transmission coefficient obtained from DFT for structures (a) and (b). (d) Relaxed atomic structure of an even (8) numbered carbon chain connected to saturated armchair edges via five membered terminal rings (ArES5). (e) Relaxed atomic structure of an odd (7) numbered of carbon chain connected to saturated armchair edges via five membered terminal ring (ArOS5) (c) Transmission coefficients for structures (d) and (e).

For comparison with the armchair structures of Figure 5.2.5, Figure 5.2.5c shows the transmission coefficient of structures ZiES6 (Figure 5.2.5a) and ZiOS6 (Figure 5.2.5b), which again differ by only a single carbon atom in their atomic chains. In common with the armchair structures of Figure 5.2.4 containing odd-numbered chains, the structures ZiOS6 and ZiOS5 with odd-numbered chains possess extra transmission resonances

within the HOMO-LUMO gap. As shown in Figure 5.2.6, these are due to two SOMOs located on the chain of ZiOS6.

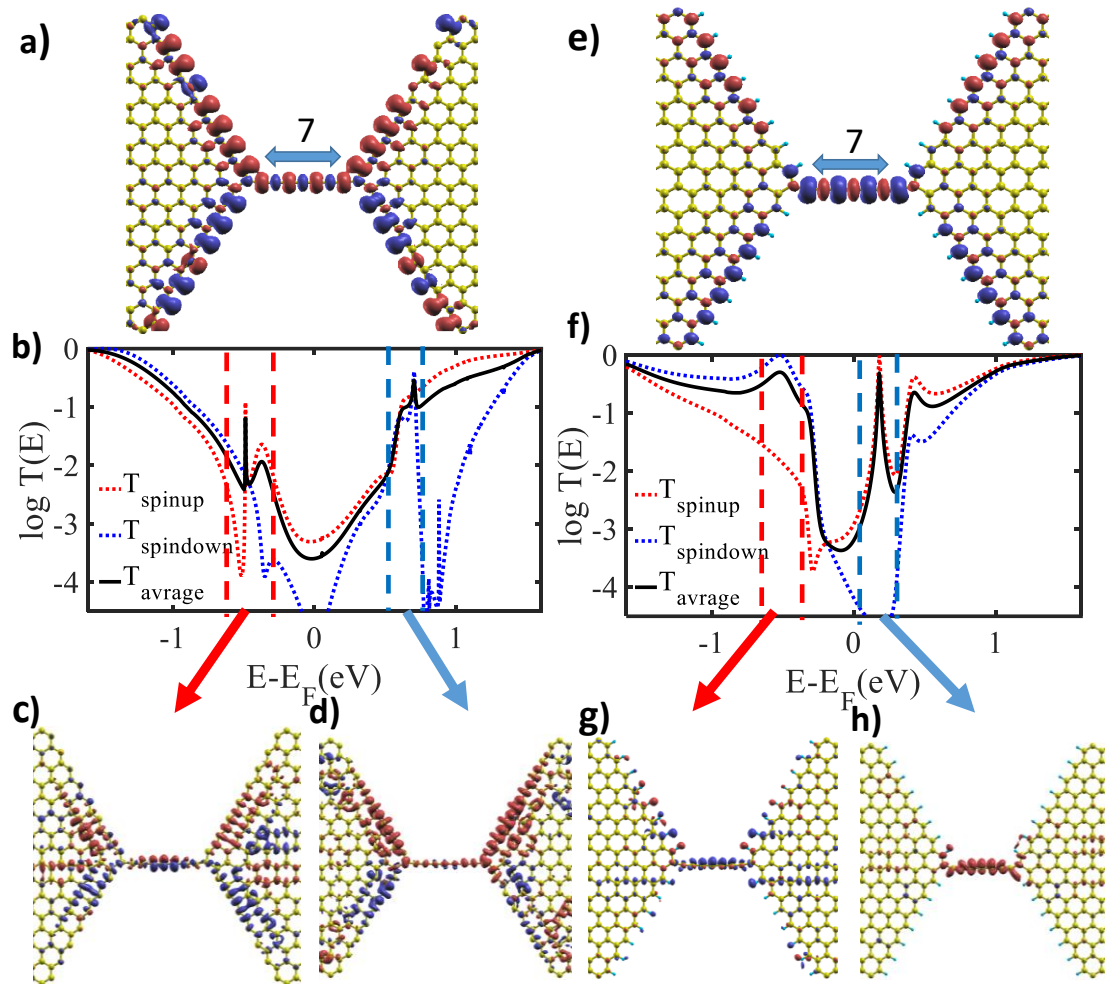


Figure 5.2.6. Schematic representation of the atomic graphene junction. (a) and (e) Spin densities ($\rho_{\uparrow} - \rho_{\downarrow}$) of an odd (7) numbered carbon chain connected to unsaturated and saturated zigzag edges via six membered terminal rings (ZiOU6) (ZiOS6). Results from DFT simulations (b), (f) DFT transmission coefficients with antiferromagnetic spin order for structures (a), (e) respectively. (c),(d),(g),(h),(c) The distributions of the HOMO and LUMO orbital.

Figure (5.2.7) shows spin densities ($\rho_{\uparrow} - \rho_{\downarrow}$), DFT transmission coefficients with antiferromagnetic spin order and local densities of states of HOMO and LUMO resonances of symmetric ZiEU6, ZiES6, ArEU6 and ArES6 junctions.

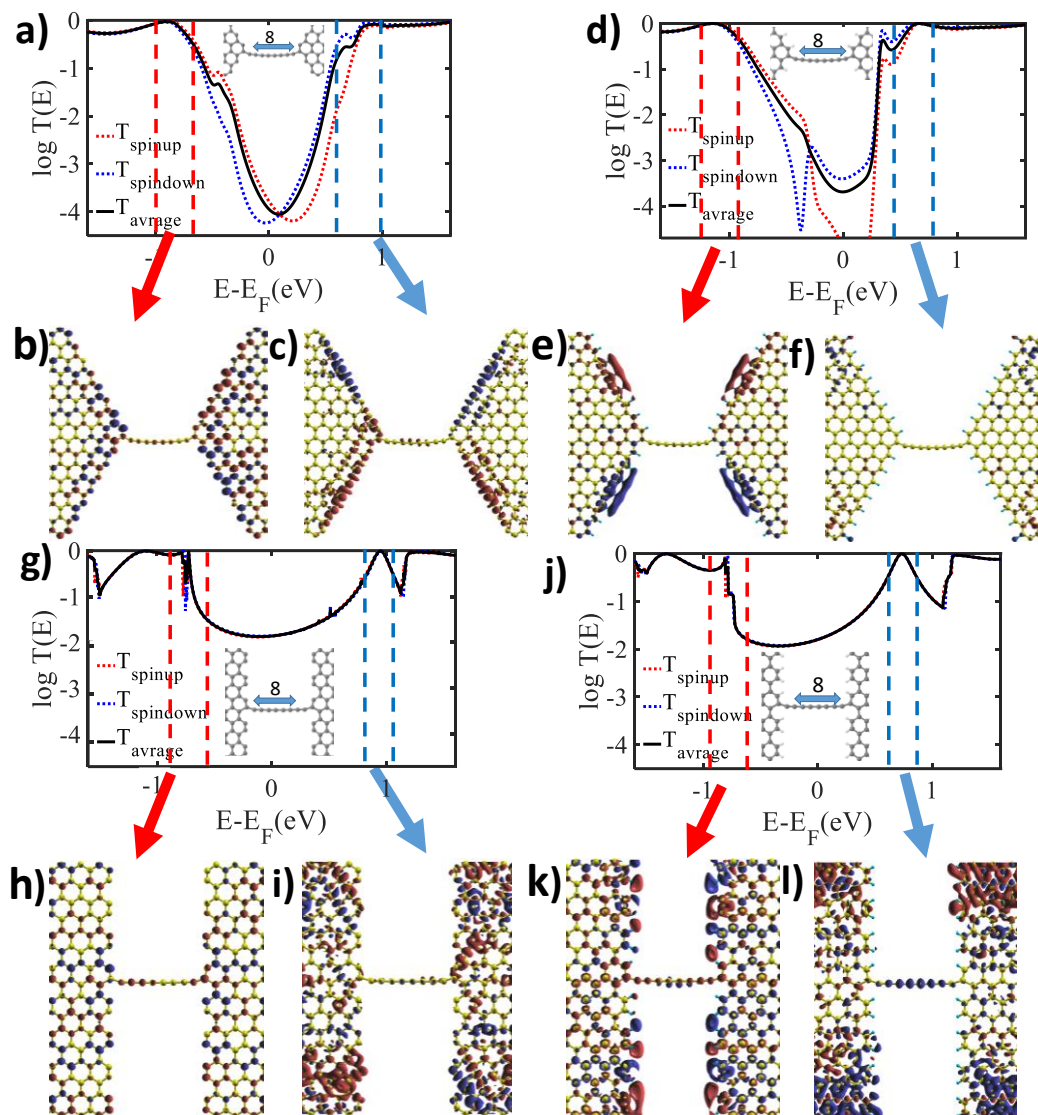


Figure 5.2.6. Schematic representation of the atomic graphene junction. a,d) DFT transmission coefficients with antiferromagnetic spin order for relaxed atomic structure of an even (8) numbered carbon chain connected to unsaturated and saturated zigzag edges via six membered terminal rings (ZiEU6) (ZiES6). g,j) DFT transmission coefficients with antiferromagnetic spin order for Relaxed atomic structure of an even (8) numbered carbon chain connected to unsaturated and saturated armchair edges via six membered terminal rings (ArEU6) (ArES6). b,c,e,f,h,i,k,l) The distributions of the HOMO and LUMO orbital

In next pages many more examples of graphene based junctions are analyzed.

Even when the edges of the two electrodes are identical, the carbon chain can attach, such that the overall junction is either symmetric or asymmetric. Figures (5.2.7) and (5.2. (5.2.12) show total and spin-resolved transmissions and spin densities of

symmetric ZiEU6, ZiES6, ArEU6 and ArES6 junctions, with even-numbered chains attached to anti-ferromagnetically and ferromagnetically aligned edges.

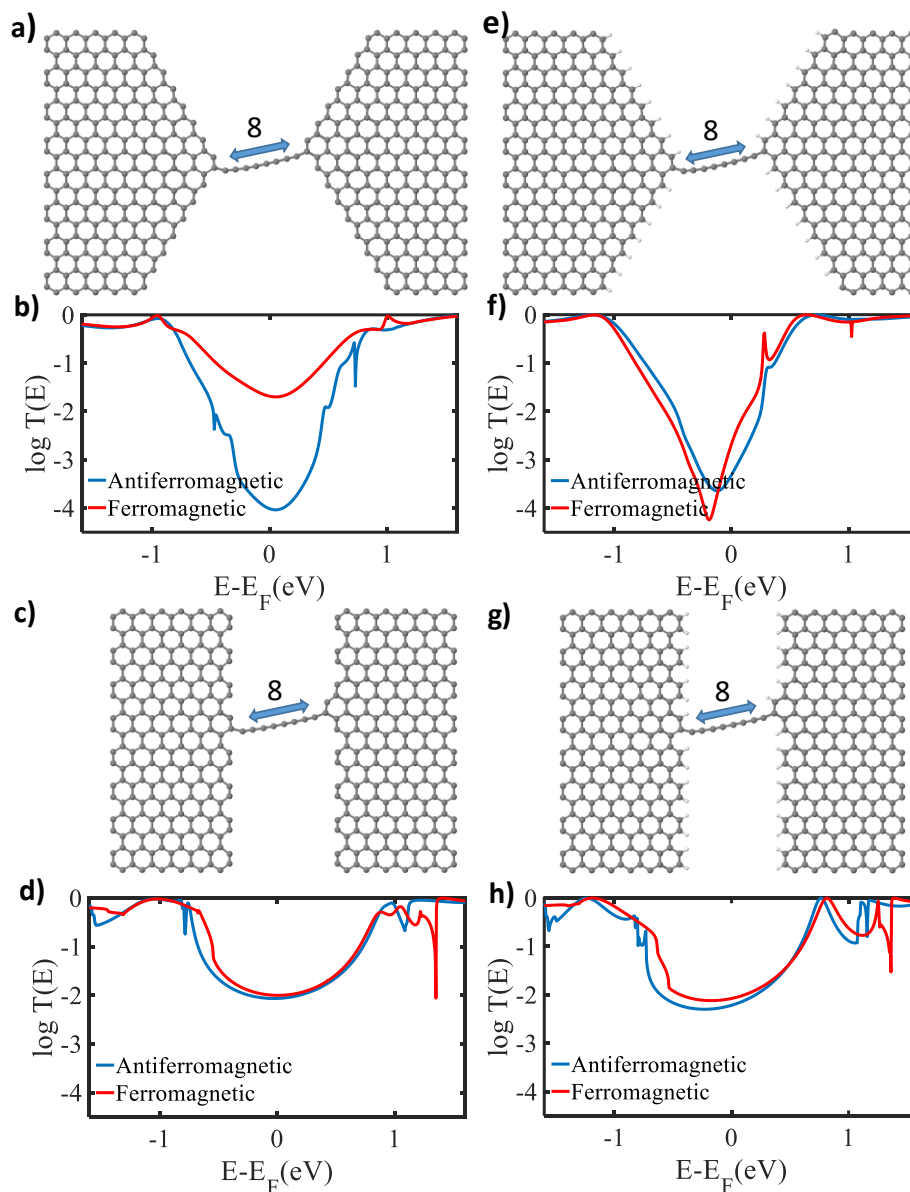


Figure 5.2.7. Schematic representation of the atomic graphene junction. (a) and (e) Relaxed atomic structure of an even (8) numbered carbon chain connected to unsaturated and saturated zigzag edges via six membered terminal rings (ZiEU6) (ZiES6). (c) and (g) Relaxed atomic structure of an even (8) numbered carbon chain connected to unsaturated and saturated armchair edges via six membered terminal rings (ArEU6)(ArES6). (b), (f), (d) and (h) DFT transmission coefficients with antiferromagnetic and ferromagnetic spin order for structures (a), (c), (e) and (g) respectively.

Figure (5.2.7) shows the comparison between total transmissions of ferromagnetic and anti-ferromagnetic edges of asymmetric ZiEU6, ZiES6, ArEU6 and ArES6 junctions. It is clear to see a conductance at ferromagnetic spin order higher than

ferromagnetic spin order as shown in figure (7a), while it is almost equal with other structures.

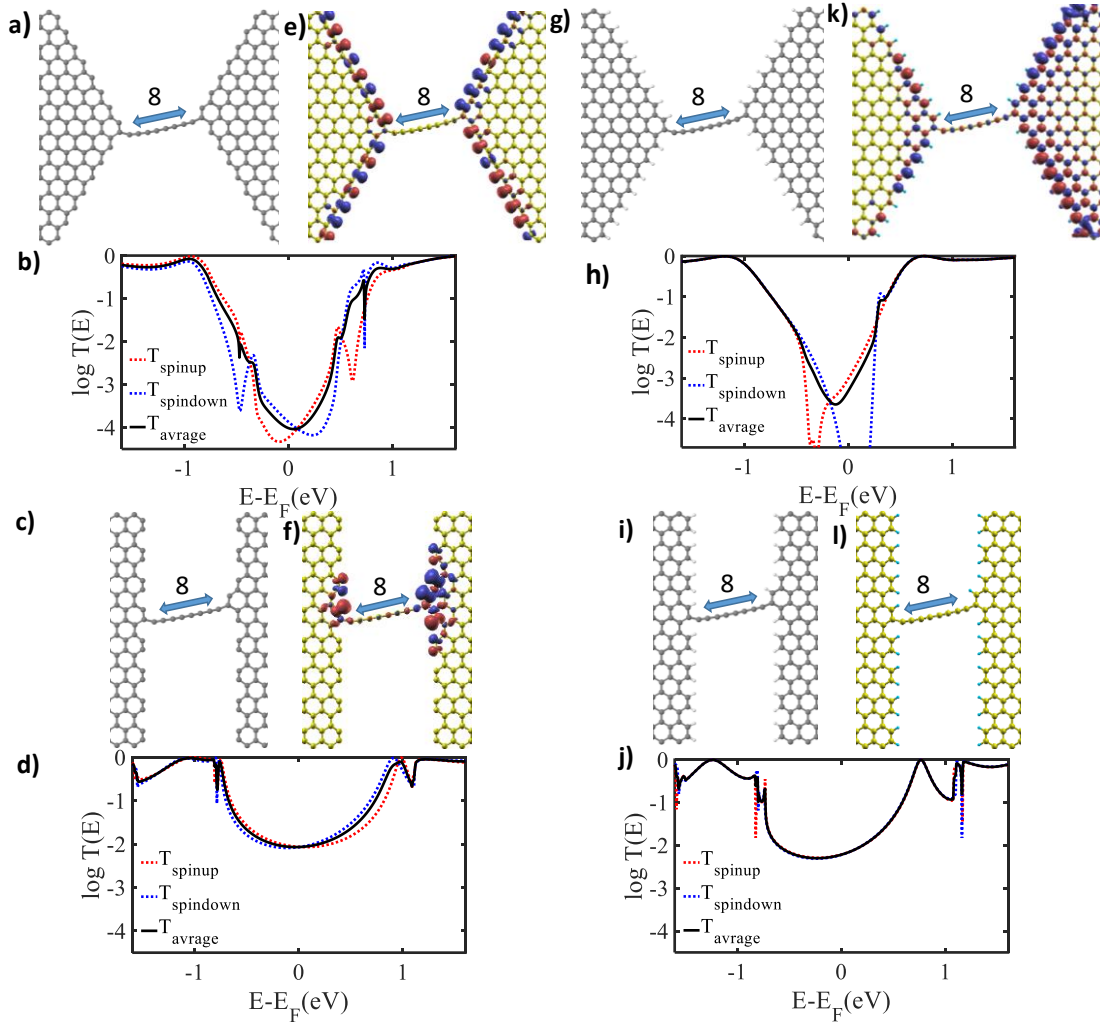


Figure 5.2.8. Schematic representation of the atomic graphene junction. (a) and (g) Relaxed atomic structure of an even (8) numbered carbon chain connected to unsaturated and saturated zigzag edges via six membered terminal rings (ZiEU6) (ZiES6). (c) and (i) Relaxed atomic structure of an even (8) numbered carbon chains connected to unsaturated and saturated armchair edges via six membered terminal rings (ArEU6) (ArES6). (e), (f), (k and l) Spin densities ($\rho_{\uparrow} - \rho_{\downarrow}$) structures (a), (c), (g) and (i) respectively. Blue and red correspond to positive and negative isosurfaces of ($\rho_{\uparrow} - \rho_{\downarrow}$). (b), (d), (h) and (j) DFT transmission coefficients with antiferromagnetic spin order for structures (a), (c), (g) and (i) respectively.

Figure 5.2.8 shows spin-resolved transmissions and spin densities of *asymmetric* ZiEU6, ZiES6, ArEU6 and ArES6 junctions, with even-numbered chains attached to anti-ferromagnetically aligned edges,

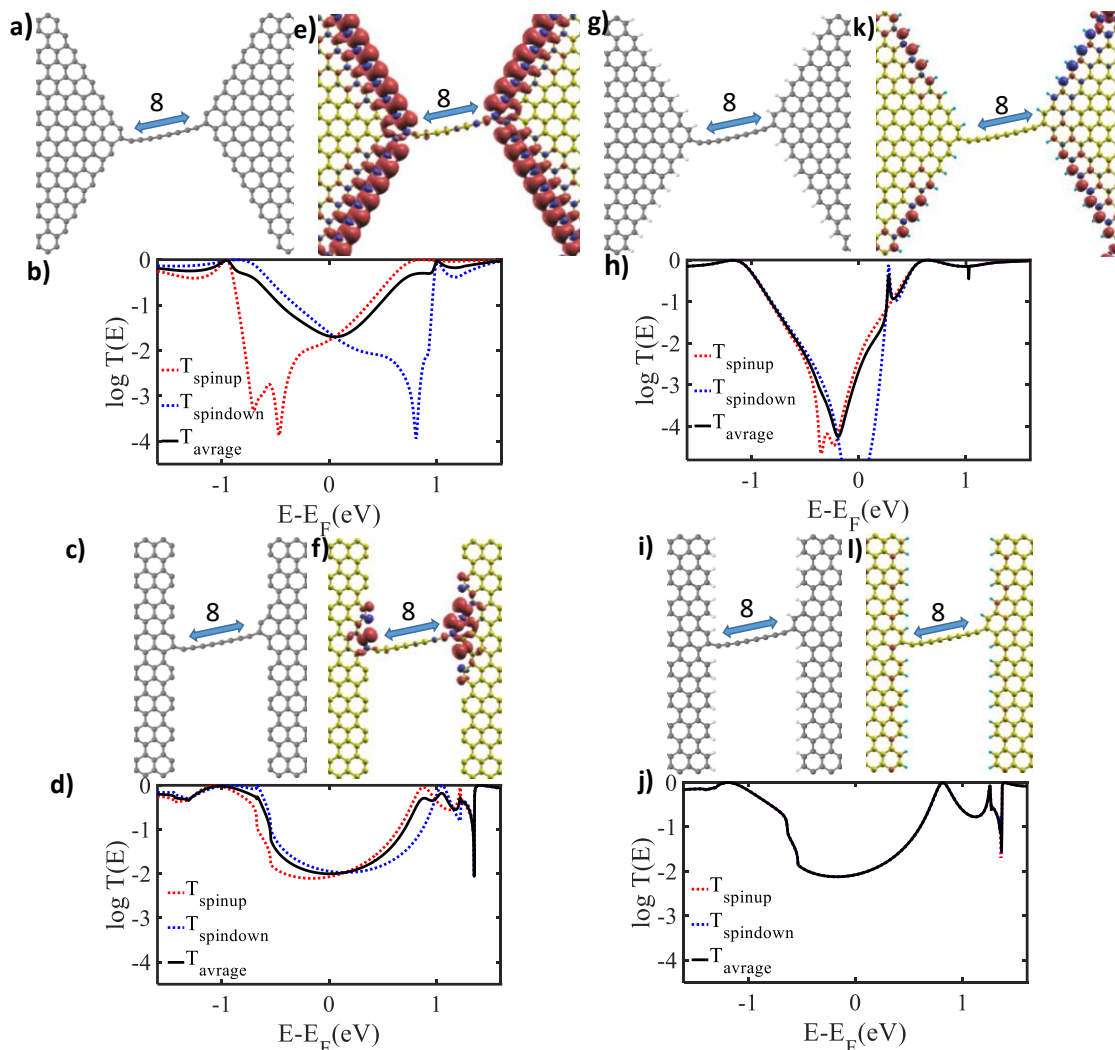


Figure 5.2.9. Schematic representation of the atomic graphene junction. (a) and (g) Relaxed atomic structure of an even (8) numbered carbon chain connected to unsaturated and saturated zigzag edges via six membered terminal rings (ZiEU6) (ZiES6). (c) and (i) Relaxed atomic structure of an even (8) numbered carbon chains connected to unsaturated and saturated armchair edges via six membered terminal rings (ArEU6) (ArES6). (e), (f), (k) and (l) Spin densities ($\rho_{\uparrow} - \rho_{\downarrow}$) structures (a), (c), (g) and (i) respectively. Blue and red correspond to positive and negative isosurfaces of ($\rho_{\uparrow} - \rho_{\downarrow}$). (b), (d), (h) and (j) DFT transmission coefficients with ferromagnetic spin order for structures (a), (c), (g) and (i) respectively.

Figure 5.2.9 shows spin-resolved transmissions and spin densities of *asymmetric* ZiEU6, ZiES6, ArEU6 and ArES6 junctions, with even-numbered chains attached to ferromagnetically aligned edges.

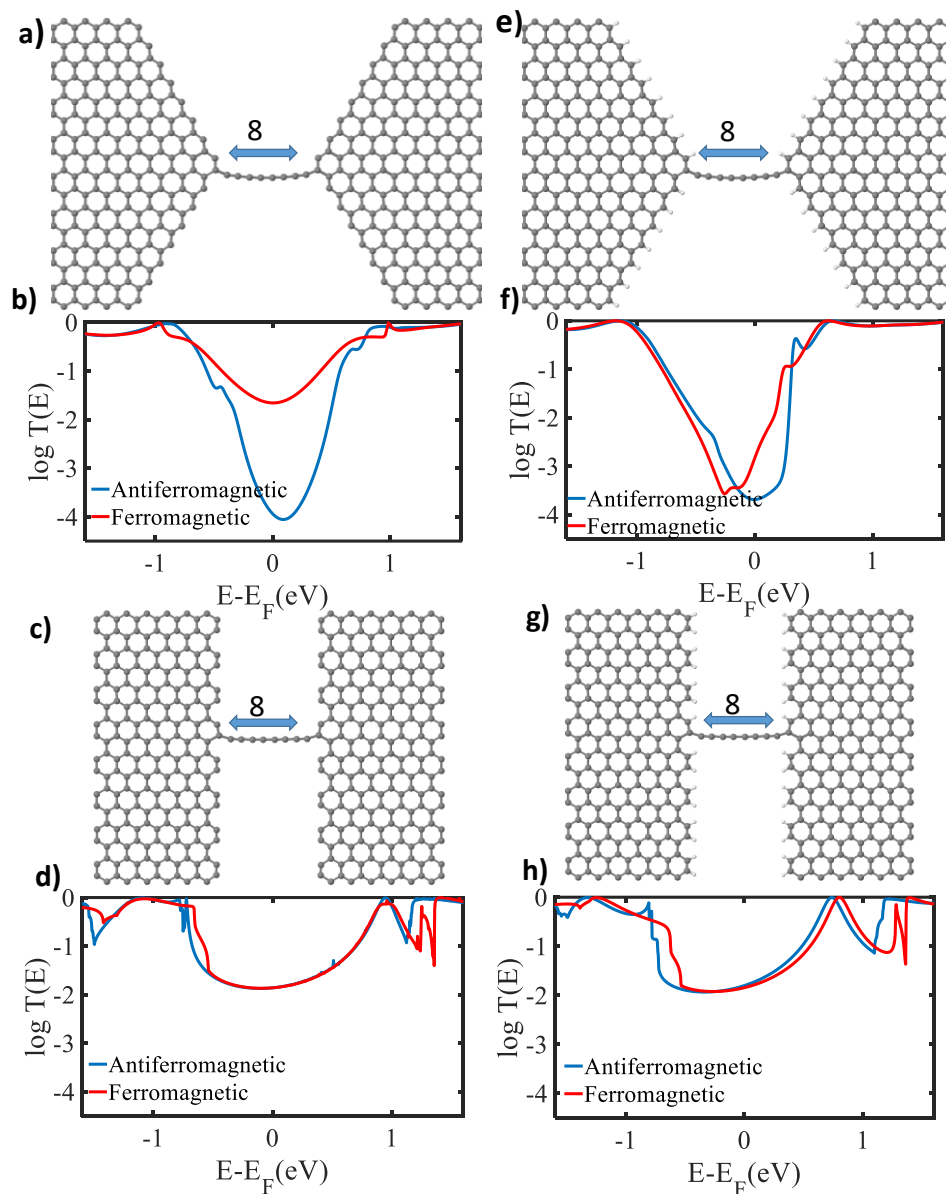


Figure 5.2.10. Schematic representation of the atomic graphene junction. (a) and (e) Relaxed atomic structure of an even (8) numbered carbon chain connected to unsaturated and saturated zigzag edges via six membered terminal rings (ZiEU6) (ZiES6). (c) and (g) Relaxed atomic structure of an even (8) numbered carbon chain connected to unsaturated and saturated armchair edges via six membered terminal rings (ArEU6)(ArES6). (b), (f), (d) and (h) DFT transmission coefficients with antiferromagnetic and ferromagnetic spin order for structures (a), (c), (e) and (g) respectively.

Figure (5.2.10) shows the comparison between total transmissions of ferromagnetic and anti-ferromagnetic edges of symmetric ZiEU6, ZiES6, ArEU6 and ArES6 junctions. By comparing between Figures (5.2.10) and (5.2.7) shows the transmissions behavior almost equal at asymmetric and symmetric ZiEU6, ZiES6, ArEU6 and ArES6 junctions

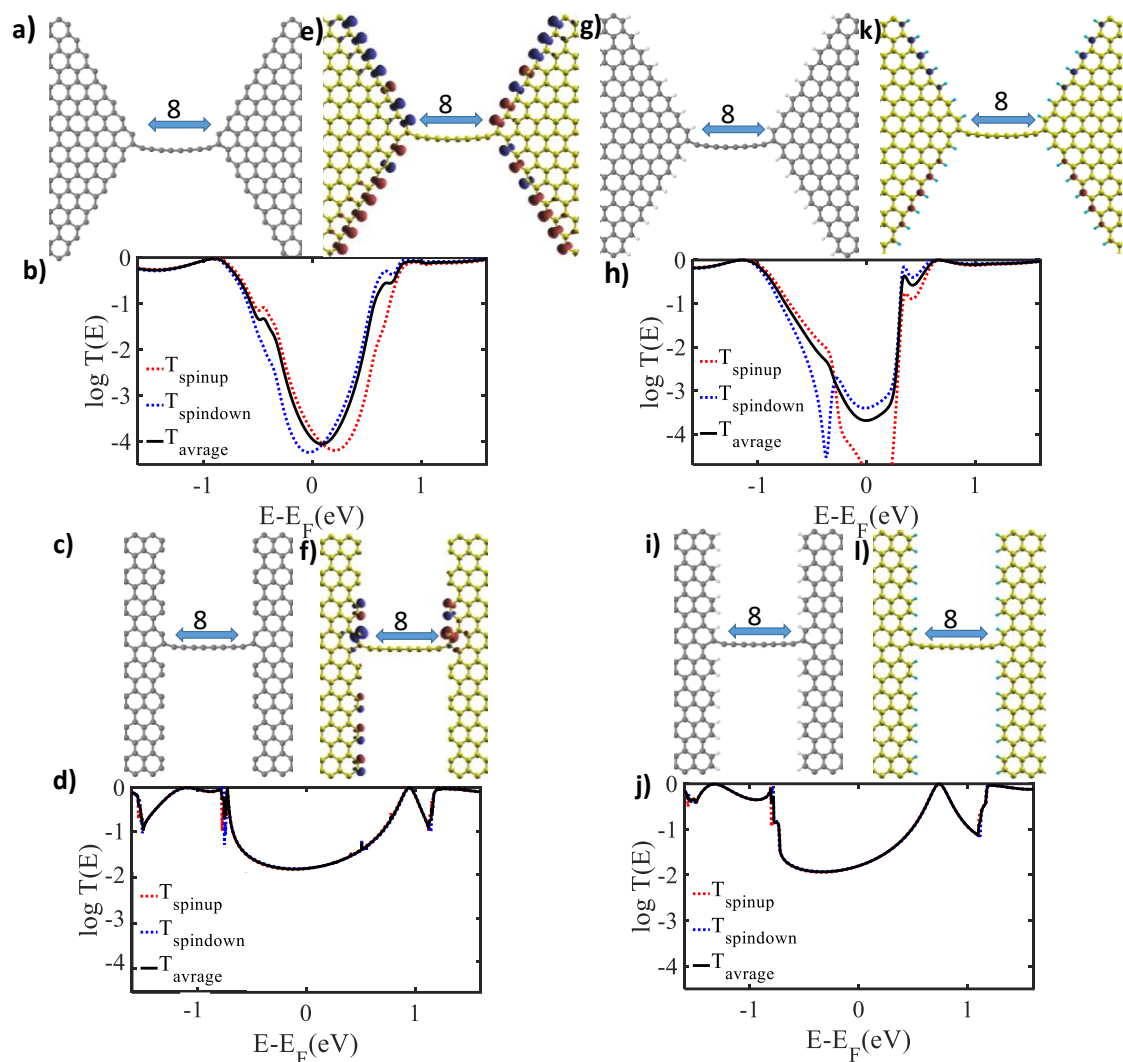


Figure 5.2.11. Schematic representation of the atomic graphene junction. (a) and (g) Relaxed atomic structure of an even (8) numbered carbon chain connected to unsaturated and saturated zigzag edges via six membered terminal rings (ZiEU6) (ZiES6). (c) and (i) Relaxed atomic structure of an even (8) numbered carbon chains connected to unsaturated and saturated armchair edges via six membered terminal rings (ArEU6) (ArES6). (e), (f), (k) and (l) Spin densities ($\rho_{\uparrow} - \rho_{\downarrow}$) structures (a), (c), (g) and (i) respectively. Blue and red correspond to positive and negative isosurfaces of ($\rho_{\uparrow} - \rho_{\downarrow}$). (b), (d), (h) and (j) DFT transmission coefficients with antiferromagnetic spin order for structures (a), (c), (g) and (i) respectively.

Figure 5.2.11 shows spin-resolved transmissions and spin densities of *symmetric* ZiEU6, ZiES6, ArEU6 and ArES6 junctions, with even-numbered chains attached to anti-ferromagnetically aligned edges.

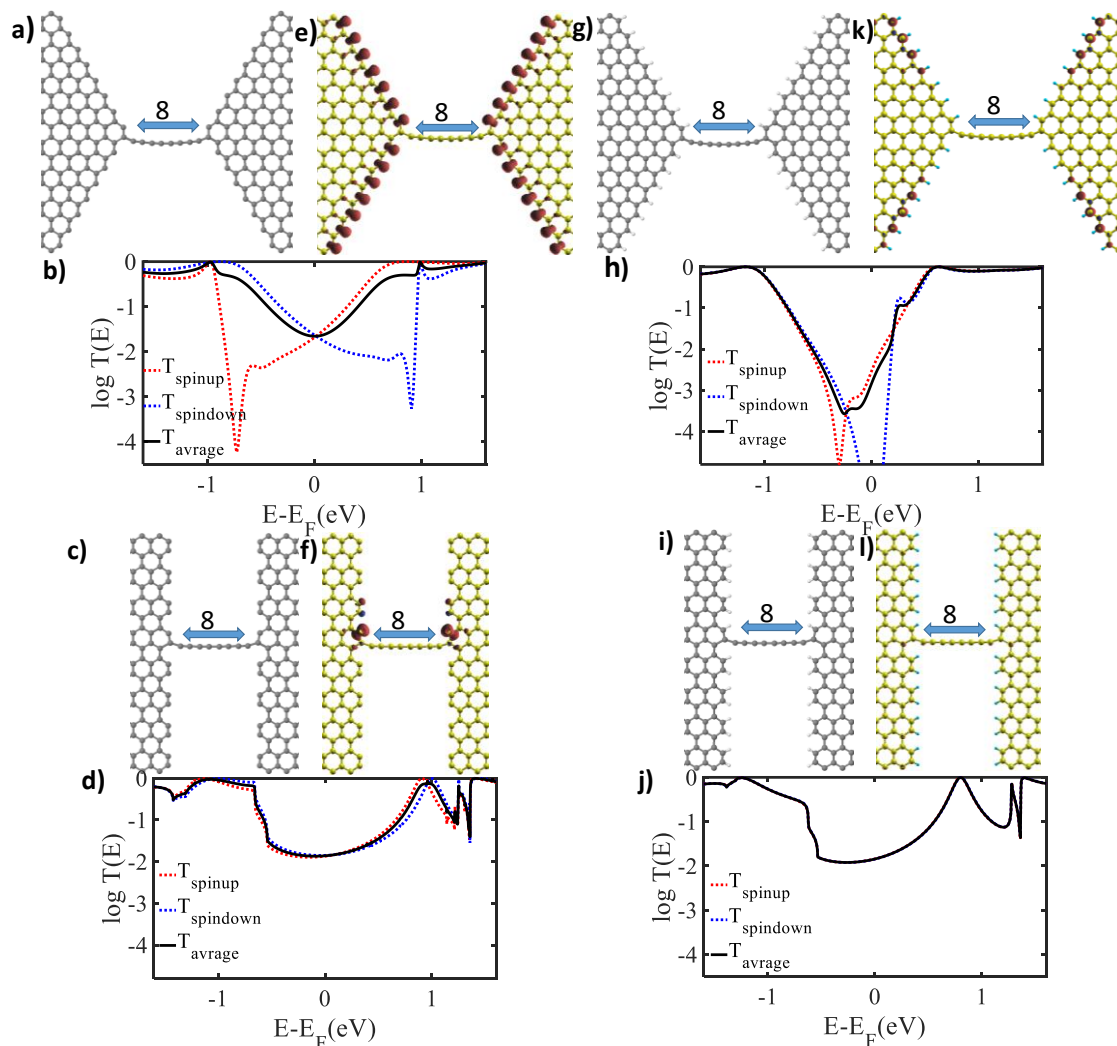


Figure 5.2.12. Schematic representation of the atomic graphene junction. (a) and (g) Relaxed atomic structure of an even (8) numbered carbon chain connected to unsaturated and saturated zigzag edges via six membered terminal rings (ZiEU6) (ZiES6). (c) and (i) Relaxed atomic structure of an even (8) numbered carbon chains connected to unsaturated and saturated armchair edges via six membered terminal rings (ArEU6) (ArES6). (e), (f), (k and l) Spin densities ($\rho_{\uparrow} - \rho_{\downarrow}$) structures (a), (c), (g) and (i) respectively. Blue and red correspond to positive and negative isosurfaces of ($\rho_{\uparrow} - \rho_{\downarrow}$). (b), (d), (h) and (j) DFT transmission coefficients with ferromagnetic spin order for structures (a), (c), (g) and (i) respectively.

Figure 5.2.8 shows spin-resolved transmissions and spin densities of *symmetric* ZiEU6, ZiES6, ArEU6 and ArES6 junctions, with even-numbered chains attached to ferromagnetically aligned edges.

Corresponding junctions with 5-membered terminal rings are shown in (5.2.13) – (5.2.18). In this case, I distinguish between 5-membered rings, which are unsaturated

(ie the apex carbon attached to the carbon chain is unsaturated) or saturated (ie the apex carbon attached to the carbon chain is also bound to a hydrogen atom).

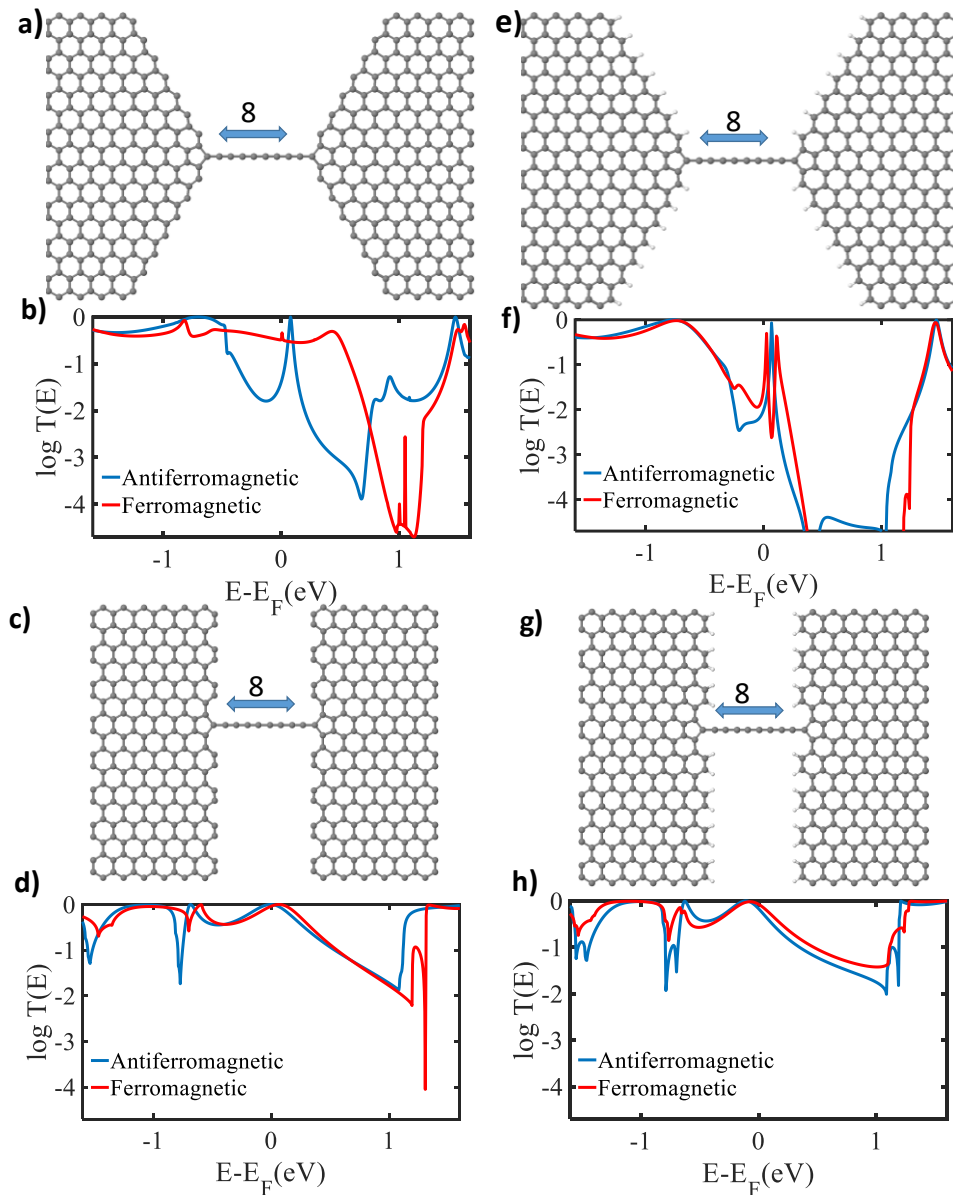


Figure 5.2.13. Schematic representation of the atomic graphene junction. (a) and (e) Relaxed atomic structure of an even (8) numbered carbon chain connected to unsaturated and saturated zigzag edges via unsaturated five membered terminal rings (ZiEU5) (ZiES5). (c) and (g) Relaxed atomic structure of an even (8) numbered carbon chain connected to unsaturated and saturated armchair edges via unsaturated five membered terminal rings (ArEU6) (ArES6). (b), (f), (d) and (h) DFT transmission coefficients with antiferromagnetic and ferromagnetic spin order for structures (a), (c), (e) and (g) respectively.

Figures (5.2.13) shows the comparison between total transmissions of ferromagnetic and anti-ferromagnetic edges of symmetric ZiEU5, ZiES5, ArEU5 and ArES5 junctions, with even-numbered carbon chains attached to unsaturated 5-membered terminal rings

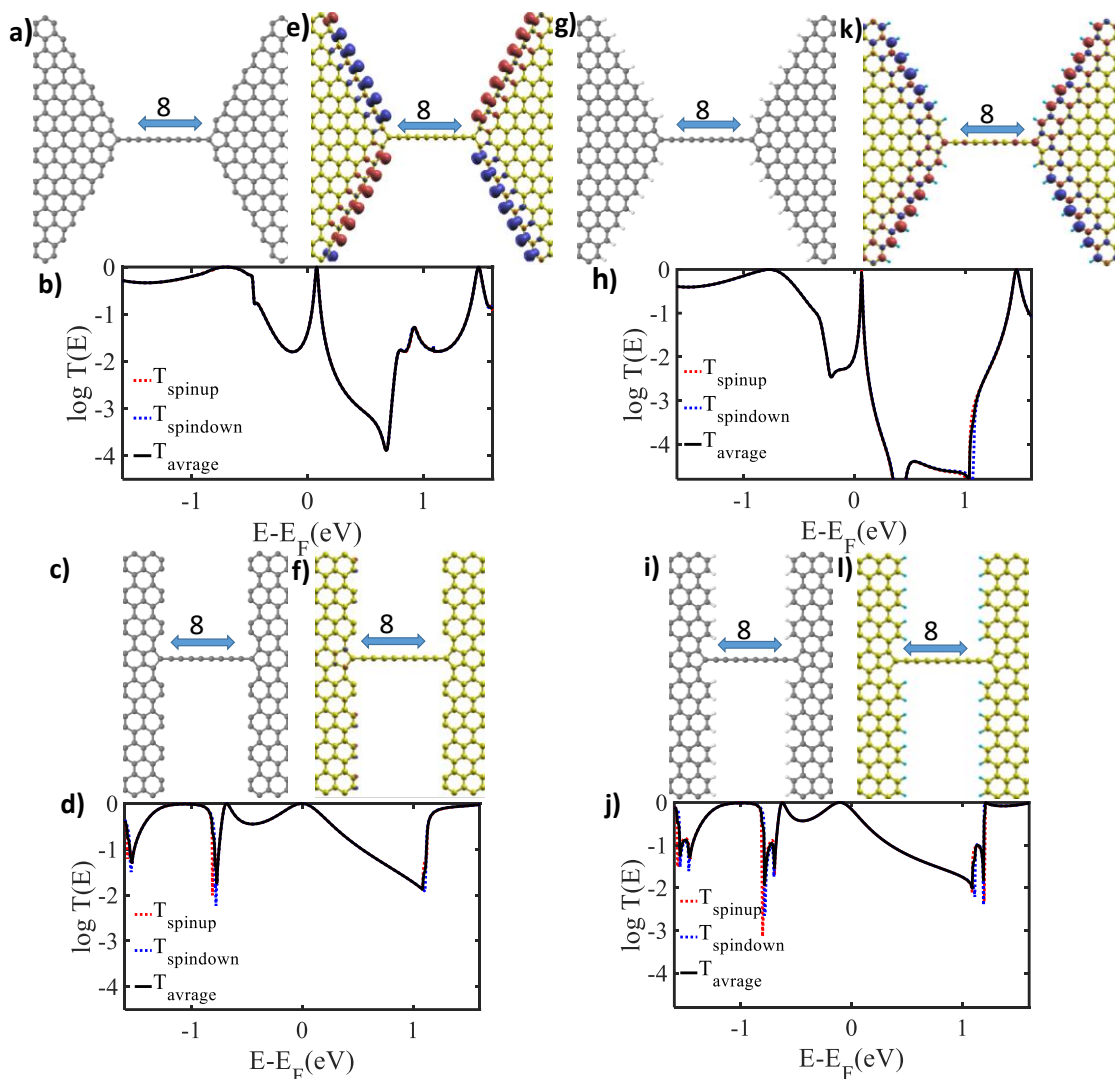


Figure 5.2.14. Schematic representation of the atomic graphene junction. (a) and (g) Relaxed atomic structure of an even (8) numbered carbon chain connected to unsaturated and saturated zigzag edges via unsaturated five membered terminal rings (ZiEU5) (ZiES5). (c) and (i) Relaxed atomic structure of an even (8) numbered carbon chains connected to unsaturated and saturated armchair edges via unsaturated five membered terminal rings (ArEU5) (ArES5). (e), (f), (k) and (l) Spin densities ($\rho_{\uparrow} - \rho_{\downarrow}$) structures (a), (c), (g) and (i) respectively. Blue and red correspond to positive and negative isosurfaces of ($\rho_{\uparrow} - \rho_{\downarrow}$). (b), (d), (h) and (j) DFT transmission coefficients with antiferromagnetic spin order for structures (a), (c), (g) and (i) respectively.

Figure 5.2.14 shows spin-resolved transmissions and spin densities of symmetric ZiEU5, ZiES5, ArEU5 and ArES5 junctions, with even-numbered chains attached to unsaturated 5-membered terminal rings to anti-ferromagnetically aligned edges.

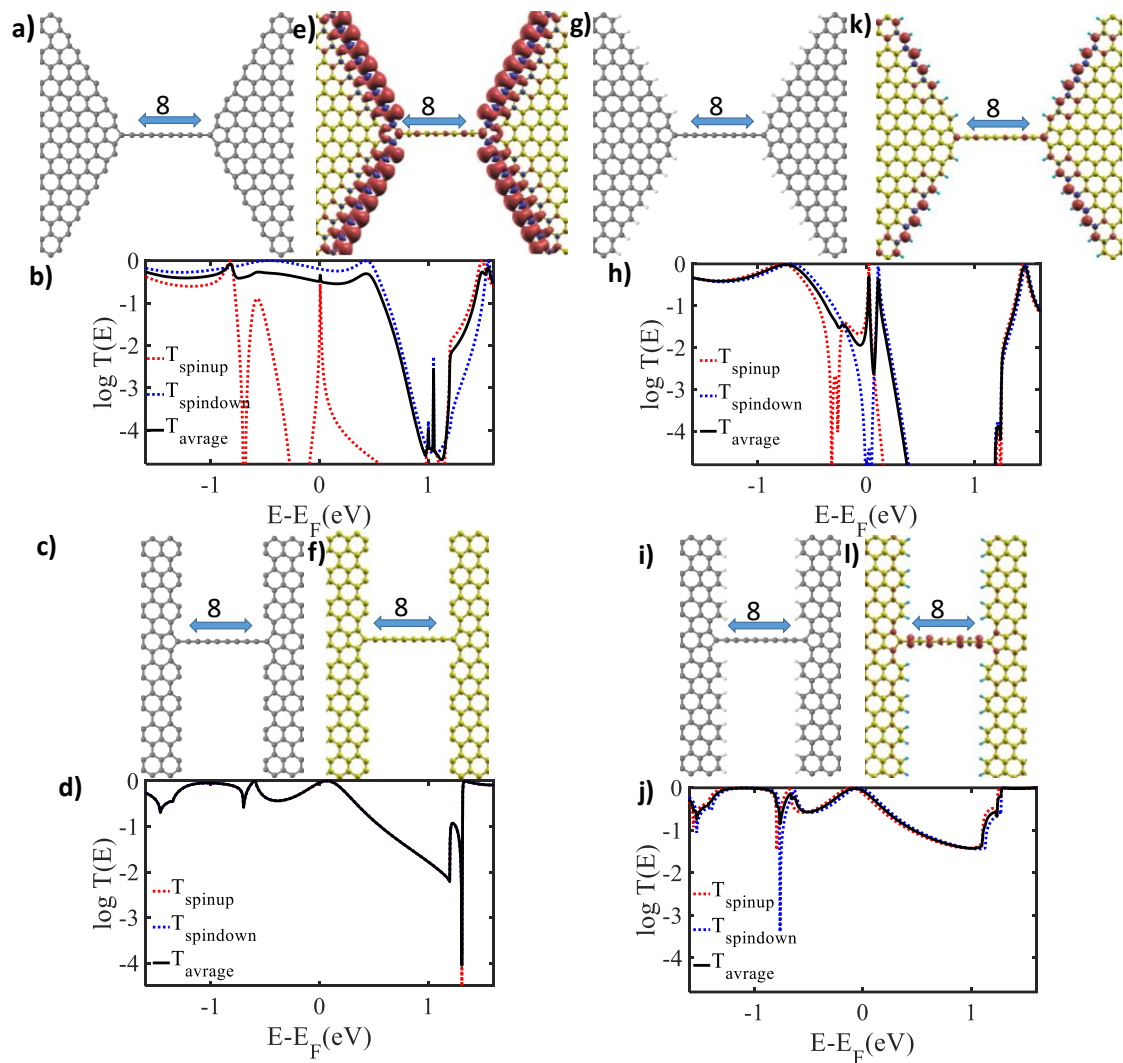


Figure 5.2.15. Schematic representation of the atomic graphene junction. (a) and (g) Relaxed atomic structure of an even (8) numbered carbon chain connected to unsaturated and saturated zigzag edges via unsaturated five membered terminal rings (ZiEU5) (ZiES5). (c) and (i) Relaxed atomic structure of an even (8) numbered carbon chains connected to unsaturated and saturated armchair edges via unsaturated five membered terminal rings (ArEU5) (ArES5). (e), (f), (k) and (l) Spin densities ($\rho_{\uparrow} - \rho_{\downarrow}$) structures (a), (c), (g) and (i) respectively. Blue and red correspond to positive and negative isosurfaces of ($\rho_{\uparrow} - \rho_{\downarrow}$). (b), (d), (h) and (j) DFT transmission coefficients with ferromagnetic spin order for structures (a), (c), (g) and (i) respectively.

Figure 5.2.15 shows spin-resolved transmissions and spin densities of symmetric ZiEU5, ZiES5, ArEU5 and ArES5 junctions, with even-numbered chains attached to unsaturated 5-membered terminal rings to ferromagnetically aligned edges.

For even-numbered carbon chains attached to saturated 5-membered terminal rings, Figures (5.2.16) – (5.2.18) show total and spin-resolved transmissions and spin densities of ZiEU5, ZiES5, ArEU5 and ArES5 junctions, with ferromagnetically aligned or anti-ferromagnetically aligned edges.

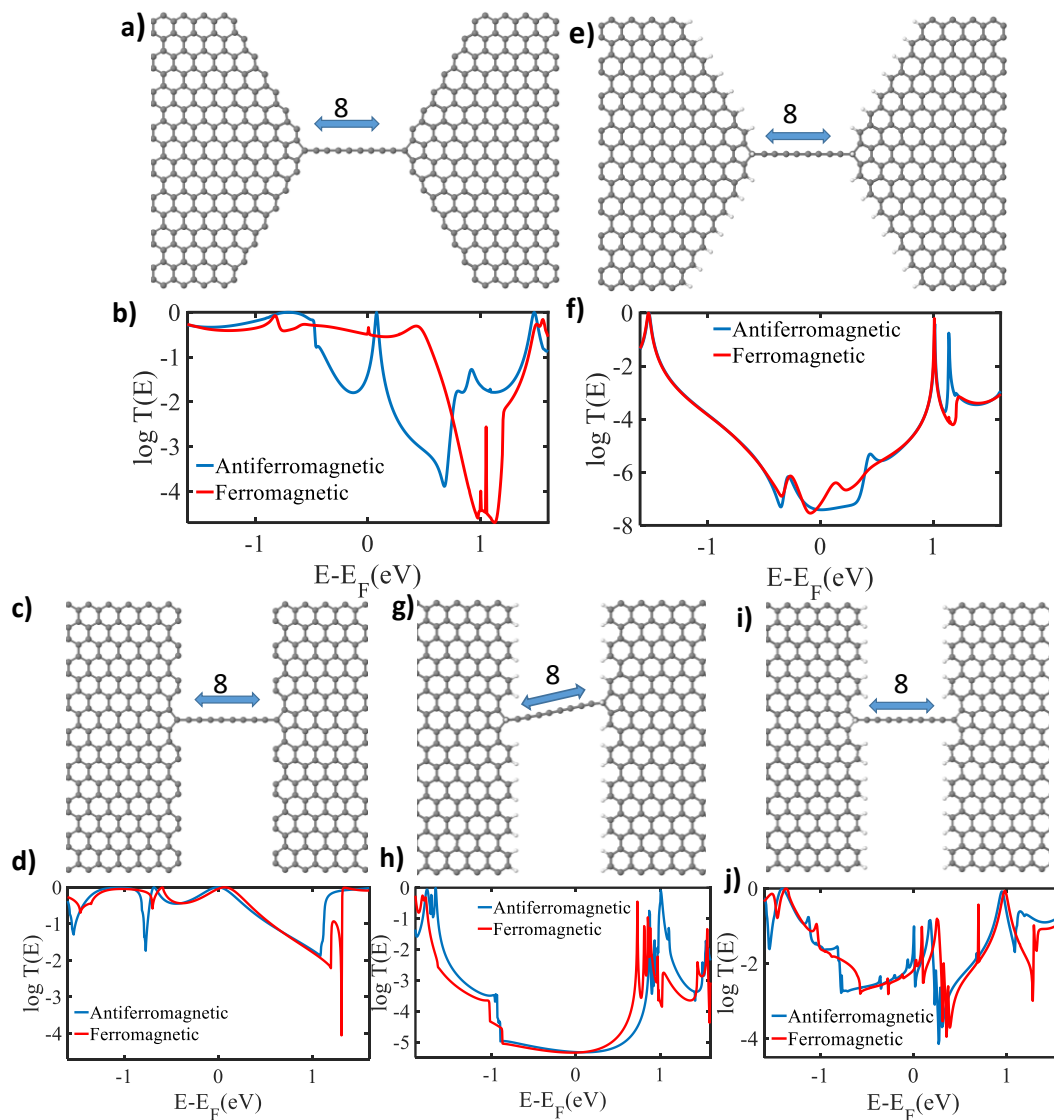


Figure 5.2.16. Schematic representation of the atomic graphene junction. (a) and (e) Relaxed atomic structure of an even (8) numbered carbon chain connected to unsaturated and saturated zigzag edges via saturated five membered terminal rings (ZiEU5) (ZiES5). (c) and (g) Relaxed atomic structure of an even (8) numbered carbon chain connected to unsaturated and saturated armchair edges via saturated five membered terminal rings (ArEU5) (ArES5). (i) Relaxed atomic structure of an even (8) numbered carbon chain connected to saturated armchair edges via saturated five membered terminal ring (ArES5). (b), (d), (f), (h), and (j) DFT transmission coefficients with antiferromagnetic and ferromagnetic spin order for structures (a), (c), (e) and (g) respectively.

Figure (5.2.16) shows the comparison between total transmissions of ferromagnetic and anti-ferromagnetic edges of symmetric ZiEU5, ZiES5, ArEU5 and ArES5 junctions, with even-numbered carbon chains attached to saturated 5-membered terminal rings, fig16g,i) how symmetric and asymmetric effect on transmissions behavior.

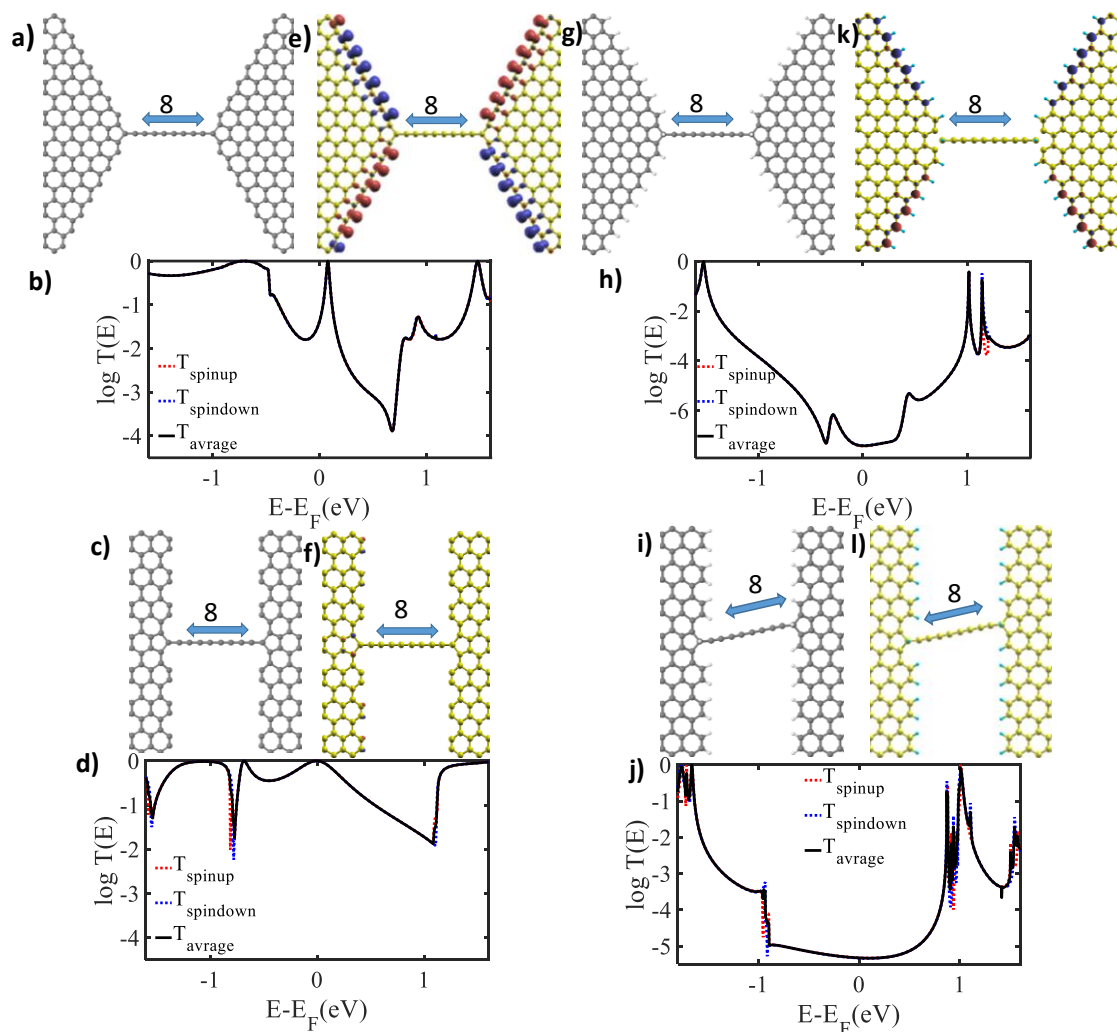


Figure 5.2.17. Schematic representation of the atomic graphene junction. (a) and (g) Relaxed atomic structure of an even (8) numbered carbon chain connected to unsaturated and saturated zigzag edges via five membered terminal rings (ZiEU5) (ZiES5). (c) and (i) Relaxed atomic structure of an even (8) numbered carbon chains connected to unsaturated and saturated armchair edges via five membered terminal rings (ArEU5) (ArES5). (e), (f), (k) and (l) Spin densities ($\rho_{\uparrow} - \rho_{\downarrow}$) structures (a), (c), (g) and (i) respectively. Blue and red correspond to positive and negative isosurfaces of ($\rho_{\uparrow} - \rho_{\downarrow}$). (b), (d), (h) and (j) DFT transmission coefficients with antiferromagnetic spin order for structures (a), (c), (g) and (i) respectively.

Figure 5.2.17 shows spin-resolved transmissions and spin densities of symmetric ZiEU5, ZiES5, ArEU5 and ArES5 junctions, with even-numbered carbon chains

attached to saturated 5-membered terminal rings to anti-ferromagnetically aligned edges.

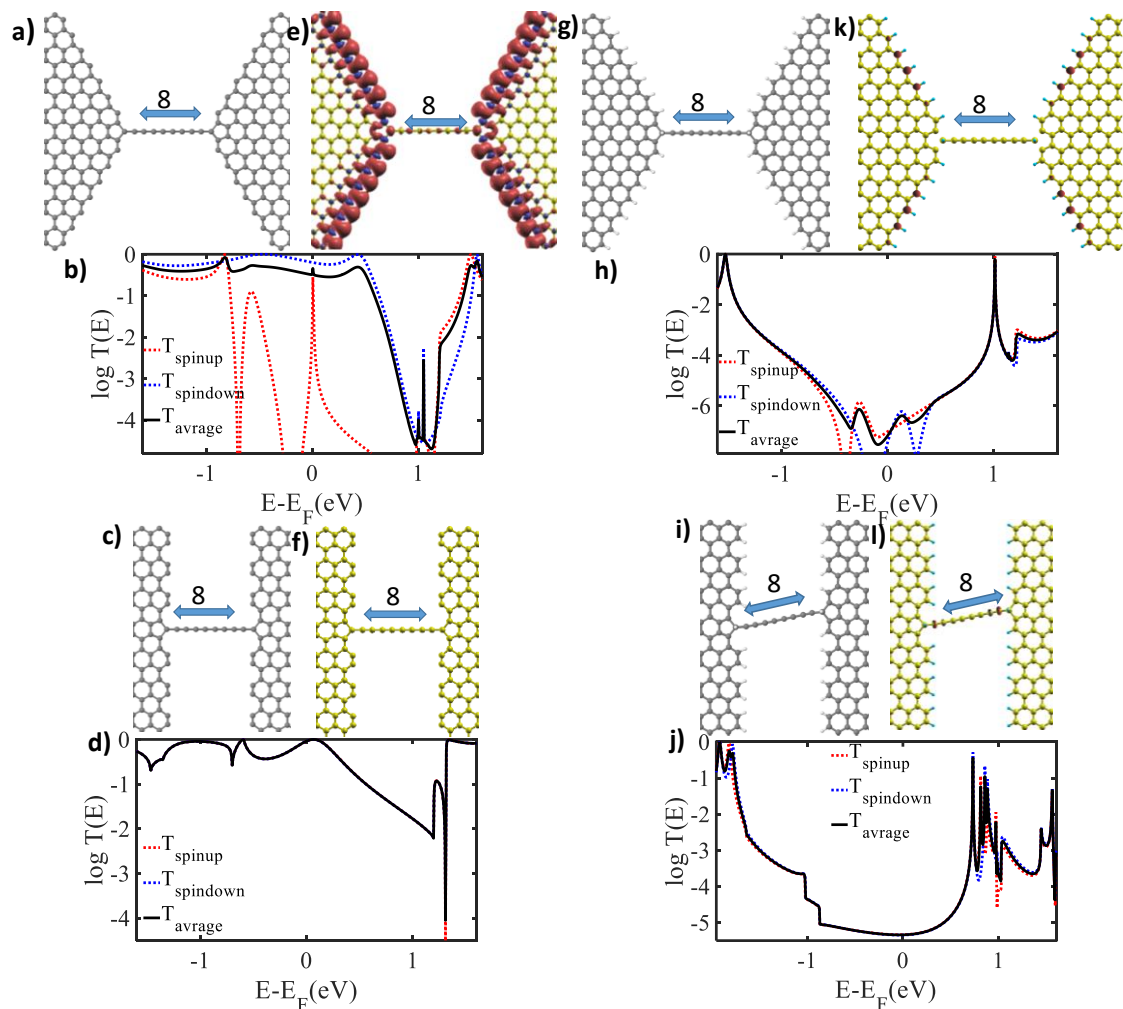


Figure 5.2.18. Schematic representation of the atomic graphene junction. (a) and (g) Relaxed atomic structure of an even (8) numbered carbon chain connected to unsaturated and saturated zigzag edges via five membered terminal rings (ZiEU5) (ZiES5). (c) and (i) Relaxed atomic structure of an even (8) numbered carbon chains connected to unsaturated and saturated armchair edges via five membered terminal rings (ArEU5) (ArES5). (e), (f), (k) and (l) Spin densities ($\rho_{\uparrow} - \rho_{\downarrow}$) structures (a), (c), (g) and (i) respectively. Blue and red correspond to positive and negative isosurfaces of ($\rho_{\uparrow} - \rho_{\downarrow}$). (b), (d), (h) and (j) DFT transmission coefficients with ferromagnetic spin order for structures (a), (c), (g) and (i) respectively.

Figure 5.2.18 shows spin-resolved transmissions and spin densities of symmetric ZiEU5, ZiES5, ArEU5 and ArES5 junctions, with even-numbered carbon chains attached to saturated 5-membered terminal rings to ferromagnetically aligned edges.

All of the above junctions are bridged by even-numbered chains. Corresponding results for junctions bridged by odd-numbered chains attached to 6-membered terminal rings, are presented in Figures (5.2.19) – (5.2.21).

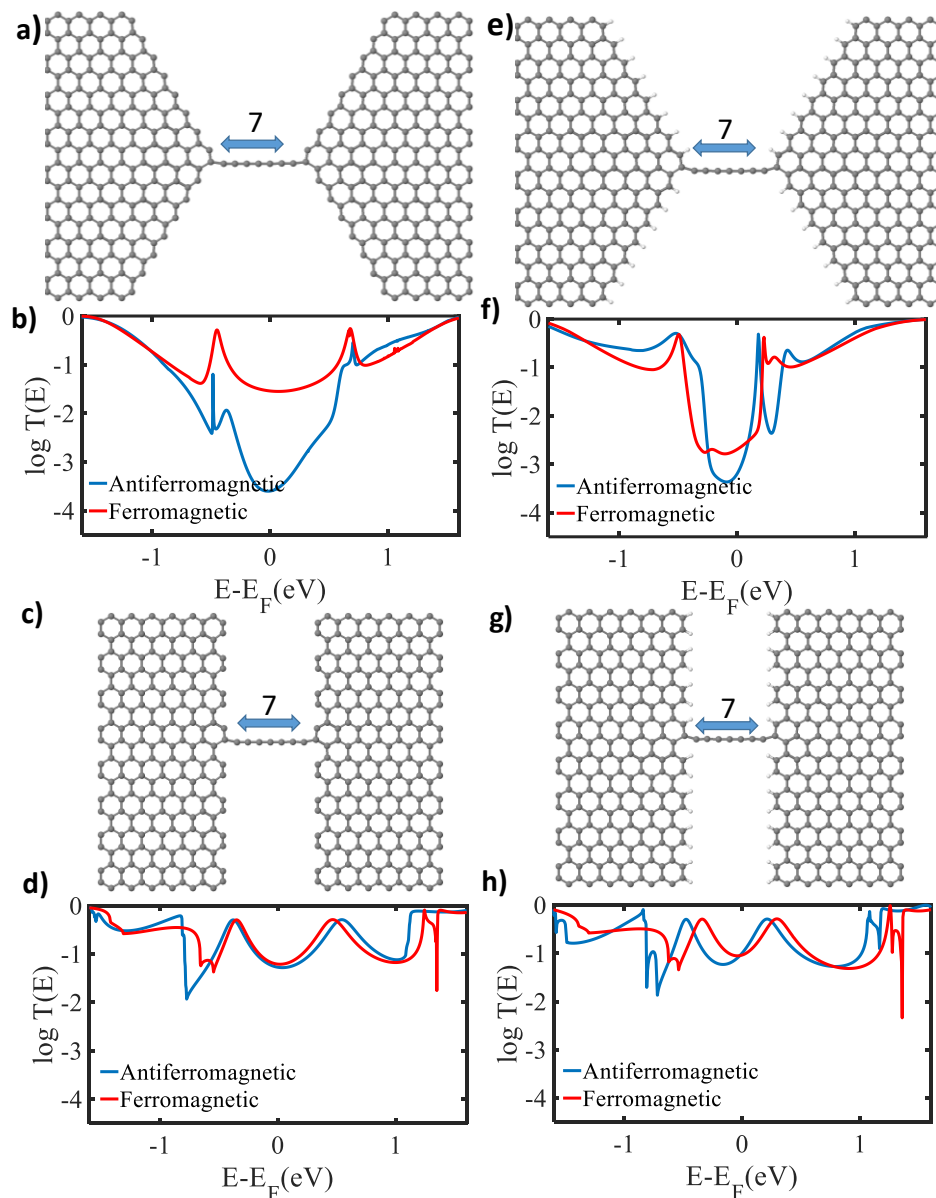


Figure 5.2.19. Schematic representation of the atomic graphene junction. (a) and (e) Relaxed atomic structure of an odd (7) numbered carbon chain connected to unsaturated and saturated zigzag edges via six membered terminal rings (ZiOU6) (ZiOS6). (c) and (g) Relaxed atomic structure of an odd (7) numbered carbon chain connected to unsaturated and saturated armchair edges via six membered terminal rings (ArOU6) (ArOS6). (b), (f), (d) and (h) DFT transmission coefficients with antiferromagnetic and ferromagnetic spin order for structures (a), (c), (e) and (g) respectively.

Figure (5.2.19) shows the comparison between total transmissions of ferromagnetic and anti-ferromagnetic edges of symmetric ZiOU6, ZiOS6, ArOU6 and ArOS6 junctions.

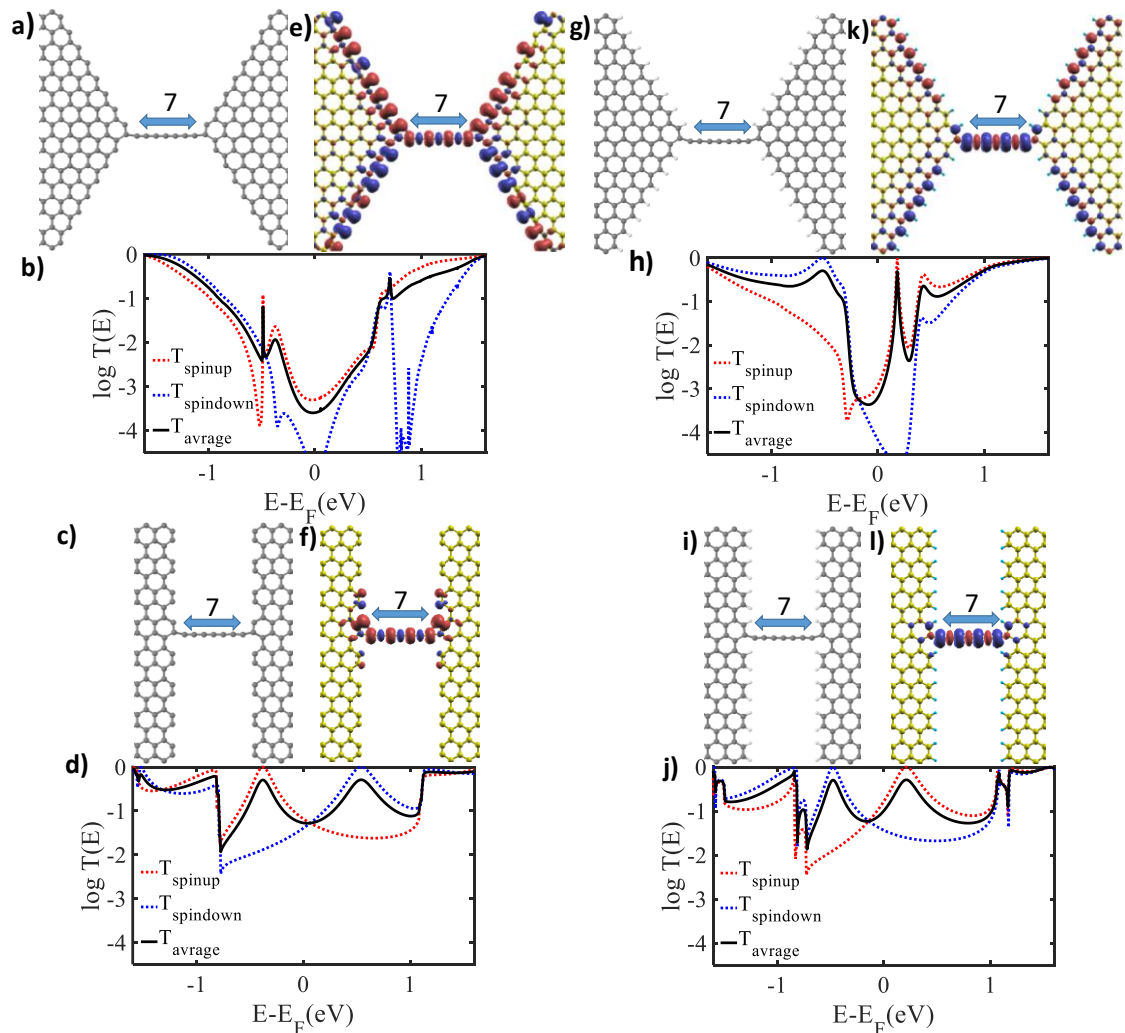


Figure 5.2.20. Schematic representation of the atomic graphene junction. (a) and (g) Relaxed atomic structure of an odd (7) numbered carbon chain connected to unsaturated and saturated zigzag edges via six membered terminal rings (ZiOU6) (ZiOS6). (c) and (i) Relaxed atomic structure of an odd (7) numbered carbon chains connected to unsaturated and saturated armchair edges via six membered terminal rings (ArOU6) (ArOS6). (e), (f), (k and l) Spin densities ($\rho_{\uparrow} - \rho_{\downarrow}$) structures (a), (c), (g) and (i) respectively. Blue and red correspond to positive and negative isosurfaces of ($\rho_{\uparrow} - \rho_{\downarrow}$). (b), (d), (h) and (j) DFT transmission coefficients with antiferromagnetic spin order for structures (a), (c), (g) and (i) respectively.

Figure (5.2.20) shows spin-resolved transmissions and spin densities of symmetric ZiOU6, ZiOS6, ArOU6 and ArOS6 junctions, with odd-numbered chains attached to anti-ferromagnetically aligned edges.

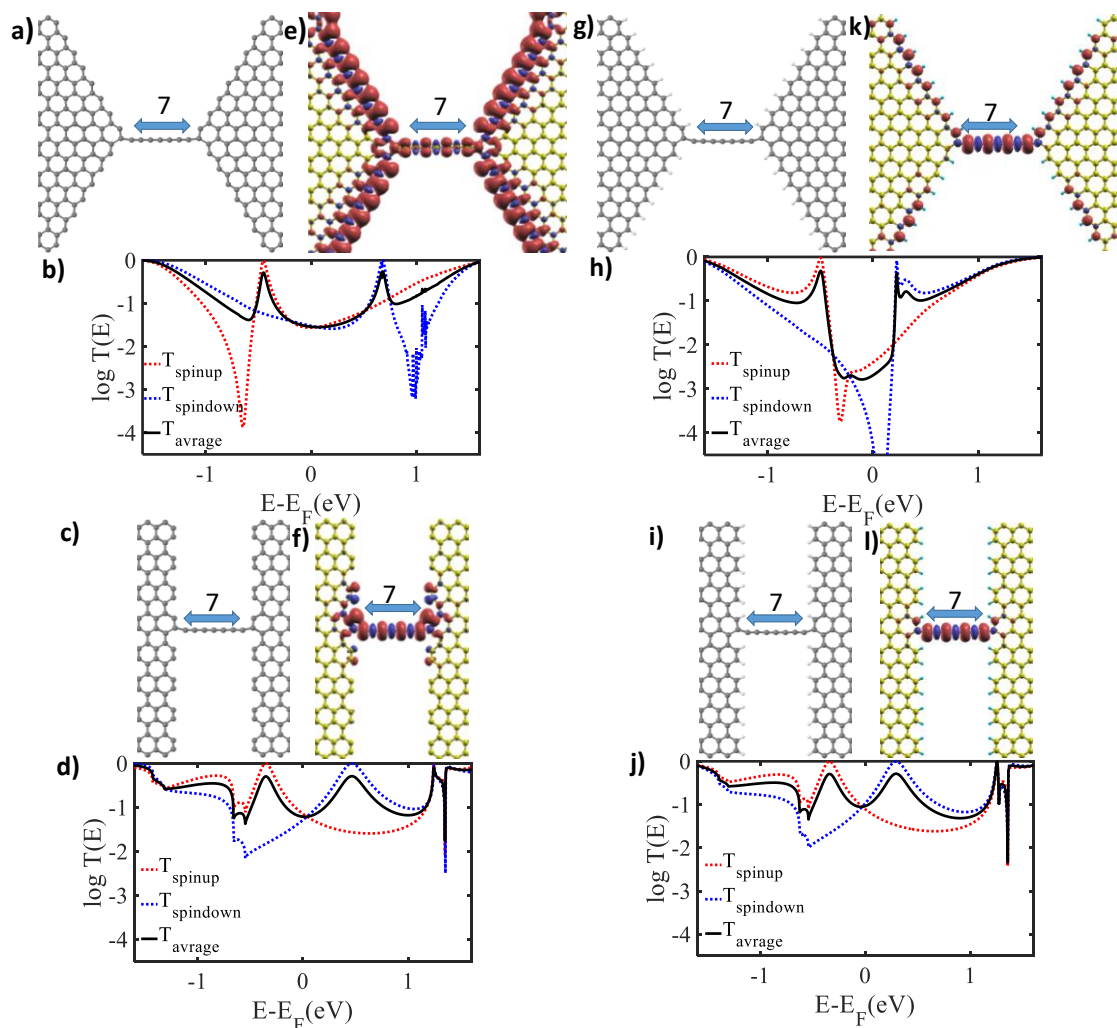


Figure 5.2.21. Schematic representation of the atomic graphene junction. (a) and (g) Relaxed atomic structure of an odd (7) numbered carbon chain connected to unsaturated and saturated zigzag edges via six membered terminal rings (ZiOU6) (ZiOS6). (c) and (i) Relaxed atomic structure of an odd (7) numbered carbon chains connected to unsaturated and saturated armchair edges via six membered terminal rings (ArOU6) (ArOS6). (e), (f), (k) and (l) Spin densities ($\rho_{\uparrow} - \rho_{\downarrow}$) structures (a), (c), (g) and (i) respectively. Blue and red correspond to positive and negative isosurfaces of ($\rho_{\uparrow} - \rho_{\downarrow}$). (b), (d), (h) and (j) DFT transmission coefficients with ferromagnetic spin order for structures (a), (c), (g) and (i) respectively.

Figure (5.2.21) shows spin-resolved transmissions and spin densities of *symmetric* ZiOU6, ZiOS6, ArOU6 and ArOS6 junctions, with odd-numbered chains attached to ferromagnetically aligned edges.

For odd-numbered carbon chains attached to unsaturated 5-membered terminal rings, Figures (5.2.22) – (5.2.24) show total and spin-resolved transmissions and spin

densities of ZiOU5, ZiOS5, ArOU6 and ArOS6 junctions, with ferromagnetically aligned or anti-ferromagnetically aligned edges

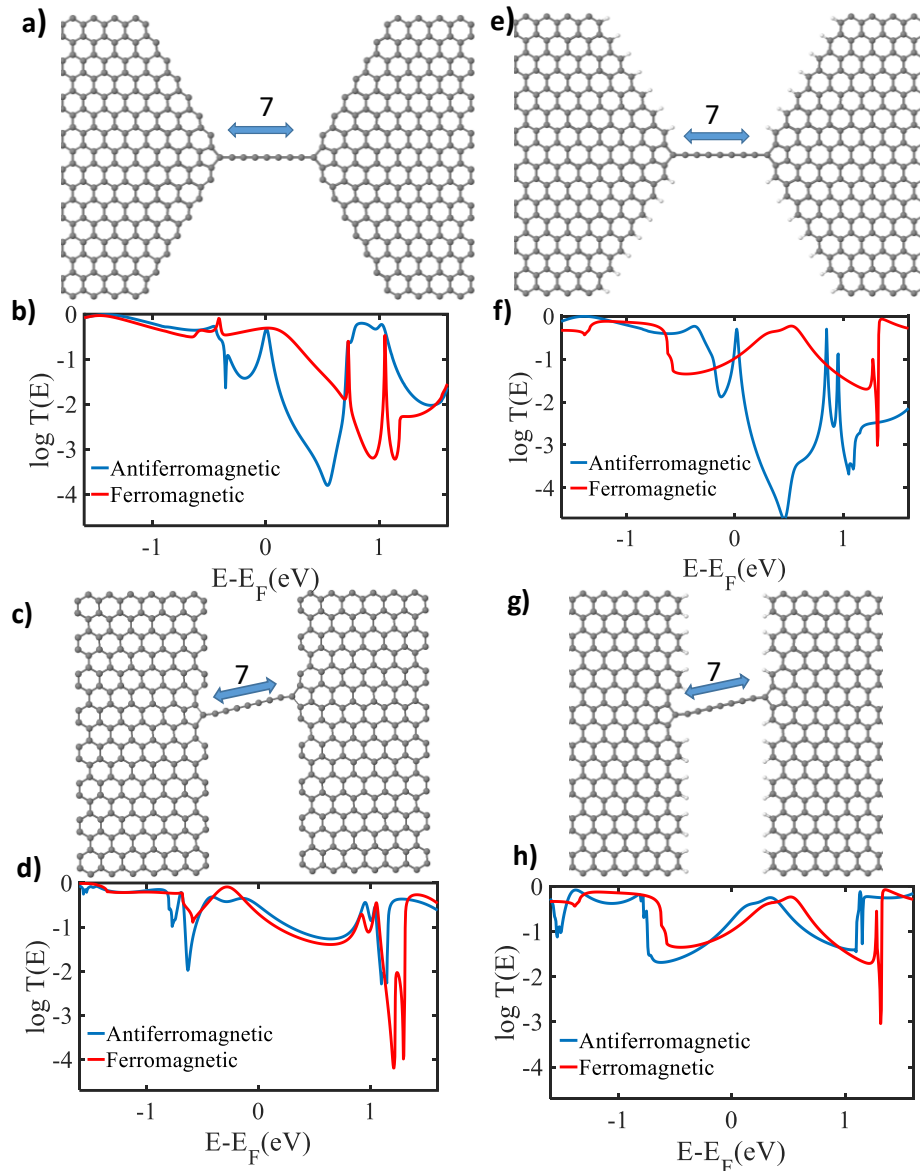


Figure 5.2.22. Schematic representation of the atomic graphene junction. (a) and (e) Relaxed atomic structure of an odd (7) numbered carbon chain connected to unsaturated and saturated zigzag edges via five membered terminal rings (ZiOU5) (ZiOS5). (c) and (g) Relaxed atomic structure of an odd (7) numbered carbon chain connected to unsaturated and saturated armchair edges via five membered terminal rings (ArOU5)(ArOS5). (b), (f), (d) and (h) DFT transmission coefficients with antiferromagnetic and ferromagnetic spin order for structures (a), (c), (e) and (g) respectively.

Figure (5.2.22) shows the comparison between total transmissions of ferromagnetic and anti-ferromagnetic edges of symmetric ZiOU5, ZiOS5, ArOU5 and ArOS5

junctions, with odd-numbered carbon chains attached to unsaturated 5-membered terminal rings

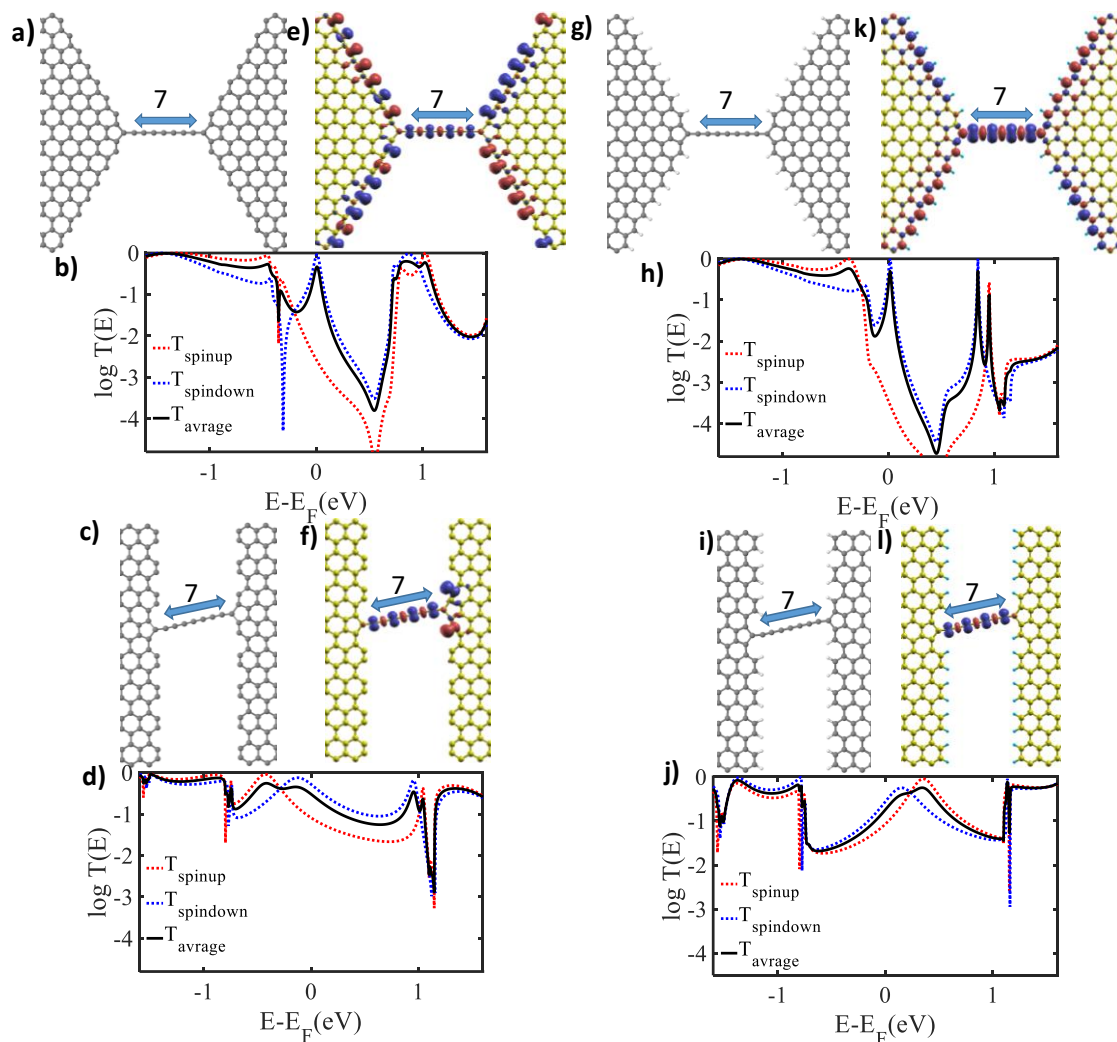


Figure 5.2.23. Schematic representation of the atomic graphene junction. (a) and (g) Relaxed atomic structure of an odd (7) numbered carbon chain connected to unsaturated and saturated zigzag edges via five membered terminal rings (ZiOU5) (ZiOS5). (c) and (i) Relaxed atomic structure of an odd (7) numbered carbon chains connected to unsaturated and saturated armchair edges via five membered terminal rings (ArOU5) (ArOS5). (e), (f), (k and l) Spin densities ($\rho_{\uparrow} - \rho_{\downarrow}$) structures (a), (c), (g) and (i) respectively. Blue and red correspond to positive and negative isosurfaces of ($\rho_{\uparrow} - \rho_{\downarrow}$). (b), (d), (h) and (j) DFT transmission coefficients with antiferromagnetic spin order for structures (a), (c), (g) and (i) respectively.

Figure 5.2.23 shows spin-resolved transmissions and spin densities of symmetric ZiOU5, ZiOS5, ArOU5 and ArOS5 junctions, with odd-numbered chains attached to unsaturated 5-membered terminal rings to anti-ferromagnetically aligned edges

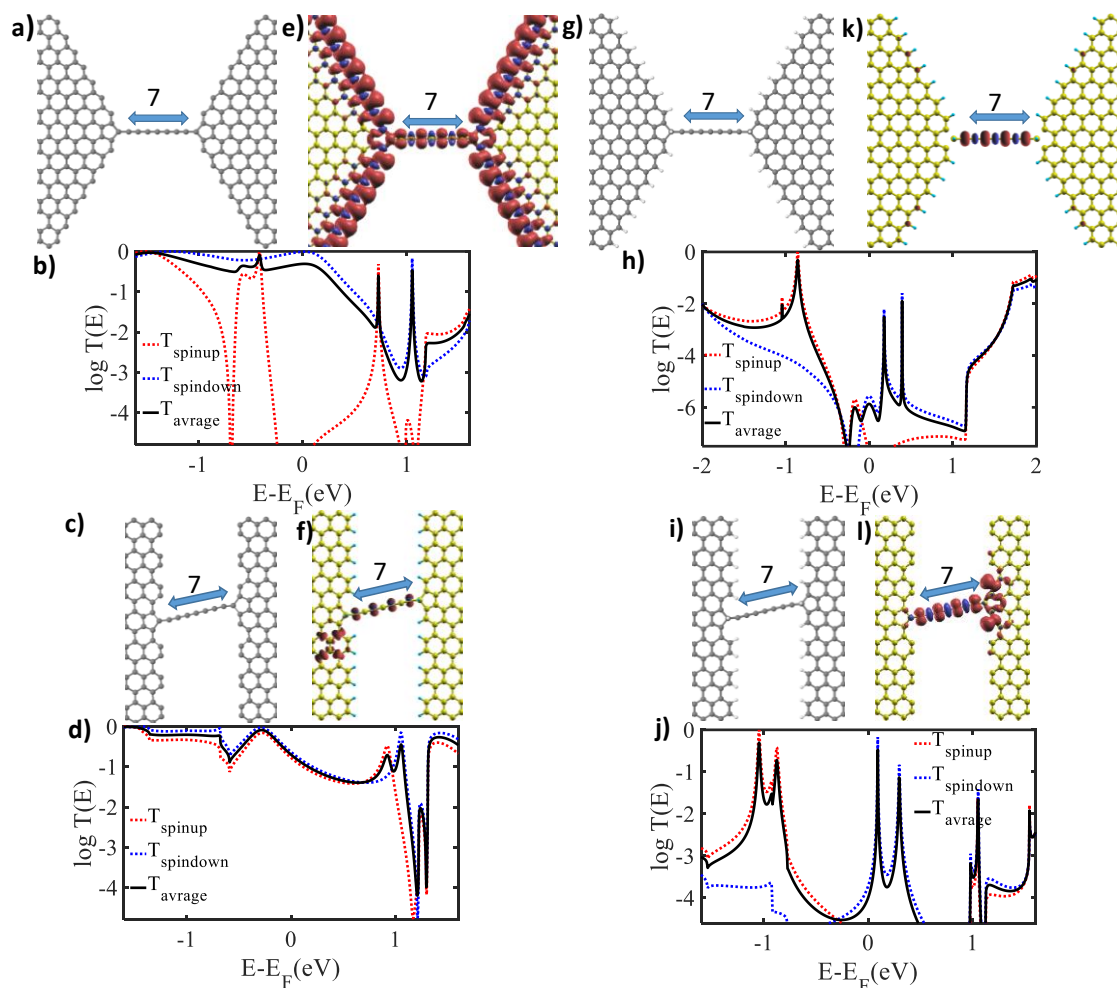


Figure 5.2.24. Schematic representation of the atomic graphene junction. (a) and (g) Relaxed atomic structure of an odd (7) numbered carbon chain connected to unsaturated and saturated zigzag edges via five membered terminal rings (ZiOU5) (ZiOS5). (c) and (i) Relaxed atomic structure of an odd (7) numbered carbon chains connected to unsaturated and saturated armchair edges via five membered terminal rings (ArOU5) (ArOS5). (e), (f), (k and l) Spin densities ($\rho_{\uparrow} - \rho_{\downarrow}$) structures (a), (c), (g) and (i) respectively. Blue and red correspond to positive and negative isosurfaces of ($\rho_{\uparrow} - \rho_{\downarrow}$). (b), (d), (h) and (j) DFT transmission coefficients with ferromagnetic spin order for structures (a), (c), (g) and (i) respectively.

Figure 5.2.24 shows spin-resolved transmissions and spin densities of symmetric ZiOU5, ZiOS5, ArOU5 and ArOS5 junctions, with odd-numbered chains attached to unsaturated 5-membered terminal rings to ferromagnetically aligned edges.

Corresponding results for odd-numbered carbon chains attached to saturated 5-membered terminal rings are shown in Figures (5.2.25) – (5.2.27). To further elucidate the electronic structures of these junctions.

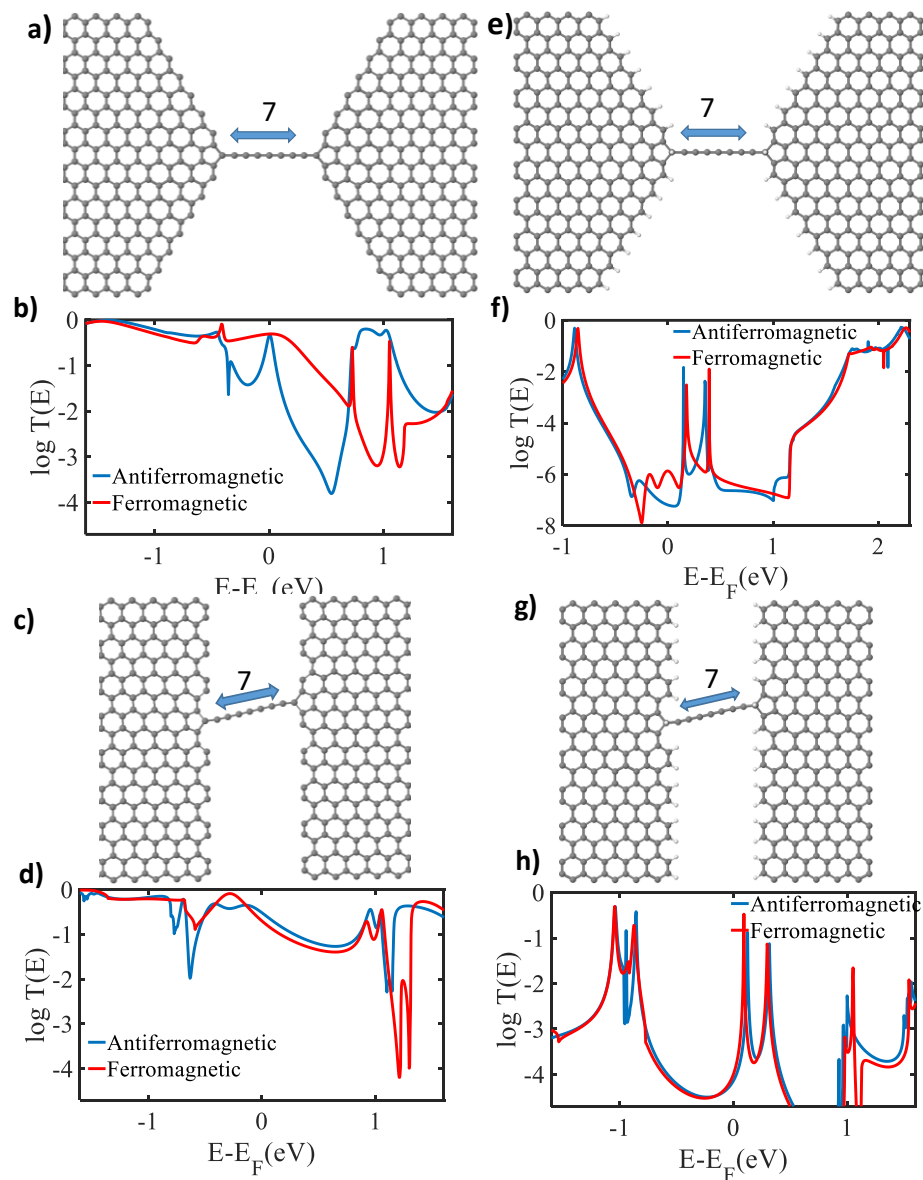


Figure 5.2.25. Schematic representation of the atomic graphene junction. (a) and (e) Relaxed atomic structure of an odd (7) numbered carbon chain connected to unsaturated and saturated zigzag edges via five membered terminal rings (ZiOU5) (ZiOS5). (c) and (g) Relaxed atomic structure of an odd (7) numbered carbon chain connected to unsaturated and saturated armchair edges via five membered terminal rings (ArOU5)(ArOS5). (b), (f), (d) and (h) DFT transmission coefficients with antiferromagnetic and ferromagnetic spin order for structures (a), (c), (e) and (g) respectively.

Figure (5.2.25) shows the comparison between total transmissions of ferromagnetic and anti-ferromagnetic edges of symmetric ZiOU5, ZiOS5 and asymmetric ArOU5 and ArOS5 junctions, with odd-numbered carbon chains attached to saturated 5-membered terminal rings.

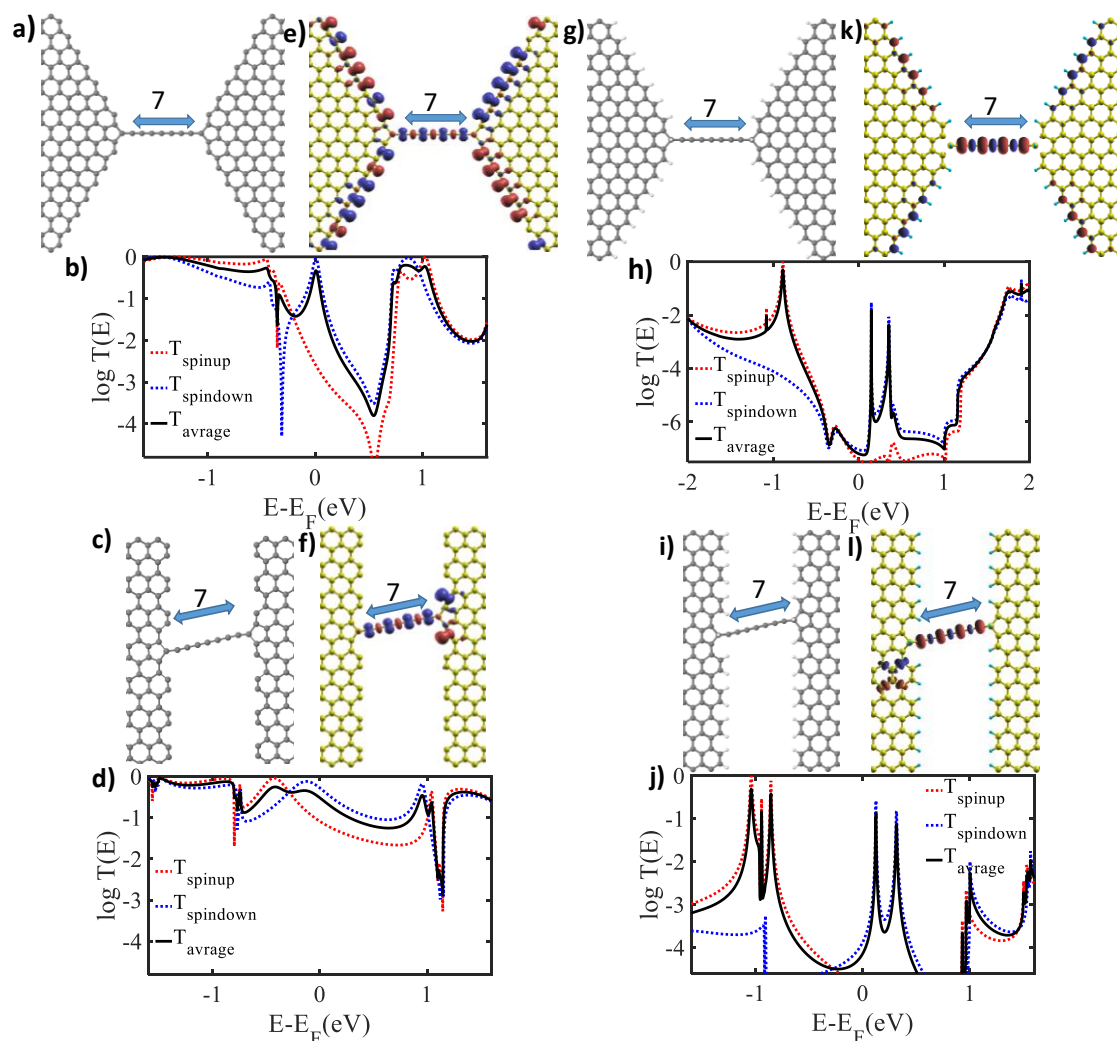


Figure 5.2.26. Schematic representation of the atomic graphene junction. (a) and (g) Relaxed atomic structure of an odd (7) numbered carbon chain connected to unsaturated and saturated zigzag edges via five membered terminal rings (ZiOU5) (ZiOS5). (c) and (i) Relaxed atomic structure of an odd (7) numbered carbon chains connected to unsaturated and saturated armchair edges via five membered terminal rings (ArOU5) (ArOS5). (e), (f), (k and l) Spin densities ($\rho_{\uparrow} - \rho_{\downarrow}$) structures (a), (c), (g) and (i) respectively. Blue and red correspond to positive and negative isosurfaces of ($\rho_{\uparrow} - \rho_{\downarrow}$). (b), (d), (h) and (j) DFT transmission coefficients with antiferromagnetic spin order for structures (a), (c), (g) and (i) respectively.

Figure 5.2.26 shows spin-resolved transmissions and spin densities of symmetric ZiOU5, ZiOS5, ArOU5 and ArOS5 junctions, with odd-numbered chains attached to saturated 5-membered terminal rings to anti-ferromagnetically aligned edges.

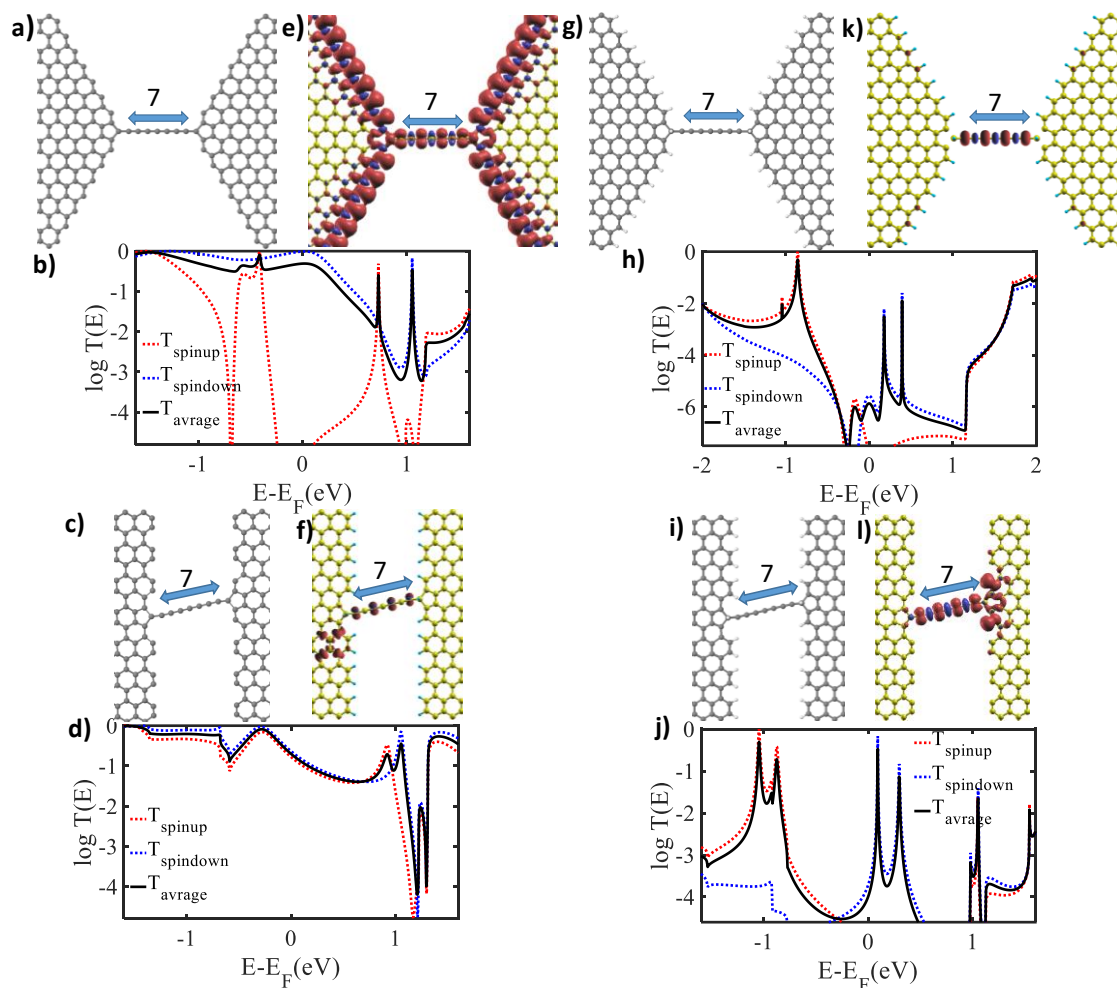


Figure 5.2.27. Schematic representation of the atomic graphene junction. (a) and (g) Relaxed atomic structure of an odd (7) numbered carbon chain connected to unsaturated and saturated zigzag edges via five membered terminal rings (ZiOU5) (ZiOS5). (c) and (i) Relaxed atomic structure of an odd (7) numbered carbon chains connected to unsaturated and saturated armchair edges via five membered terminal rings (ArOU5) (ArOS5). (e), (f), (k) and (l) Spin densities ($\rho_{\uparrow} - \rho_{\downarrow}$) structures (a), (c), (g) and (i) respectively. Blue and red correspond to positive and negative isosurfaces of ($\rho_{\uparrow} - \rho_{\downarrow}$). (b), (d), (h) and (j) DFT transmission coefficients with ferromagnetic spin order for structures (a), (c), (g) and (i) respectively.

Figure 5.2.27 shows spin-resolved transmissions and spin densities of symmetric ZiOU5, ZiOS5, ArOU5 and ArOS5 junctions, with odd-numbered chains attached to saturated 5-membered terminal rings to ferromagnetically aligned edges.

Table 5.2.1 Transport properties of graphene junctions bridged by carbon chains. The numbers show the \log_{10} of the transmission coefficient near E_F . Orange, green or blue boxes indicate large spin splitting, sharp transmission features near E_F or both, respectively.

Large spin splitting		Sharp features near E_F		Sharp features and spin splitting		
		Chain length N=8		Chain length N=7		
		edges	Unsaturated	Saturated	Unsaturated	Saturated
6 membered terminal ring	Zigzag	-4	-3.3	-3.4	-3	
	Armchair	-2.06	-2.2	-1	-1	
5 membered unsaturated terminal ring	Zigzag	-1.4	-1.5	-0.34	-0.7	
	Armchair	-0.00	-0.16	-0.5	-0.75	
5 membered saturated terminal ring	Zigzag	-1.4	-7.4	-0.34	-7.2	
	Armchair	-0.5	-5.3	-0.5	-4	

Table 5.2.1 shows a summary of the conductances of all carbon junctions with various electrode shape and termination and binding configurations. For example, the conductance of an even (8) numbered carbon chain connected to unsaturated zigzag edges via six-membered terminal ring is $10^{-4} G_0$ whereas the conductance of the same chain connected to unsaturated armchair edges, saturated zigzag edges and saturated armchair edges via six-membered terminal ring are $10^{-2.06} G_0$, $10^{-3.3} G_0$ and $10^{-2.2} G_0$, respectively. The latter is due to a large spin splitting. It is clear from this example that structures with saturated edges tend to have a lower conductance than unsaturated edges.

Also table 5.2.1 shows the conductance of an even (8) numbered carbon chain generally is high. For example, the conductance of such chain connected to unsaturated zigzag and armchair edges via unsaturated five-membered terminal ring are $10^{-1.4} G_0$ and G_0 , respectively. This is because the transmission curves have sharp features near

Chapter 5 Quantum Transport Across Graphene Nanogaps Bridged By

the Fermi energy. It is clear from this example that five- membered terminal unsaturated rings with unsaturated edges are very good conductors.

The conductance of an odd (7) numbered carbon chain connected to unsaturated zigzag and armchair edges via six-membered terminal ring are $10^{-3.4} G_0$ and $10^{-1} G_0$, respectively. In contrast, the conductance of an odd (7) numbered carbon chain connected to saturated zigzag and armchair edges via six-membered terminal ring are $10^{-3} G_0$ and $10^{-1} G_0$, respectively. Furthermore, the conductance of the same chain connected to unsaturated zigzag and armchair edges via unsaturated five-membered terminal ring are $10^{-0.34} G_0$ and $10^{-0.5} G_0$, respectively. These relatively high conductances are due to sharp features of $T(E)$ close to the Fermi energy and large spin splitting.

The above calculations show that graphene nanogaps bridged by atomic carbon chains exhibit a wide variety of transport features. Nevertheless, they can be divided into a small number of groups, with qualitatively similar transport properties, differentiated by the presence of large spin splitting and/or sharp transmission features near the Fermi energy. Which for the junctions studied, are summarized in Table 5.2.1.

Generally, I find that

- Zigzag edges tend to lower the conductance compared with armchair edges (Figure 5.2.1.), where it is clear to see that the $\log T(E)$ in 6 membered terminal ring
- Ferromagnetically aligned edges have a higher transmission than anti-Ferromagnetically aligned edges, because ferromagnetic alignment tends to increase the transmission of one of the spins (Figure 5.2.7.).
- Saturated edges tend to have a lower conductance than unsaturated edges.

Chapter 5 **Quantum Transport Across Graphene Nanogaps Bridged By**

- Five-membered saturated terminal rings with saturated edges are the worst conductors
- Five- membered terminal rings (saturated or unsaturated) with unsaturated edges are the best conductors

In addition to the above features, I find that

- Junctions with even numbered chains of carbon atoms tend to have a lower conductance than those with odd atom numbered chains. (Figure 5.2.3)
- Junctions with six-membered terminal rings and unsaturated edges tend to have a lower conductance than those with five-membered terminal rings and unsaturated edges. (Figure 5.2.11.) and (Figure 5.2.14))
- Junctions with five-membered saturated terminal rings with saturated edges tend to have a lower conductance than those with unsaturated edges. (Figure 5.2.21).

These qualitative trends form a useful categorisation, which allow us to rationalise the behaviour of graphene nanogaps, bridged by atomic carbon chains.

In this section I calculated widths Γ of HOMO and LUMO resonances from the transmission coefficient $T(E)$. The transmission for electrons of energy E (passing from the source to the drain) is calculated via the relation $T(E) = \text{Trace}(\Gamma_R(E)G^R(E)\Gamma_L(E)G^{R\dagger}(E))$. In this expression, $\Gamma_{R,L}(E) = i(\Sigma_{R,L}(E) - \Sigma_{R,L}^\dagger(E))$ describe the level broadening due to the coupling between left (L) and right (R) electrodes and the central scattering region, ($\Sigma_{R,L}(E)$ are the retarded self-energies associated with this coupling, the transmission could be calculated by Lorentzian formula.

$$T = \frac{4\Gamma_1\Gamma_2}{(E - \varepsilon)^2 + (\Gamma_1 + \Gamma_2)^2}$$

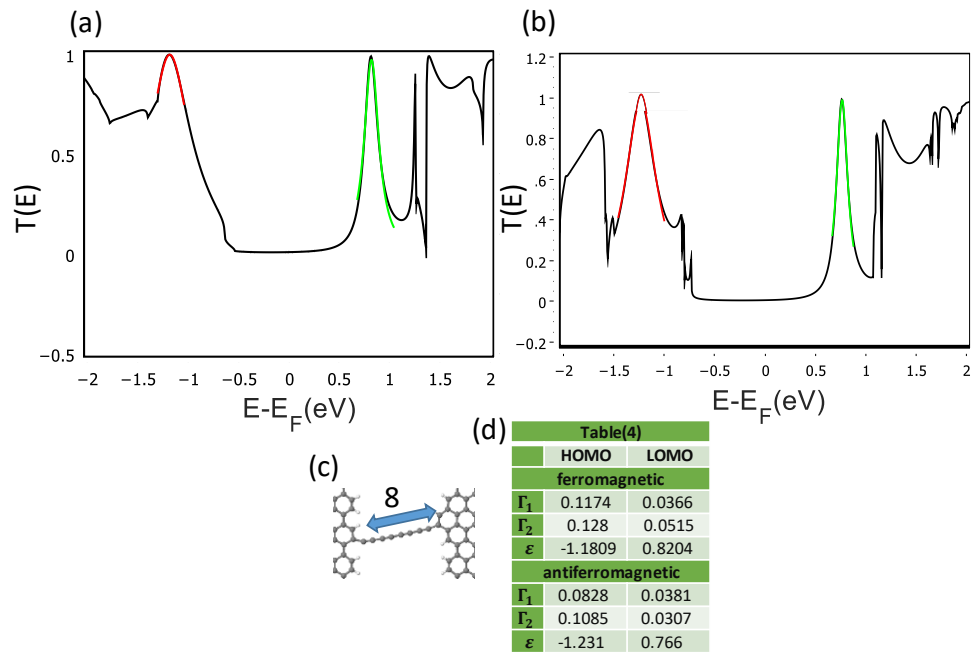


Figure 5.2.28. (a) Transmission coefficients with antiferromagnetic spin order for structures (c). (b) Transmission coefficients with ferromagnetic spin order for structures (c). (d) The values obtained for Γ_1 , Γ_2 and ϵ by fitting HOMO and LUMO resonances for structure (c)

Figure 5.2.28a,b shows transmission coefficients as function of energy for structure shown in Figure 5.2.28c. The red (green) line shows HOMO (LUMO) resonances fitting using above equation for antiferromagnetic and ferromagnetic spin orders and the values of ϵ , Γ_1 , Γ_2 (Fig. 5.2.28d).

The table below shows the value of Γ_1 , Γ_2 and ϵ in the unit of electron volt (eV) for most of the structures.

Table 5.2.2. Gammas energies (eV) for HOMO and LUMO with antiferromagnetic and ferromagnetic spin order

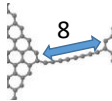
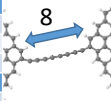
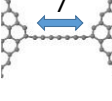
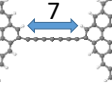
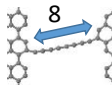
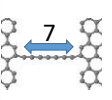
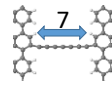
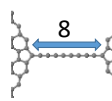
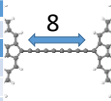
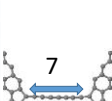
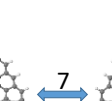
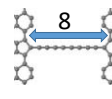
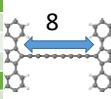
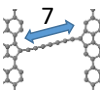
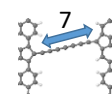
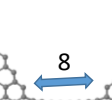
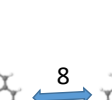
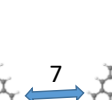
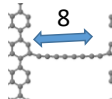
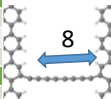
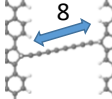
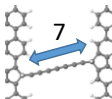
	Table(1) HOMO LUMO ferromagnetic Γ_1 0.0465 0.031 Γ_2 0.0718 0.059 ϵ -0.965 1.015 antiferromagnetic Γ_1 0.1760 0.234 Γ_2 0.0728 0.041 ϵ -0.968 0.892		Table(2) HOMO LUMO ferromagnetic Γ_1 0.1200 0.1305 Γ_2 0.1562 0.1646 ϵ -1.188 0.659 antiferromagnetic Γ_1 0.1399 0.1522 Γ_2 0.1727 0.1898 ϵ -1.1963 0.7471		Table(13) HOMO LUMO ferromagnetic Γ_1 0.005 0.032 Γ_2 0.0321 0.005 ϵ -0.448 0.676 antiferromagnetic Γ_1 -3.0522 -0.0125 Γ_2 -0.001 -0.0010 ϵ -0.485 0.7017		Table(14) HOMO LUMO ferromagnetic Γ_1 0.140 0.0020 Γ_2 0.036 0.035 ϵ -0.319 0.891 antiferromagnetic Γ_1 -0.177 -0.059 Γ_2 -0.031 -0.006 ϵ -0.230 0.846
	Table(3) HOMO LUMO ferromagnetic Γ_1 0.1421 0.1231 Γ_2 0.2171 0.02158 ϵ -1.009 0.891 antiferromagnetic Γ_1 0.0178 0.0699 Γ_2 0.006 0.0265 ϵ -0.755 0.952		Table(4) HOMO LUMO ferromagnetic Γ_1 0.1174 0.0366 Γ_2 0.128 0.0515 ϵ -1.1809 0.8204 antiferromagnetic Γ_1 0.0828 0.0381 Γ_2 0.1085 0.0307 ϵ -1.231 0.766		Table(15) HOMO LUMO ferromagnetic Γ_1 0.0119 0.0194 Γ_2 0.068 0.1106 ϵ -0.348 0.468 antiferromagnetic Γ_1 0.0125 0.0199 Γ_2 0.0721 0.113 ϵ -0.377 0.545		Table(16) HOMO LUMO ferromagnetic Γ_1 0.0722 0.0986 Γ_2 0.1326 0.0175 ϵ -0.336 0.295 antiferromagnetic Γ_1 0.010 0.0939 Γ_2 0.0581 0.0165 ϵ -0.4728 0.2150
	Table(5) HOMO LUMO ferromagnetic Γ_1 0.0563 0.1433 Γ_2 0.3029 0.0227 ϵ -0.497 0.4045 antiferromagnetic Γ_1 0.160 0.0066 Γ_2 0.1605 0.0072 ϵ -0.7096 0.0780		Table(6) HOMO LUMO ferromagnetic Γ_1 0.162 0.0006 Γ_2 0.101 0.0038 ϵ -0.759 0.0234 antiferromagnetic Γ_1 0.1971 0.0035 Γ_2 0.1385 0.0017 ϵ -0.798 0.067		Table(17) HOMO LUMO ferromagnetic Γ_1 0.1043 0.0268 Γ_2 0.0192 0.0041 ϵ -0.4803 -0.0056 antiferromagnetic Γ_1 0.0201 0.3280 Γ_2 0.0073 0.0543 ϵ -0.414 -0.007		Table(18) HOMO LUMO ferromagnetic Γ_1 0.3794 0.0379 Γ_2 0.1326 0.01925 ϵ -1.048 0.465 antiferromagnetic Γ_1 0.0232 0.0116 Γ_2 0.1108 0.0019 ϵ -0.381 0.0174
	Table(7) HOMO LUMO ferromagnetic Γ_1 0.0279 0.1153 Γ_2 0.0396 0.1029 ϵ -0.607 0.0586 antiferromagnetic Γ_1 0.0223 0.114 Γ_2 0.0222 0.103 ϵ -0.673 -0.0100		Table(8) HOMO LUMO ferromagnetic Γ_1 0.1200 0.1547 Γ_2 0.0816 0.119 ϵ -0.075 1.304 antiferromagnetic Γ_1 0.0803 0.0531 Γ_2 0.0900 0.0442 ϵ -0.111 1.203		Table(19) HOMO LUMO ferromagnetic Γ_1 -0.043 -0.0021 Γ_2 -0.109 -0.0412 ϵ -0.2799 0.9192 antiferromagnetic Γ_1 -0.0331 -0.037 Γ_2 -0.221 -0.003 ϵ -0.152 0.952		Table(20) HOMO LUMO ferromagnetic Γ_1 -0.1398 -0.0396 Γ_2 -0.4090 -0.2033 ϵ -1.038 0.4723 antiferromagnetic Γ_1 0.0883 0.0363 Γ_2 0.0213 0.1934 ϵ -0.840 0.3020
	Table(9) HOMO LUMO ferromagnetic Γ_1 0.066 0.0228 Γ_2 0.1399 0.0439 ϵ -1.010 1.001 antiferromagnetic Γ_1 0.2003 0.2146 Γ_2 0.1144 0.0889 ϵ -0.930 0.932		Table(10) HOMO LUMO ferromagnetic Γ_1 0.1583 0.1126 Γ_2 0.1464 0.1255 ϵ -1.209 0.6633 antiferromagnetic Γ_1 0.1446 0.1131 Γ_2 0.1588 0.1392 ϵ -1.175 0.7071		Table(21) HOMO LUMO ferromagnetic Γ_1 0.0074 0.0005 Γ_2 0.0067 0.0005 ϵ -1.525 1.011 antiferromagnetic Γ_1 0.0066 0.0010 Γ_2 0.0074 0.0003 ϵ -1.522 1.0147		Table(22) HOMO LUMO ferromagnetic Γ_1 -0.0071 -0.0003 Γ_2 -0.0012 -0.0026 ϵ -0.857 0.157 antiferromagnetic Γ_1 -0.0012 -0.0655 Γ_2 -0.0072 -0.0644 ϵ -0.887 0.647
	Table(11) HOMO LUMO ferromagnetic Γ_1 0.1366 0.0305 Γ_2 0.2248 0.0793 ϵ -1.047 0.9550 antiferromagnetic Γ_1 0.00724 0.04361 Γ_2 0.0034 0.0335 ϵ -0.7222 0.9448		Table(12) HOMO LUMO ferromagnetic Γ_1 0.1307 0.0471 Γ_2 0.0880 0.0383 ϵ -1.229 0.80204 antiferromagnetic Γ_1 -0.0334 -0.0497 Γ_2 -0.0084 -0.0381 ϵ -0.8205 0.738		Table(23) HOMO LUMO ferromagnetic Γ_1 -0.0347 -0.0001 Γ_2 -0.0059 -0.0009 ϵ -1.803 0.731 antiferromagnetic Γ_1 0.0037 0.0029 Γ_2 0.0047 0.0080 ϵ -1.659 1.012		Table(24) HOMO LUMO ferromagnetic Γ_1 -0.0006 -0.0001 Γ_2 -0.0114 -0.0011 ϵ -0.8746 0.0915 antiferromagnetic Γ_1 0.0037 -0.0686 Γ_2 0.0005 -0.0686 ϵ -0.8573 0.749

Table 5.2.3. Total energy differences between antiferromagnetically aligned and ferromagnetically aligned edges.

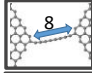
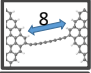
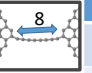
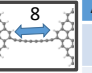
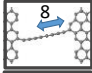
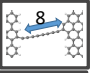
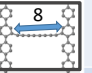
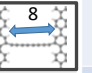
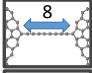
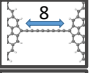
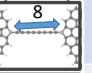
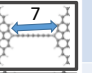
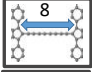
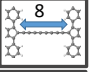
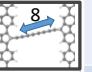
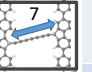
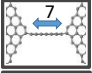
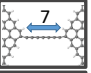
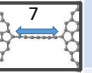
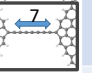
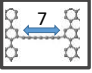
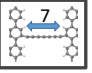
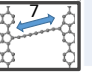
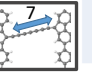




	ΔE (eV)		ΔE (eV)		ΔE (eV)		ΔE (eV)
	-1.88		-9.11		-2.91		-1.88
	-2.92		-14.73		-3.17		-2.92
	-2.94		-9.46		-2.71		-2.94
	-2.8		-16.6		-0.81		-2.8
	-0.12		-9.85		-3.63		-9.7
	-2.9		-14.87		-2.74		-15.15

Table 5.2.3 shows the energy differences between antiferromagnetic and ferromagnetic spin orders. In all junctions, antiferromagnetic spin configuration has lower energy. For example, the total energy of relaxed atomic structure of an even (8) numbered carbon chain connected to unsaturated zigzag edges via six membered terminal rings with antiferromagnetic spin order is -1.88 eV lower than the total energy of the same structure with ferromagnetic spin order.

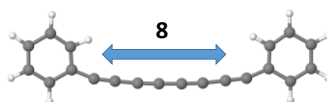
Below, I show wave functions of HOMO-4, HOMO-3, HOMO-2, HOMO-1, HOMO, LUMO, LUMO+1, LUMO+2, LUMO+3 and LUMO+4 levels for relaxed atomic structure of most carbon filaments.

Table 5.2.4. The wave functions of HOMO-4, HOMO-3, HOMO-2, HOMO-1, HOMO, LUMO, LUMO+1, LUMO+2, LUMO+3 and LUMO+4 levels orbitals for relaxed atomic structure of an even (8) numbered carbon chain connected to unsaturated six membered terminal rings .



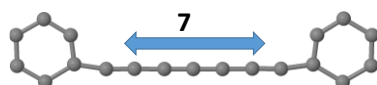
$E_f = -5.09$ (eV)	E (eV)	Spin up	E (eV)	Spin down
LUMO+4	-3.40		-3.40	
LUMO+3	-3.59		-3.59	
LUMO+2	-4.28		-4.28	
LUMO+1	-4.44		-4.44	
LUMO	-4.78		-4.78	
HOMO	-5.4		-5.4	
HOMO-1	-5.73		-5.73	
HOMO-2	-6.11		-6.11	
HOMO-3	-6.13		-6.13	
HOMO+4	-6.26		-6.26	

Table 5.2.5. The wave functions of HOMO-4, HOMO-3, HOMO-2, HOMO-1, HOMO, LUMO, LUMO+1, LUMO+2, LUMO+3 and LUMO+4 levels orbitals for relaxed atomic structure of an even (8) numbered carbon chain connected to saturated six membered terminal rings .



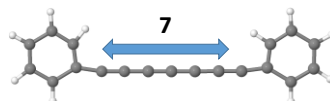
$E_f = -4.04$ (eV)	E (eV)	Spin up	E (eV)	Spin down
LUMO+4	-1.17		-1.17	
LUMO+3	-1.36		-1.36	
LUMO+2	-1.90		-1.90	
LUMO+1	-2.61		-2.61	
LUMO	-2.90		-2.90	
HOMO	-4.86		-4.86	
HOMO-1	-5.20		-5.20	
HOMO-2	-5.80		-5.80	
HOMO-3	-6.08		-6.08	
LUMO+4	-6.20		-6.20	

Table 5.2.6. The wave functions of HOMO-4, HOMO-3, HOMO-2, HOMO-1, HOMO, LUMO, LUMO+1, LUMO+2, LUMO+3 and LUMO+4 levels orbitals for relaxed atomic structure of an odd (7) numbered carbon chain connected to unsaturated six membered terminal ring



$E_f = -5.28$ (eV)	E (eV)	Spin up	E (eV)	Spin down
LUMO+4	-3.25		-3.18	
LUMO+3	-4.09		-4.32	
LUMO+2	-4.16		-4.40	
LUMO+1	-4.98		-5.05	
LUMO	-5.12		-5.18	
HOMO	-5.67		-5.38	
HOMO-1	-5.81		-5.57	
HOMO-2	-5.98		-5.74	
HOMO-3	-5.98		-5.91	
HOMO+4	-6.11		-6.06	

Table 5.2.7. The wave functions of HOMO-4, HOMO-3, HOMO-2, HOMO-1, HOMO, LUMO, LUMO+1, LUMO+2, LUMO+3 and LUMO+4 levels orbitals for Relaxed atomic structure of an odd (7) numbered carbon chain connected to saturated six membered terminal rings .



$E_f = -3.88$ (eV)	E (eV)	Spin up	E (eV)	Spin down
LUMO+4	-1.19		-1.05	
LUMO+3	-1.59		-1.30	
LUMO+2	-2.32		-1.43	
LUMO+1	-3.19		-1.78	
LUMO	-3.44		-2.42	
HOMO	-5.37		-4.33	
HOMO-1	-5.77		-4.44	
HOMO-2	-5.77		-5.46	
HOMO-3	-5.91		-5.88	
HOMO+4	-6.41		-6.01	

Table 5.2.8. The wave functions of HOMO-4, HOMO-3, HOMO-2, HOMO-1, HOMO, LUMO, LUMO+1, LUMO+2, LUMO+3 and LUMO+4 levels orbitals for relaxed atomic structure of an odd (7) numbered carbon chain connected to unsaturated five membered terminal rings.

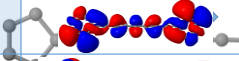
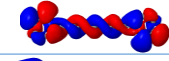
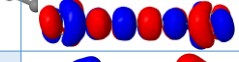
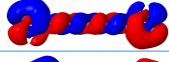
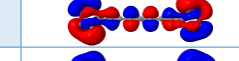
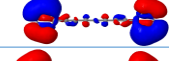
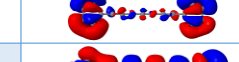
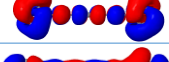
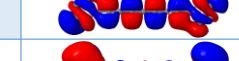
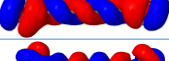
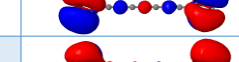
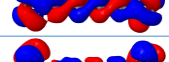
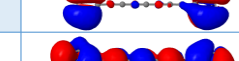
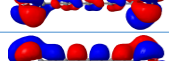
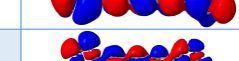
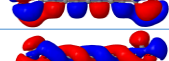
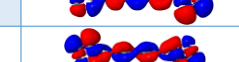



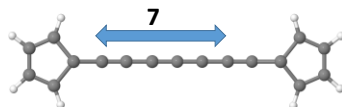
$E_f = -5.14$ (eV)	E (eV)	Spin up	E (eV)	Spin down
LUMO+4	-3.57		-3.85	
LUMO+3	-4.23		-4.12	
LUMO+2	-4.26		-4.31	
LUMO+1	-4.31		-4.35	
LUMO	-4.96		-4.56	
HOMO	-5.33		-5.41	
HOMO-1	-5.37		-5.43	
HOMO-2	-5.48		-5.77	
HOMO-3	-6.06		-5.94	
HOMO+4	-6.25		-6.06	

Table 5.2.9. The wave functions of HOMO-4, HOMO-3, HOMO-2, HOMO-1, HOMO, LUMO, LUMO+1, LUMO+2, LUMO+3 and LUMO+4 levels orbitals for relaxed atomic structure of an odd (7) numbered carbon chain connected to unsaturated five membered terminal rings .



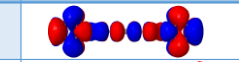
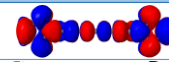
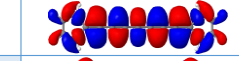
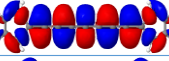
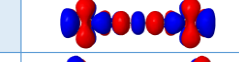
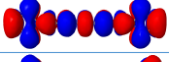
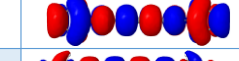
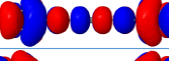
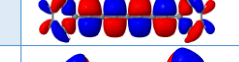
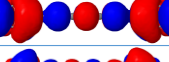
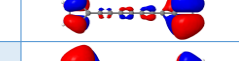
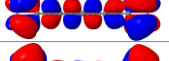
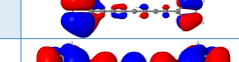
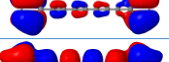
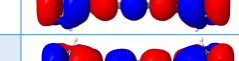
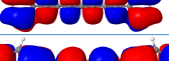
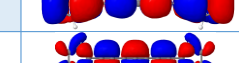
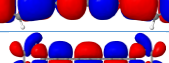

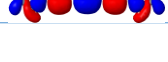
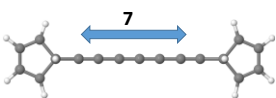
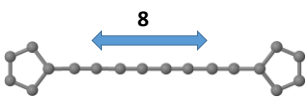
$E_f = -4.62$ (eV)	E (eV)	Spin up	E (eV)	Spin down
LUMO+4	-0.79		-1.11	
LUMO+3	-1.86		-1.55	
LUMO+2	-1.87		-1.91	
LUMO+1	-3.74		-3.63	
LUMO	-4.48		-3.78	
HOMO	-4.75		-4.85	
HOMO-1	-4.83		-4.88	
HOMO-2	-4.99		-5.32	
HOMO-3	-5.71		-5.96	
HOMO+4	-6.50		-6.34	

Table 5.2.10. The wave functions of HOMO-4, HOMO-3, HOMO-2, HOMO-1, HOMO, LUMO, LUMO+1, LUMO+2, LUMO+3 and LUMO+4 levels orbitals for relaxed atomic structure of an odd (7) numbered carbon chain connected to saturated five membered terminal rings.



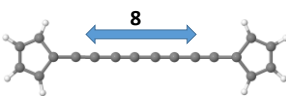
$E_f = -3.79$ (eV)	E (eV)	Spin up	E (eV)	Spin down
LUMO+4	-1.12		0.65	
LUMO+3	-2.03		-1.17	
LUMO+2	-2.10		-1.42	
LUMO+1	-3.11		-2.09	
LUMO	-3.23		-2.15	
HOMO	-4.98		-4.34	
HOMO-1	-5.01		-4.44	
HOMO-2	-5.71		-5.01	
HOMO-3	-5.82		-5.05	
HOMO+4	-6.94		-5.96	

Table 5.2.11. The wave functions of HOMO-4, HOMO-3, HOMO-2, HOMO-1, HOMO, LUMO, LUMO+1, LUMO+2, LUMO+3 and LUMO+4 levels orbitals for relaxed atomic structure of an even (8) numbered carbon chain connected to unsaturated five membered terminal rings.



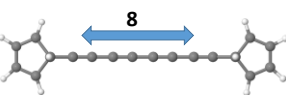
$E_f = -4.99$ (eV)	E (eV)	Spin up	E (eV)	Spin down
LUMO+4	-3.43		-3.35	
LUMO+3	-3.59		-3.54	
LUMO+2	-4.18		-4.11	
LUMO+1	-4.27		-4.29	
LUMO	-4.79		-4.77	
HOMO	-5.23		-5.18	
HOMO-1	-5.46		-5.44	
HOMO-2	-5.77		-5.87	
HOMO-3	-5.89		-5.97	
HOMO+4	-6.26		-6.34	

Table 5.2.12. The wave functions of HOMO-4, HOMO-3, HOMO-2, HOMO-1, HOMO, LUMO, LUMO+1, LUMO+2, LUMO+3 and LUMO+4 levels orbitals for Relaxed atomic structure of an even (8) numbered carbon chain connected to saturated five membered terminal rings.



$E_f = -4.62$ (eV)	E (eV)	Spin up	E (eV)	Spin down
LUMO+4	-0.75		-0.75	
LUMO+3	-1.37		-1.37	
LUMO+2	-2.70		-2.70	
LUMO+1	-2.91		-2.91	
LUMO	-4.43		-4.43	
HOMO	-4.82		-4.81	
HOMO-1	-4.87		-4.88	
HOMO-2	-5.39		-5.38	
HOMO-3	-5.67		-5.67	
HOMO+4	-6.47		-6.47	

Table 5.2.13. The wave functions of HOMO-4, HOMO-3, HOMO-2, HOMO-1, HOMO, LUMO, LUMO+1, LUMO+2, LUMO+3 and LUMO+4 levels orbitals for Relaxed atomic structure of an even (8) numbered carbon chain connected to saturated five membered terminal rings.



$E_f = -4.09$ (eV)	E (eV)	Spin up	E (eV)	Spin down
LUMO+4	-0.32		-0.32	
LUMO+3	-1.99		-1.99	
LUMO+2	-2.07		-2.07	
LUMO+1	-2.41		-2.41	
LUMO	-2.43		-2.43	
HOMO	-4.94		-4.94	
HOMO-1	-5.03		-5.03	
HOMO-2	-5.06		-5.06	
HOMO-3	-5.24		-5.24	
HOMO+4	-6.38		-6.38	

Chapter 5 Quantum Transport Across Graphene Nanogaps Bridged By

In summary, as a step towards realising the technological potential of electroburnt graphene junctions, I have investigated how their electronic and spintronic properties are controlled by edge terminations and by the carbon chains bridging their gaps. Such junctions are of particular interest, because of the stable covalent bonding of atomic carbon bridges to the electrodes. One can conceive of an infinite number of combinations of edges and chains in such graphene-based junctions and in the present study, I have presented results for a selection of these. Although a wide range of transport properties are possible, I find that junctions can be divided into a small number of categories, according to their qualitative transport properties.

References

- [1] Novoselov, K. S., Geim, A. K., Morozov, S. V., Jiang, D., Zhang, Y., Dubonos, S. V., ... & Firsov, A. A. (2004). Electric field effect in atomically thin carbon films. *science*, 306(5696), 666-669.
- [2] Geim, A. K., & Novoselov, K. S. (2010). The rise of graphene. In *Nanoscience and technology: a collection of reviews from nature journals* (pp. 11-19).
- [3] Nair, R. R., Blake, P., Grigorenko, A. N., Novoselov, K. S., Booth, T. J., Stauber, T., ... & Geim, A. K. (2008). Fine structure constant defines visual transparency of graphene. *Science*, 320(5881), 1308-1308.
- [4] Wang, F., Zhang, Y., Tian, C., Girit, C., Zettl, A., Crommie, M., & Shen, Y. R. (2008). Gate-variable optical transitions in graphene. *science*, 320(5873), 206-209.
- [5] Frank, I. W., Tanenbaum, D. M., van der Zande, A. M. & McEuen, P. L. Mechanical properties of suspended graphene sheets. *J. Vac. Sci. & Technol. B* 25, 2558–2561 (2007).
- [6] Lee, C., Wei, X., Kysar, J. W., & Hone, J. (2008). Measurement of the elastic properties and intrinsic strength of monolayer graphene. *science*, 321(5887), 385-388.
- [7] Balandin, A. A. et al. Superior thermal conductivity of single-layer graphene. *Nano Lett.* 8, 902–907 (2008).
- [8] Balandin, A. A. (2011). Thermal properties of graphene and nanostructured carbon materials. *Nature materials*, 10(8), 569-581..

- [9] van der Molen, S. J., Liao, J., Kudernac, T., Agustsson, J. S., Bernard, L., Calame, M., ... & Schönenberger, C. (2009). Light-controlled conductance switching of ordered metal– molecule– metal devices. *Nano letters*, 9(1), 76-80. R. R. Tykwinski, *Chem. Rec.* 2015, 15, 1060–1074.
- [10] Lörtscher, E., Cizek, J. W., Tour, J., & Riel, H. (2006). Reversible and controllable switching of a single-molecule junction. *Small*, 2(8-9), 973-977.
- [11] Song, H., Kim, Y., Jang, Y. H., Jeong, H., Reed, M. A., & Lee, T. (2009). Observation of molecular orbital gating. *Nature*, 462(7276), 1039-1043.
- [12] Kay, N. J., Higgins, S. J., Jeppesen, J. O., Leary, E., Lycoops, J., Ulstrup, J., & Nichols, R. J. (2012). Single-molecule electrochemical gating in ionic liquids. *Journal of the American Chemical Society*, 134(40), 16817-16826.
- [13] Haiss, W., van Zalinge, H., Higgins, S. J., Bethell, D., Höbenreich, H., Schiffrin, D. J., & Nichols, R. J. (2003). Redox state dependence of single molecule conductivity. *Journal of the American Chemical Society*, 125(50), 15294-15295.
- [14] Chen, F., He, J., Nuckolls, C., Roberts, T., Klare, J. E., & Lindsay, S. (2005). A molecular switch based on potential-induced changes of oxidation state. *Nano Letters*, 5(3), 503-506.
- [15] Xiao, X., Brune, D., He, J., Lindsay, S., Gorman, C. B., & Tao, N. (2006). Redox-gated electron transport in electrically wired ferrocene molecules. *Chemical physics*, 326(1), 138-143.
- [16] Albrecht, T., Guckian, A., Kuznetsov, A. M., Vos, J. G., & Ulstrup, J. (2006). Mechanism of electrochemical charge transport in individual transition metal

Chapter 5 ***Quantum Transport Across Graphene Nanogaps Bridged By***

- complexes. *Journal of the American Chemical Society*, 128(51), 17132-17138.
- [17] Li, C., Mishchenko, A., & Wandlowski, T. (2011). Charge transport in single molecular junctions at the solid/liquid interface. In *Unimolecular and Supramolecular Electronics II* (pp. 121-188). Springer, Berlin, Heidelberg.
- [18] Pia, E. A. D., Chi, Q., Jones, D. D., Macdonald, J. E., Ulstrup, J., & Elliott, M. (2011). Single-molecule mapping of long-range electron transport for a cytochrome b 562 variant. *Nano letters*, 11(1), 176-182.
- [19] Tsoi, S., Griva, I., Trammell, S. A., Blum, A. S., Schnur, J. M., & Lebedev, N. (2008). Electrochemically controlled conductance switching in a single molecule: Quinone-modified oligo (phenylene vinylene). *Acs Nano*, 2(6), 1289-1295.
- [20] Leary, E., Higgins, S. J., van Zalinge, H., Haiss, W., Nichols, R. J., Nygaard, S., ... & Ulstrup, J. (2008). Structure– Property Relationships in Redox-Gated Single Molecule Junctions– A Comparison of Pyrrolo-Tetrathiafulvalene and Viologen Redox Groups. *Journal of the American Chemical Society*, 130(37), 12204-12205.
- [21] Capozzi, B., Chen, Q., Darancet, P., Kotiuga, M., Buzzeo, M., Neaton, J. B., ... & Venkataraman, L. (2014). Tunable charge transport in single-molecule junctions via electrolytic gating. *Nano letters*, 14(3), 1400-1404.
- [22] Kroto H W, Heath J R, O'Brien S C, Curl R F and Smalley R E 1985 C60: buckminsterfullerene *Nature* 318 162
- [23] Iijima, S. (1991). Helical microtubules of graphitic carbon. *nature*, 354(6348), 56-58.

Chapter 5 **Quantum Transport Across Graphene Nanogaps Bridged By**

- [24] Saito R, Dresselhaus G and Dresselhaus M S 1998 Physical Properties of Carbon Nanotubes (London: Imperial College Press)
- [25] Novoselov K S, Geim A K, Morozov S V, Jiang D, Zhang Y, Dubonos S V, Grigorieva I V and Firsov A A 2004 Electric field effect in atomically thin carbon films Science 306 666
- [26] Geim A K and Novoselov K S 2007 The rise of graphene Nat. Mater. 6 183
- A. I. Yanson, I. K. Yanson, J. M. v. Ruitenbeek, Nature 400, 144 (1999) .
- [27] Roth, G., & Fischer, H. (1996). On the Way to Heptaheptaenylidene Complexes: Trapping of an Intermediate with the Novel MCCCCC CR2 Moiety. Organometallics, 15(26), 5766-5768.
- [28] CJ Lambert, H Sadeghi, S Sangtarash, Oligoyne molecular junctions for efficient room temperature thermoelectric power generation, Nano Letters 15, 7467-7472 (2015)
- [29] P. Moreno-Garcia, M. Gulcur, D. Manrique, T. Pope, W. Hong, V. Kaliginedi, C.C. Huang, A.S. Batsanov, M.R. Bryce, C.J. Lambert and T. Wandlowskii, J. Am. Chem. Soc., 135 12228-12240 (2013)
- [30] C-S. Wang, A S. Batsanov, M. R. Bryce, S. Martin, R. J. Nichols, S. J. Higgins, V. M. García-Suárez and C. J. Lambert, Oligoyne Single Molecule Wires, Journal of the American Chemical Society 131, 15647 (2009)
- [31] P. Cadiot, W. Chodkiewicz, J. Rauss-Godineau, J. Bull. Soc. Chim. Fr. 1961, 2176–2193; b) R. Hoffmann, Tetrahedron 1966, 22, 521–538.
- [32] Wendinger, D., & Tykwinski, R. R. (2017). Odd [n] cumulenes (n= 3, 5, 7, 9): synthesis, characterization, and reactivity. Accounts of chemical research, 50(6), 1468-1479.

Chapter 5 **Quantum Transport Across Graphene Nanogaps Bridged By**

- [33] Januszewski, J. A., & Tykwinski, R. R. (2014). Synthesis and properties of long [n] cumulenes ($n \geq 5$). *Chemical Society Reviews*, 43(9), 3184-3203.
- [34] Tykwinski, R. R. (2015). Carbyne: the molecular approach. *The Chemical Record*, 15(6), 1060-1074.
- [35] Kroto H W, Heath J R, O'Brien S C, Curl R F and Smalley R E 1985 C60: buckminsterfullerene *Nature* 318 162
- [36] Iijima, S. (1991). Helical microtubules of graphitic carbon. *nature*, 354(6348), 56-58.
- [37] Dresselhaus, G., & Riichiro, S. (1998). *Physical properties of carbon nanotubes*. World scientific.
- [38] Novoselov K S, Geim A K, Morozov S V, Jiang D, Zhang Y, Dubonos S V, Grigorieva I V and Firsov A A 2004 Electric field effect in atomically thin carbon films *Science* 306 666
- [39] Geim A K and Novoselov K S 2007 The rise of graphene *Nat. Mater.* 6 183
- A. I. Yanson, I. K. Yanson, J. M. v. Ruitenbeek, *Nature* 400, 144 (1999) .
- [40] G. Roth and H. Fischer, *Organometallics* 15, 5766 (1996).
- [41] CJ Lambert, H Sadeghi, S Sangtarash, Oligoyne molecular junctions for efficient room temperature thermoelectric power generation, *Nano Letters* 15, 7467-7472 (2015)
- [42] P. Moreno-Garcia, M. Gulcur, D. Manrique, T. Pope, W. Hong, V. Kaliginedi, C.C. Huang, A.S. Batsanov, M.R. Bryce, C.J. Lambert and T. Wandlowskii, *J. Am. Chem. Soc.*, 135 12228-12240 (2013)
- [43] C-S. Wang, A S. Batsanov, M. R. Bryce, S. Martin, R. J. Nichols, S. J. Higgins, V. M. García-Suárez and C. J. Lambert, *Oligoyne Single Molecule Wires*, *Journal of the American Chemical Society* 131, 15647 (2009)

Chapter 5 **Quantum Transport Across Graphene Nanogaps Bridged By**

- [44] P. Cadiot, W. Chodkiewicz, J. Rauss-Godineau, J. Bull. Soc. Chim. Fr. 1961, 2176–2193; b) R. Hoffmann, Tetrahedron 1966, 22, 521–538.
- [45] Wendinger, D., & Tykwinski, R. R. (2017). Odd [n] cumulenes (n= 3, 5, 7, 9): synthesis, characterization, and reactivity. Accounts of chemical research, 50(6), 1468-1479.
- [46] Januszewski, J. A., & Tykwinski, R. R. (2014). Synthesis and properties of long [n] cumulenes (n \geq 5). Chemical Society Reviews, 43(9), 3184-3203.
- [47] Tykwinski, R. R. (2015). Carbyne: the molecular approach. The Chemical Record, 15(6), 1060-1074.
- [48] J. A. Januszewski, D. Wendinger, C. D. Methfessel, F. Hampel, R. R. Tykwinski, Angew. Chem. Int. Ed. 2013, 52, 1817–1821
- [49] S. Gunasekaran, D. Hernangómez-Pérez, I. Davydenko, S. Marder, F. Evers, L. Venkataraman, Nano. Lett. 2018, 18, 6387–6391.
- [50] J. Prasongkit, A. Grigoriev, G. Wendin, R. Ahuja, Phys. Rev. B 2010, 81, 15404.
- [51] M. Weimer, W. Hieringer, F. D. Sala, A. Görling, Chem. Phys. 2005, 309, 77–87.
- [52] M. Tommasini, A. Milani, D. Fazzi, A. Lucotti, C. Castiglioni, J. A. Januszewski, D. Wendinger, R. R. Tykwinski, J. Phys. Chem. C 2014, 118, 26415–26425.
- [53] Wenjun Xu, Edmund Leary, Songjun Hou, Sara Sangtarash, M. Teresa González, Qingqing Wu, Hatef Sadeghi, Lara Tejerina, Nicolás Agraït, Simon J. Higgins, Colin J. Lambert, Richard J. Nichols, and Harry L. Anderson, Angewandte Chemie May (2019)

- [54] V. Mujica, M. Kemp, A. Roitberg, and M. Ratner, *J. Chem. Phys.* 104, 7296 (1996).
- [55] W. Tian, S. Datta, S. Hong, R. Riefenberger, J. I. Henderson, and C. P. Kubiak, *J. Chem. Phys.* 109, 2874 (1998).
- [56] Lang, N. D., & Avouris, P. (1998). Oscillatory conductance of carbon-atom wires. *Physical review letters*, 81(16), 3515.
- [57] Mehrez, H., Wlasenko, A., Larade, B., Taylor, J., Grütter, P., & Guo, H. (2002). I– V characteristics and differential conductance fluctuations of Au nanowires. *Physical Review B*, 65(19), 195419.
- [58] Di Ventra, M., Pantelides, S. T., & Lang, N. D. (2000). First-principles calculation of transport properties of a molecular device. *Physical review letters*, 84(5), 979.
- [59] Reed, M. A., Zhou, C., Muller, C. J., Burgin, T. P., & Tour, J. M. (1997). Conductance of a molecular junction. *Science*, 278(5336), 252-254.
- [60] G.J. Ashwell, B. Urasinska, C. Wang, M.R. Bryce, I. Grace, C.J. Lambert, Single-molecule electrical studies on a 7 nm long molecular wire, *Chem. Comm.*, 45 4706-4708 (2006)
- [61] V.M. García-Suárez, A.R. Rocha, S.W. Bailey, C.J. Lambert, S. Sanvito, J. Ferrer, Single-channel conductance of H₂ molecules attached to platinum or palladium electrodes, *Phys. Rev. B* 72 (4), 045437 (2005)
- [62] Emberly, E. G., & Kirczenow, G. (2002). Molecular spintronics: spin-dependent electron transport in molecular wires. *Chemical Physics*, 281(2-3), 311-324.
- [63] Zwolak, M., & Di Ventra, M. (2002). DNA spintronics. *Applied physics letters*, 81(5), 925-927.

Chapter 5 Quantum Transport Across Graphene Nanogaps Bridged By

- [64] Ouyang, M., & Awschalom, D. D. (2003). Coherent spin transfer between molecularly bridged quantum dots. *Science*, 301(5636), 1074-1078.
- [65] Chakraborty, S., Walsh, K. M., Alphenaar, B. W., Liu, L., & Tsukagoshi, K. (2003). Temperature-mediated switching of magnetoresistance in Co-contacted multiwall carbon nanotubes. *Applied physics letters*, 83(5), 1008-1010.
- [66] Pati, R., Senapati, L., Ajayan, P. M., & Nayak, S. K. (2003). First-principles calculations of spin-polarized electron transport in a molecular wire: Molecular spin valve. *Physical Review B*, 68(10), 100407.
- [67] AR Rocha, VM Garcia-Suarez, SW Bailey, CJ Lambert, J Ferrer, S Sanvito, Towards molecular spintronics, *Nature materials* 4 (4), 335 (2005)
- [68] Burzurí E, Prins F, van der Zant H Characterization of nanometer-spaced few layer graphene electrodes. *Graphene* 1(2):26–29 (2012).
- [69] Deng X, Zhang Z, Tang G, Fan Z, Yang C Spin filtering and large magnetoresistance behaviors in carbon chain-zigzag graphene nanoribbon nanojunctions. *Phys Lett A* 378(21):1540–1547 (2014).
- [70] Zanolli Z, Onida G, Charlier J-C, Quantum spin transport in carbon chains. *ACS Nano* 4(9):5174–5180 (2010).
- [71] Akdim B, Pachter R Switching behavior of carbon chains bridging graphene nanoribbons: Effects of uniaxial strain. *ACS Nano* 5(3):1769–1774 (2011).
- [72] Shen L, et al. Electron transport properties of atomic carbon nanowires between graphene electrodes. *J Am Chem Soc* 132(33):11481–11486 (2010).
- [73] Sadeghi, H.; Mol, J.; Lau, C.; Briggs, G. A. D.; Warner, J.; Lambert, C. J., Conductance Enlargement in Pico-scale Electro-burnt Graphene

Chapter 5 ***Quantum Transport Across Graphene Nanogaps Bridged By***

- Nanojunctions, Proceedings of the National Academy of Sciences 9, 2658-2663 (2015)
- [74] Bart Limburg, James O. Thomas, Gregory Holloway, Hatef Sadeghi, Sara Sangtarash, Jonathan Cremers, Akimitsu Narita, Klaus Müllen, Colin J. Lambert, G. Andrew D. Briggs, Jan Mol, and Harry L. Anderson, Anchor Groups for Graphene-Porphyrin Single-Molecule Transistors. *Adv. Func. Mat.* 28 1803629 (2018)
- [75] Pascal Gehring, Jakub K Sowa, Jonathan Cremers, Qingqing Wu, Hatef Sadeghi, Yuewen Sheng, Jamie H Warner, Colin J Lambert, G Andrew D Briggs, Jan A Mol, Distinguishing lead and molecule states in graphene-based single-electron transistors, *ACS Nano* 11 (3) 3404 -3412 (2017)
- [76] JA Mol, CS Lau, WJM Lewis, H Sadeghi, C Roche, A Cnossen, JH Warner, C.J. Lambert, H.L. Anderson and G.A.D. Briggs, Graphene-porphyrin single-molecule transistors, *Nanoscale* 7 (31), 13181-13185 (2015)
- [77] Rong, Y., & Warner, J. H. (2014). Wired up: interconnecting two-dimensional materials with one-dimensional atomic chains. *ACS nano*, 8(12), 11907-11912..
- [78] Lin, Y. C., Morishita, S., Koshino, M., Yeh, C. H., Teng, P. Y., Chiu, P. W., ... & Suenaga, K. (2016). Unexpected huge dimerization ratio in one-dimensional carbon atomic chains. *Nano letters*, 17(1), 494-500.
- [79] Botello-Méndez, A. R., Lopez-Urias, F., Terrones, M., & Terrones, H. (2009). Metallic and ferromagnetic edges in molybdenum disulfide nanoribbons. *Nanotechnology*, 20(32), 325703.

Chapter 5 ***Quantum Transport Across Graphene Nanogaps Bridged By***

- [80] Lee, H., Son, Y. W., Park, N., Han, S., & Yu, J. (2005). Magnetic ordering at the edges of graphitic fragments: Magnetic tail interactions between the edge-localized states. *Physical Review B*, 72(17), 174431.
- [81] Soler, J. M.; Artacho, E.; Gale, J. D.; Garcia, A.; Junquera, J.; Ordejon, P.; Sanchez-Portal, D. *J. Phys.: Condens. Matter* 2002, 14 (11), 2745.
- [82] Perdew, J. P. J.; Burke, K.; Ernzerhof, M. *Phys. Rev. Lett.* 1996, 77 (18), 3865–3868.
- [83] Frisch, M. J. *Gaussian g09; Revision E.01*, Gaussian, Inc.: Wallingford, CT, 2016.
- [84] Ferrer, J.; Lambert, C. J.; García-Suárez, V. M.; Manrique, D. Z.; Visontai, D.; Oroszlany, L.; Rodríguez-Ferradás, R.; Grace, I.; Bailey, S. W. D.; Gillemot, K.; Sadeghi, H.; Algharagholi, L. A. *New J. Phys.* 2014, 16, 093029.

Chapter 6

6.1 Conclusion

The electric properties of different molecular devices have been studied in this thesis using density functional theory and the Green's function scattering formalism which are described in chapter 2 and 3 respectively.

In the chapter 4, I investigated the charge transport through thiophene core molecules; I explained the gating of destructive quantum interference in molecular junctions observed using the applied electrode potential without electrochemical reaction. The molecular conductance was increased by reducing the distance between the negative side of an ionic liquid and the molecular backbone, On the other hand the molecular conductance was decreased by reducing the distance between the thiophene molecule and the positive side of the ionic liquid. This work provides evidence of the tuning of charge transport at an anti-resonance state arising from DQI at room temperature.

In the chapter 5, I studied quantum transport across graphene nanogaps bridged by carbon atomic chains. As a step towards realising the technological potential of electroburnt graphene junctions, I investigated how their electronic and spintronic properties are controlled by edge terminations and by the carbon chains bridging their gaps. Such junctions are of particular interest, because of the stable covalent bonding of atomic carbon bridges to the electrodes. One can conceive of an infinite number of combinations of edges and chains in such graphene-based junctions and in the present study, I have presented results for a selection of these. Although a wide range of transport properties are possible, I find that junctions can be divided into a small

number of categories, according to their qualitative transport properties. For example, junctions can be spin active or spin quiescent, depending on the saturated or unsaturated nature of the graphene edges, on the odd or even length of the carbon bridge and on the odd or even nature of the terminal electrode ring attached to the graphene chain. Furthermore, such features can change the electrical conductance of the junction by orders of magnitude. These results demonstrate that if junction geometries and edge terminations can be controlled, then graphene electroburnt junctions offer the possibility of exploiting a wide range of functionalities in stable, all-carbon nanostructures.

6.2 Future Work

In this thesis, I have concentrated on electron and transport through single molecules attached to either gold or graphene leads. For the last study, I calculated transport across graphene nanogaps bridged by carbon atomic chains, and used hydrogen to saturate the edges. For the future it would of interest to include oxygen, nitrogen and bromine elements for edge saturation. It would also be of interest to study asymmetric junctions and see the effect on electron transmission [1-4]. In practice, for such complex structures, it may not be possible to obtain simple analytic results. Nevertheless such problems could be investigated numerically, using quantum transport codes such as the multiple-scattering code Gollum [5].

References

- [1] Sahu, B., Min, H., & Banerjee, S. K. (2011). Edge saturation effects on the magnetism and band gaps in multilayer graphene ribbons and flakes. *Physical Review B*, 84(7), 075481.
- [2] Lu, Y. H., Wu, R. Q., Shen, L., Yang, M., Sha, Z. D., Cai, Y. Q., ... & Feng, Y. P. (2009). Effects of edge passivation by hydrogen on electronic structure of armchair graphene nanoribbon and band gap engineering. *Applied Physics Letters*, 94(12), 122111.
- [3] Cui, L. L., Long, M. Q., Zhang, X. J., Li, X. M., Zhang, D., & Yang, B. C. (2016). Spin-dependent transport properties of hetero-junction based on zigzag graphene nanoribbons with edge hydrogenation and oxidation. *Physics Letters A*, 380(5-6), 730-738.
- [4] Liu, J., Zhang, Z. H., Deng, X. Q., Fan, Z. Q., & Tang, G. P. (2015). Electronic structures and transport properties of armchair graphene nanoribbons by ordered doping. *Organic Electronics*, 18, 135-142.
- [5] Ferrer, J., Lambert, C. J., García-Suárez, V. M., Manrique, D. Z., Visontai, D., Oroszlany, L., ... & Sadeghi, H. (2014). GOLLUM: a next-generation simulation tool for electron, thermal and spin transport. *New Journal of Physics*, 16(9), 093029.